Chapter 1
Dynamics in Mechatronic Systems

Section 1.1 is devoted to the study of dynamical processes in electric circuits. It includes derivations of the constitutive relations of elements of electric circuits (capacitors, inductors) and describes current and voltage sources and Kirchhoff's law. Section 1.2 deals with dynamical processes in mechatronic systems (transducers) and the electromagnetomechanical circuit. In Sect. 1.3, the dynamics and control of a mass levitating in magnetic and gravitational fields is discussed. Two cases of numerical control are considered and verified experimentally. In Sect. 1.4, combined analytical and numerical analyses of vibrations in string-type generators is carried out. The vibrations of a string are governed by a PDE, whereas the dynamics of an amplifier is governed by an ODE with a time delay. The voltage generated on the string ends depends on both electromagnetic induction and string vibration speed. An averaged set of equations is derived and numerically studied. Finally, in Sect. 1.5, a 2-DOF nonlinear dynamics of a rotor supported by a magnetohydrodynamic bearing is investigated using perturbation analysis. Two modes corresponding to the vertical and horizontal vibrations of the rotor are coupled. The non-resonant case and the various resonant cases (with and without an internal resonance) are considered. Frequency-response curves are obtained. When the amplitude of the external harmonic excitation is near one of the natural frequencies of the vibrations and the system experiencing internal resonance, a saturation phenomenon occurs. When the amplitude of the external excitation increases, after some critical value the energy pumping between various submotions of the rotor occurs for each mode. Further, it is shown that in the case of rigid magnetic materials, hysteresis may be a cause of chaotic vibrations of the rotor. Chaotic regions and the amplitude level contours of the rotor vibrations are obtained in various control parameter planes.

J. Awrejcewicz and Z. Koruba, *Classical Mechanics*, Advances in Mechanics and Mathematics 30, DOI 10.1007/978-1-4614-3978-3_1,

1.1 Dynamical Processes in Electric Circuits

In Sect. 1.1, to write equations of dynamics in mechatronic systems, we will make use of the unified approach developed from mechanics and based on variational calculus [1, 2]. It should be emphasized that such an approach is based on the theory of the quasistatic electromagnetic field whose changes are slow enough to neglect the interactions occurring between magnetic and electric fields. Electric circuits consist of *passive elements* such as resistors, coils, and capacitors and *active elements* such as voltage and current sources.

1.1.1 Constitutive Relations of Elements of Electric Circuits

1.1.1.1 The Capacitor

Figure 1.1a shows a schematic of a capacitor to whose plates the voltage U was applied and an example of a constitutive function $U(Q)$ (Fig. 1.1b).

As the capacitor is charged, the charge Q is supplied to one of its plates and removed from another. The change in the charge on the plates separated by a dielectric produces the current flow

$$I = \frac{\mathrm{d}Q}{\mathrm{d}t} \equiv \dot{Q}. \tag{1.1}$$

During charging, a potential difference appears between the plates of the capacitor (voltage U). An example of measurements of the voltage U and the corresponding charge Q in static conditions leads to the construction of graph $U(Q)$ (Fig. 1.1b).

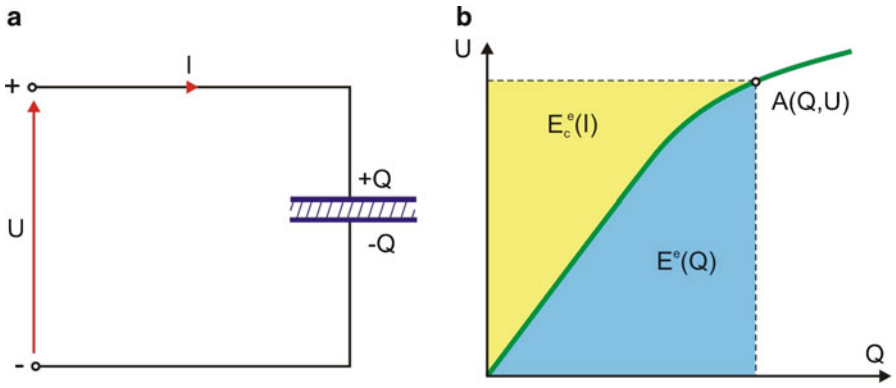

Fig. 1.1 Schematic diagram of a capacitor (**a**) and a constitutive function $U(Q)$ (**b**)

The electric energy gathered in the capacitor $E^{\mathrm{e}}(Q)$ is equivalent to the work done while charging it from value 0 to Q and is equal to

$$E^{\mathrm{e}}(Q) \equiv W^{\mathrm{e}}(Q) = \int_0^t N^{\mathrm{e}} \mathrm{d}t = \int_0^t UI \mathrm{d}t = \int_0^Q U \mathrm{d}Q, \tag{1.2}$$

where $N^{\mathrm{e}} = \dot{W}^{\mathrm{e}}$ is the power supplied to the system, and during transformations (1.1) was used. The value of integral (1.2) corresponds to the area under the curve $U(Q)$ in Fig. 1.1b. If in the neighborhood of the operating point A of the capacitor we conduct the linearization, we obtain

$$Q = CU = C \frac{\mathrm{d}E^{\mathrm{e}}}{\mathrm{d}Q}, \tag{1.3}$$

and integrating we have

$$E^{\mathrm{e}}(Q) = \frac{Q^2}{2C}. \tag{1.4}$$

A complementary state function may be easily determined on the basis of Fig. 1.1b, and it is equal to

$$E^{\mathrm{e}}(Q) + E_{\mathrm{c}}^{\mathrm{e}}(I) = UQ, \tag{1.5}$$

where $E_{\mathrm{c}}^{\mathrm{e}}(I)$ is the so-called *complementary energy*.

Making use of the method described earlier it is easy to notice that

$$E_{\mathrm{c}}^{\mathrm{e}}(U) = \frac{CU^2}{2}. \tag{1.6}$$

1.1.1.2 The Inductor

It is widely known that if the current of intensity I flows through a conductor, then around the conductor there is generated a magnetic field proportional to the intensity of the flowing current. In turn, if the conductor is situated in the changing magnetic field, then the voltage will be generated at its ends.

If the conductor is wound in turns so as to form a coil, then the generated magnetic flux Φ is proportional to the intensity of the current I flowing through the coil. If we now put a ferromagnetic core inside the coil, then the density of the magnetic flux is substantially increased.

According to Faraday's law of induction, the voltage induced in a conductor is equal to

$$U = \frac{\mathrm{d}\Phi}{\mathrm{d}t} \equiv \dot{\Phi}. \tag{1.7}$$

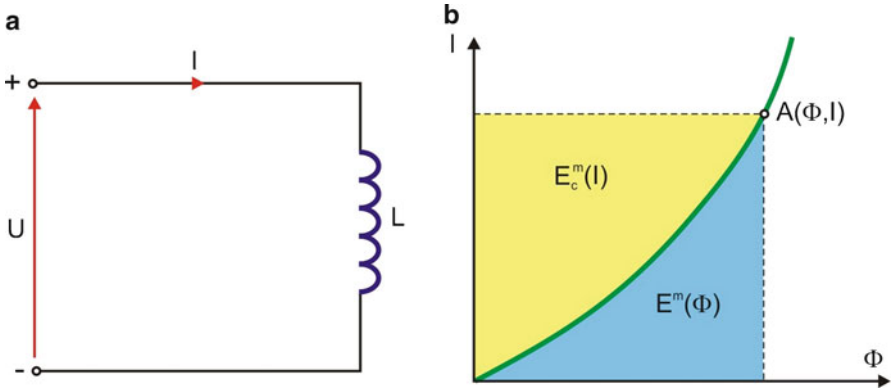

Fig. 1.2 Schematic diagram of an inductor (**a**) and the graph of the constitutive function (**b**)

If we have an ideal conductor, then $I = \text{const}$ (intensity of the current does not change in time) and a magnetic flux $\Phi = \text{const}$. In this case, from (1.7) it follows that $U = 0$ (the voltage in the conductor is not induced). If we perform the linearization of the function $I(\Phi)$ (Fig. 1.2b) in the neighborhood of operating point A, then

$$\Phi = LI, \tag{1.8}$$

where L is called the *inductance*.

As in the case of the capacitor, the magnetic energy stored in an ideal conductor is calculated based on the knowledge of the power supplied to the conductor (to the electric circuit) $N^{\mathrm{e}} = UI$, and it is equal to

$$E^{\mathrm{m}}(\Phi) = \int_0^t UI\,\mathrm{d}t = \int_0^{\Phi} I\,\mathrm{d}\Phi. \tag{1.9}$$

On the basis of the method described earlier we calculate the magnetic energy $E^{\mathrm{m}}(\Phi)$ and complementary magnetic energy $E_c^{\mathrm{m}}(I)$ of the forms

$$E^{\mathrm{m}}(\Phi) = \frac{\Phi^2}{2L}, \qquad E_c^m(I) = \frac{LI^2}{2}, \tag{1.10}$$

where

$$I = \frac{\mathrm{d}E^{\mathrm{m}}}{\mathrm{d}\Phi}. \tag{1.11}$$

It is easy to notice that

$$E^{\mathrm{m}}(\Phi) + E_c^m(I) = \Phi\mathrm{I}. \tag{1.12}$$

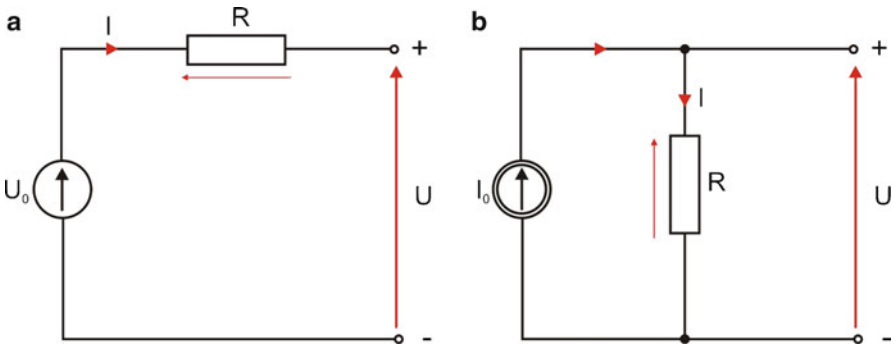

Fig. 1.3 Ideal voltage source (**a**) and ideal current source (**b**)

1.1.1.3 Current and Voltage Sources and Kirchhoff's Laws

An *ideal voltage source* is a source that produces the voltage $U = U(t)$ in a conductor (an electric circuit) and is not affected by the current flowing in the conductor (the circuit). During the composition of Lagrange's equations voltages will be treated as generalized forces.

In turn, a source that in a conductor produces the current intensity $I = I(t)$ and is not affected by the voltage in the conductor (the electric circuit) is called an *ideal current source*.

During composition of Lagrange's equations the current intensity $I(t) = \dot{Q}(t)$ in a dissipation function D is taken with a negative sign because it is the active element supplying the energy.

Figure 1.3a, b shows a schematic of the ideal voltage (current) source.

Voltage-current characteristics corresponding to Fig. 1.3a, b are respectively described by the equations

$$U_0 = U + RI, \tag{1.13}$$

$$RI_0 = U = RI. \tag{1.14}$$

It turns out that the development of contemporary electronics allows for the construction of almost ideal voltage and current sources.

If we now connect together the active elements (sources) and the passive ones (resistors, coils, and capacitors), then we will impose certain constraints on the variables describing the processes in the isolated, i.e., considered individually, elements (conductors or circuits). Such constraints imposed on electric systems are known as *Kirchhoff's laws*.

Theorem 1.1 (Kirchhoff's current law). *The sum of currents entering and leaving an arbitrary node of an electric circuit must be equal to zero (the conservation of electric charge).*

Theorem 1.2 (The Kirchhoff's voltage law). *The sum of voltage drops on each element along a closed subcircuit (loop) must be equal to zero (meaning that the electric potential at any point in the circuit is independent of the choice of the path leading to that point).*

There are many books (and other publications) devoted to the methods of composition of equations describing current processes in electric circuits based on Kirchhoff's law (the so-called *direct methods*), and they will not be described in this textbook. Mainly, the *indirect (variational) methods* originating in classical mechanics will be used here.

1.1.2 Application of Hamilton's Principle and Lagrange's Equations to Electrical Systems

There exist two possibilities for formulating Hamilton's principle for electromagnetic systems by different choices of generalized coordinates.

In the first case as generalized coordinates we will choose the charge Q_n and the current intensity I_n. The general equation of mechanics allows, by analogy, for a direct formulation of the general equation of electromagnetic systems of the form

$$\sum_{n=1}^{N}\left(U_n - \frac{\mathrm{d}\Phi_n}{\mathrm{d}t}\right)\delta Q_n = 0, \tag{1.15}$$

where now N denotes the number of elements of an electric circuit. In turn, the first component of (1.15) will be represented in the form

$$\sum_{n=1}^{N} U_n \delta Q_n = -\delta E^{\mathrm{e}} + \sum_{n*=1}^{N*} U_{n*}\delta Q_{n*}, \tag{1.16}$$

where U_{n^*} denotes generalized voltages associated with the n^*th non-conservative element.

In the preceding equation there is a distinction made between the fraction of the work (the energy) done by an element of conservative electrical circuit E^{e} and that done by N^* non-conservative elements associated with the generalized coordinates Q_{n^*}.

The minus sign in front of δE^{e} means that the application of voltage to a conservative element results in a decrease of electrical energy inside this element. In turn, the second component of (1.15) will be transformed in the following way:

$$-\sum_{n=1}^{N}\frac{\mathrm{d}\Phi_n}{\mathrm{d}t}\delta Q_n = -\sum_{n=1}^{N}\frac{\mathrm{d}}{\mathrm{d}t}\left(\Phi_n \delta Q_n\right) + \sum_{n=1}^{N}\Phi_n\frac{\mathrm{d}\left(\delta Q_n\right)}{\mathrm{d}t}. \tag{1.17}$$

Since according to (1.1) and (1.11) we have

$$\sum_{n=1}^{N} \Phi_n \frac{\mathrm{d}}{\mathrm{d}t} \delta Q_n = \sum_{n=1}^{N} \Phi_n \delta I_n = \delta E^{\mathrm{m}}, \tag{1.18}$$

taking into account the obtained result in the integrated (1.15) we have

$$\begin{aligned} S &= \int_{t_1}^{t_2} \left[-\delta E^{\mathrm{m}} - \delta E^{\mathrm{e}} + \sum_{n^*=1}^{N^*} U_{n^*} \delta Q_{n^*} - \sum_{n=1}^{N} \frac{\mathrm{d}}{\mathrm{d}t} \left(\Phi_n \delta Q_n \right) \right] \mathrm{d}t \\ &= \int_{t_1}^{t_2} \left[-\delta \left(E^{\mathrm{m}} + E^{\mathrm{e}} \right) + \sum_{n^*=1}^{N^*} U_{n^*} \delta Q_{n^*} \right] \mathrm{d}t - \underline{\sum_{n=1}^{N} \left[\Phi_n \delta Q_n \right]_{t_1}^{t_2}} \\ &= \int_{t_1}^{t_2} \left[-\delta \left(E^{\mathrm{m}} + E^{\mathrm{e}} \right) + \sum_{n^*=1}^{N^*} U_{n^*} \delta Q_{n^*} \right] \mathrm{d}t \\ &= \int_{t_1}^{t_2} \left[-\delta L + \sum_{n^*=1}^{N^*} U_{n^*} \delta Q_{n^*} \right] \mathrm{d}t = 0, \end{aligned} \tag{1.19}$$

because, according to Hamilton's principle, the underlined term is equal to zero, since $\delta Q_n(t_1) = \delta Q_n(t_2) = 0$. In (1.19), $L = E^{\mathrm{m}} + E^{\mathrm{e}}$, and it denotes the Lagrangian function.

In other words, according to Hamilton's principle, the dynamic equilibrium of a physical system is realized by the system by means of the choice of the *extremal value of the action* between the states of the system at time instants t_1 and t_2. The extremal value of the action in an electric circuit according to Hamilton leads to (1.19) for all possible and permitted changes of the charge δQ_n during the transition between the states of the system determined at time instants t_1 and t_2 and such that $\delta Q_n(t_1) = \delta Q_n(t_2) = 0$.

According to the notation introduced earlier, E^{m} in the equation denotes the magnetic energy in the circuit, that is, it is the sum of all energies of the individual conductors in the circuit expressed in terms of the current intensity I. In turn, E^{e} denotes the electric energy of the circuit, which is the sum of electric energies of all individual conductors in the circuit related to the charge Q_n. The possible current and charge intensities are allowed if they satisfy Kirchhoff's law and additionally $I_n = \frac{\mathrm{d}Q_n}{\mathrm{d}t}$. The expression $\sum_{n^*=1}^{N^*} U_{n^*} \delta Q_{n^*}$ represents the virtual work of non-conservative elements of the circuit. Let us now proceed to the second way to formulate Hamilton's principle for electromagnetic systems, that is, now we will choose as generalized coordinates the magnetic flux Φ_n and the voltage U_n.

Similarly to the previous case, the general equation of mechanics allows for the formulation of equation dual to (1.15) of the form

$$\sum_{n=1}^{N}\left(I_n - \frac{\mathrm{d}Q_n}{\mathrm{d}t}\right)\delta\Phi_n = 0, \tag{1.20}$$

where N denotes the number of circuit elements.

The first component of (1.20) will be represented as

$$\sum_{n=1}^{N} I_n\delta\Phi_n = -\delta E^{\mathrm{m}} + \sum_{n^*=1}^{N^*} I_{n^*}\delta\Phi_{n^*}, \tag{1.21}$$

where E^{m} denotes the magnetic energy of all elements in the circuit, whereas the second term on the right-hand side of (1.21) denotes the work associated with non-conservative elements of the circuit related to the generalized current intensities I_{n^*} and magnetic fluxes Φ_{n^*}, and N^* denotes the number of independent coordinates of magnetic fluxes.

The second component of (1.20) has the form

$$-\sum_{n=1}^{N}\frac{\mathrm{d}Q_n}{\mathrm{d}t}\delta\Phi_n = -\sum_{n=1}^{N}\frac{\mathrm{d}}{\mathrm{d}t}\left(Q_n\delta\Phi_n\right) + \sum_{n=1}^{N} Q_n\frac{\mathrm{d}}{\mathrm{d}t}\left(\delta\Phi_n\right). \tag{1.22}$$

Because according to (1.7) and (1.2) we have

$$\sum_{n=1}^{N} Q_n\frac{\mathrm{d}}{\mathrm{d}t}\delta\Phi_n = \sum_{n=1}^{N} Q_n\delta\left(\frac{\mathrm{d}\Phi_n}{\mathrm{d}t}\right) = \sum_{n=1}^{N} Q_n\delta U_n = \delta E^{\mathrm{e}}, \tag{1.23}$$

taking into account (1.23) in integrated (1.20) and taking into account (1.21) and (1.22) we obtain

$$\begin{aligned} S &= \int_{t_1}^{t_2}\left[-\delta L + \sum_{n^*=1}^{N^*} I_{n^*}\delta Q_{n^*} - \underline{\sum_{n=1}^{N}\frac{\mathrm{d}}{\mathrm{d}t}\left(Q_n\delta\Phi_n\right)}\right]\mathrm{d}t \\ &= \int_{t_1}^{t_2}\left[-\delta L + \sum_{n^*=1}^{N^*} I_{n*}\delta Q_{n^*}\right]\mathrm{d}t = 0, \end{aligned} \tag{1.24}$$

because, according to Hamilton's principle, the underlined term becomes zero (since we have $\delta\Phi_{n^*}(t_1) = \delta\Phi_{n^*}(t_2) = 0$).

In (1.24), E^{e} is the electric energy of the circuit that is the sum of all energies of the individual elements (the conductors) and expressed in terms of the voltage U_n. In turn, E^{m} is the function of magnetic energy of the circuit that is the sum of the

magnetic energies of all its conductors. The Lagrangian function $L = E^{\mathrm{m}} - E^{\mathrm{e}}$ and the adopted generalized coordinates, that is, the voltage U_n and the magnetic flux Φ_n, will be allowed if they satisfy Kirchhoff's law $U_n = \frac{\mathrm{d}\Phi_n}{\mathrm{d}t}$.

From Hamilton's principle follow directly Lagrange's equations (see Chap. 3 of [3]). We will derive two elementary forms of Lagrange's equations of the second kind in relation to generalized coordinates Q_n (the charge) and Φ_n (the magnetic flux).

In the first case, according to (1.19), the Lagrangian of the electrical system is equal to

$$L = E^{\mathrm{m}}(\dot{Q}_n) + E^{\mathrm{e}}(Q_n), \qquad n = 1, \ldots, N, \tag{1.25}$$

where N denotes the number of generalized coordinates. Work done by non-conservative elements can be expressed by independent generalized coordinates Q_{n^*} in the following way:

$$\sum_{n*=1}^{N^*} U_{n^*}^* \delta Q_{n^*} = \sum_{n=1}^{N} U_n \delta Q_n, \tag{1.26}$$

and Lagrange's equations of the second kind in this case take the forms

$$\frac{\mathrm{d}}{\mathrm{d}t}\left(\frac{\partial L}{\partial \dot{Q}_n}\right) - \frac{\partial L}{\partial Q_n} = U_n, \qquad n = 1, \ldots, N, \tag{1.27}$$

where U_n is the generalized voltage corresponding to the generalized charge Q_n. Non-homogeneous Lagrange (1.27) after the introduction of a dissipation function

$$D(\dot{Q}) = \frac{R\dot{Q}^2}{2} \tag{1.28}$$

will take the form of homogeneous equations

$$\frac{\mathrm{d}}{\mathrm{d}t}\left(\frac{\partial L}{\partial \dot{Q}_n}\right) + \frac{\partial D}{\partial \dot{Q}_n} - \frac{\partial L}{\partial Q_n} = 0 \tag{1.29}$$

because

$$U_n = -\frac{\partial D}{\partial \dot{Q}_n}. \tag{1.30}$$

In the second case, according to (1.24), the Lagrangian of the electrical system is equal to

$$L = E^{\mathrm{m}}(\dot{\Phi}_n) - E^{\mathrm{e}}(\Phi_n), \qquad n = 1, \ldots, N, \tag{1.31}$$

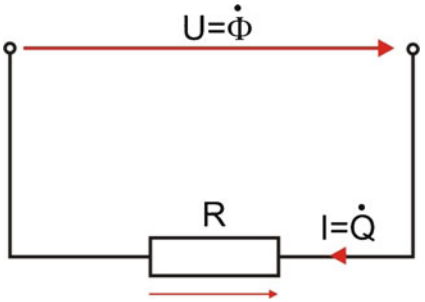

Fig. 1.4 A resistor R as an example of a non-conservative conductor

where $n = 1, \ldots, N$ denotes independent generalized coordinates of magnetic fluxes. In this case the work done by non-conservative elements is expressed by

$$\sum_{n^*=1}^{N^*} I_{n^*}^* \delta \Phi_{n^*} = \sum_{n=1}^{N} I_n \delta \Phi_n, \tag{1.32}$$

where I_n is the generalized current intensity corresponding to the generalized magnetic flux Φ_{n^*}, or by the dissipation function D, which will be shown on examples. Lagrange's equations for this case take the form

$$\frac{\mathrm{d}}{\mathrm{d}t}\left(\frac{\partial L}{\partial \dot{\Phi}_n}\right) + \frac{\partial L}{\partial \Phi_n} = I_n, \quad n = 1, \ldots, N. \tag{1.33}$$

Non-homogeneous Lagrange (1.33), following the introduction of a dissipation function

$$D(\dot{\Phi}) = \frac{\dot{\Phi}^2}{2R}, \tag{1.34}$$

will take the homogeneous form

$$\frac{\mathrm{d}}{\mathrm{d}t}\left(\frac{\partial L}{\partial \dot{\Phi}_n}\right) + \frac{\partial D}{\partial \dot{\Phi}} - \frac{\partial L}{\partial \Phi_n} = 0, \tag{1.35}$$

because

$$I_n = -\frac{\partial D}{\partial \dot{\Phi}}. \tag{1.36}$$

Finally, let us consider virtual work done on a non-conservative element (a resistor R) with the application of two different generalized coordinates, that is, the charge Q and the magnetic flux Φ (Fig. 1.4).

Work done on the non-conservative element can be positive (supplied energy) or negative (removed energy). In the case of the resistor shown in Fig. 1.4, the virtual work can be expressed in two ways:

(a) By the generalized charge

$$U\delta Q = -RI\delta Q = -R\dot{Q}\delta Q; \tag{1.37}$$

(b) By the generalized magnetic flux

$$I\delta\Phi = -\frac{U}{R}\delta\Phi = -\frac{\dot{\Phi}}{R}\delta\Phi, \tag{1.38}$$

where in both cases the minus sign denotes energy losses.

In the case of an ideal voltage generator, the voltage variation and, consequently, the variation of the flux change in time is equal to zero, and in this case virtual work can be expressed only in one way, that is, in terms of the variation of generalized charge of the form

$$U\delta Q = U_*\delta Q_*, \tag{1.39}$$

where the voltage of an ideal generator is denoted by U_*.

In turn, in the case of an ideal current intensity generator, the virtual work can be expressed only by changes in the generalized magnetic flux Φ, and it is equal to

$$I(t)\delta\Phi = I_*(t)\delta\Phi, \tag{1.40}$$

because in this case $\delta I = 0$.

Example 1.1. Derive equations of dynamics of electromagnetic processes in the circuit presented in Fig. 1.5 by means of the two methods described earlier.

(a) We choose charges Q_1 and Q_2 as generalized coordinates. The circuit is divided into two loops in which flow the currents $I_n(t) = \dot{Q}_n(t)$, $n = 1, 2$. However, these two generalized coordinates are dependent since

$$\dot{Q}_2 = \dot{Q}_1 + \dot{Q}_0,$$

where $\dot{Q}_0 = I(t)$.

Lagrange's (1.29) in this case takes the form

$$\frac{\mathrm{d}}{\mathrm{d}t}\left(\frac{\partial E^{\mathrm{m}}}{\partial\dot{Q}_1}\right) + \frac{\partial D}{\partial\dot{Q}_1} - \frac{\partial E^{\mathrm{e}}}{\partial Q_1} = 0,$$

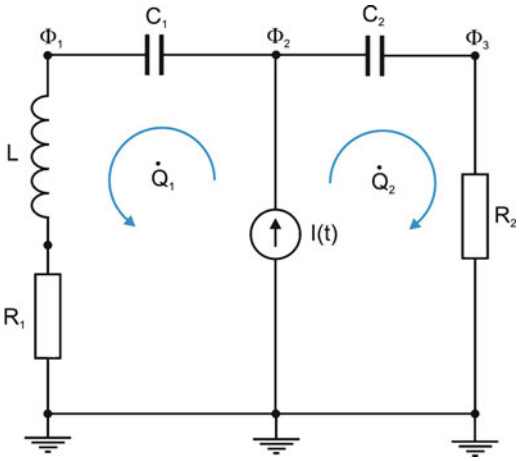

Fig. 1.5 Electric circuit constructed from two capacitors C_1 and C_2, resistors R_1 and R_2, an inductor L, and ideal current generator $I(t)$

where

$$E^{\mathrm{m}} = \frac{1}{2} L \dot{Q}_1^2, \quad E^{\mathrm{e}} = \frac{Q_1^2}{2C_1} + \frac{Q_2^2}{2C_2}, \quad D = \frac{1}{2} R_1 \dot{Q}_2^2 + \frac{1}{2} R_2 \dot{Q}_1^2.$$

We successively calculate

$$\frac{\partial E^{\mathrm{m}}}{\partial \dot{Q}_1} = L \dot{Q}_1, \qquad \frac{\mathrm{d}}{\mathrm{d}t}\left(\frac{\partial E^{\mathrm{m}}}{\partial \dot{Q}_1}\right) = L \ddot{Q}_1,$$
$$\frac{\partial E^{\mathrm{e}}}{\partial Q_1} = \frac{Q_1}{C_1} + \frac{Q_1 + Q_0}{C_2} = Q_1 \left(\frac{C_1 + C_2}{C_1 C_2}\right) + \frac{Q_0}{C_2},$$
$$\frac{\partial D}{\partial \dot{Q}_1} = (R_1 + R_2)\, \dot{Q}_1 + R_1 \dot{Q}_0,$$

and eventually obtain

$$L \ddot{Q}_1 + (R_1 + R_2)\, \dot{Q}_1 + \frac{C_1 + C_2}{C_1 C_2} Q_1 = -R I(t) - \frac{1}{C_2} \int_0^t I(t) \mathrm{d}t.$$

(b) We choose magnetic fluxes Φ_n for $n = 1, 2, 3$ as generalized coordinates. Lagrange's equations (1.35) in this case take the form

$$\frac{\mathrm{d}}{\mathrm{d}t}\left(\frac{\partial E^{\mathrm{e}}}{\partial \dot{\Phi}_n}\right) + \frac{\partial D}{\partial \dot{\Phi}_n} - \frac{\partial E^{\mathrm{m}}}{\partial \Phi_n} = 0, \qquad n = 1,\, 2,\, 3,$$

where

$$E^{\mathrm{e}} = \frac{C_1}{2}\left(\dot{\Phi}_2 - \dot{\Phi}_1\right)^2 + \frac{C_2}{2}\left(\dot{\Phi}_3 - \dot{\Phi}_2\right)^2, \qquad E^{\mathrm{m}} = \frac{\Phi_1^2}{2L}.$$

$$D = \frac{\dot{\Phi}_1^2}{2R} + \frac{\dot{\Phi}_3^2}{2R_2} - \frac{\dot{\Phi}_2^2}{2}$$

$$\dot{\Phi}_2 = I(t)$$

We successively calculate

$$\frac{\partial E^{\mathrm{e}}}{\partial \dot{\Phi}_1} = -C_1\left(\dot{\Phi}_2 - \dot{\Phi}_1\right), \qquad \frac{\partial E^{\mathrm{e}}}{\partial \dot{\Phi}_2} = (C_1 + C_2)\,\dot{\Phi}_2 - C_1\dot{\Phi}_1 - C_2\dot{\Phi}_3,$$

$$\frac{\partial E^{\mathrm{e}}}{\partial \dot{\Phi}_3} = C_2\left(\dot{\Phi}_3 - \dot{\Phi}_2\right), \qquad \frac{\partial E^{\mathrm{m}}}{\partial \Phi_1} = \frac{\Phi_1}{L}, \qquad \frac{\partial D}{\partial \dot{\Phi}_1} = \frac{\dot{\Phi}_1}{R},$$

$$\frac{\partial D}{\partial \dot{\Phi}_2} = -I(t), \qquad \frac{\partial D}{\partial \dot{\Phi}_3} = \frac{\dot{\Phi}_3}{R_2}.$$

Eventually, from Lagrange's equations we obtain the following differential equations:

$$\ddot{\Phi}_1 - \ddot{\Phi}_2 + \frac{\dot{\Phi}_1}{R_1C_1} + \frac{\Phi_2}{C_1L} = 0,$$

$$-C_1\ddot{\Phi}_1 + (C_1 + C_2)\,\ddot{\Phi}_2 - C_2\ddot{\Phi}_3 = I(t),$$

$$-\ddot{\Phi}_2 + \ddot{\Phi}_3 + \frac{\dot{\Phi}_3}{R_2C_2} = 0.$$

As results we obtained the system of three non-autonomous linear differential equations, so the problem is more complex than it was in (a).

1.2 Dynamical Processes in Mechatronic Systems

Differential equations describing dynamical processes in mechatronic systems can be derived from one of Hamilton's principles, which for cases of mechanical and electrical systems was described respectively in Chaps. 3 and 4 of [3].

If we number independent mechanical generalized coordinates q_k using index k (K in total) and independent electrical generalized coordinates Q_n or Φ_n using index n (N in total), and if for the description of the electrical system as generalized coordinates we take charges Q_n, then the Lagrangian of a mechatronic system (mechanical and electrical) will take the form

$$L\left(q_k, \dot{q}_k, Q_n, \dot{Q}_n\right) = T_c + E^{\mathrm{m}} - V - E^{\mathrm{e}}. \tag{1.41}$$

The preceding equation describes the energy of conservative mechatronic systems, and the energy of non-conservative mechatronic systems is equal to

$$\delta W = \sum_{k=1}^{K} Q_k^F \delta q_k + \sum_{n=1}^{N} U_n \delta Q_n, \tag{1.42}$$

where Q_k^F denote generalized forces in the mechanical part of a mechatronic system.

Lagrange's equations in this case take the form

$$\frac{\mathrm{d}}{\mathrm{d}t}\left(\frac{\partial L}{\partial \dot{q}_k}\right) + \frac{\partial D}{\partial \dot{q}_k} - \frac{\partial L}{\partial q_k} = Q_k, \qquad k = 1, \ldots, K, \tag{1.43}$$

$$\frac{\mathrm{d}}{\mathrm{d}t}\left(\frac{\partial L}{\partial \dot{Q}_n}\right) - \frac{\partial L}{\partial Q_n} = U_n, \qquad n = 1, \ldots, N, \tag{1.44}$$

where Q_k in (1.43) denotes the generalized force (moment of force), Q_n in (1.44) the generalized charge as a generalized coordinate, and D the mechanical dissipation function.

If for the description of the electrical part we take as generalized coordinates the magnetic fluxes Φ_n, then the Lagrangian of conservative elements of a conservative mechatronic system is equal to

$$L\left(q_k, \dot{q}_k, \Phi_n, \dot{\Phi}_n\right) = T_c + E^{\mathrm{e}} - V - E^{\mathrm{m}}. \tag{1.45}$$

Variation in the work of non-conservative elements of a mechatronic system is equal to

$$\delta W = \sum_{k=1}^{K} Q_k \delta q_k + \sum_{n=1}^{N} I_n \delta \Phi_n. \tag{1.46}$$

In this case, Lagrange's equations have the form

$$\frac{\mathrm{d}}{\mathrm{d}t}\left(\frac{\partial L}{\partial \dot{q}_k}\right) + \frac{\partial D}{\partial \dot{q}_k} - \frac{\partial L}{\partial q_k} = Q_k, \qquad k = 1, \ldots, K, \tag{1.47}$$

$$\frac{\mathrm{d}}{\mathrm{d}t}\left(\frac{\partial L}{\partial \dot{\Phi}_n}\right) - \frac{\partial L}{\partial \Phi_n} = I_n, \qquad n = 1, \ldots N. \tag{1.48}$$

In Lagrange's equations associated with the mechanical part of the system described by (1.43) and (1.47), particular components of the Lagrangian were already described earlier in Chap. 3 of [3], whereas particular components associated only with the electrical part are described subsequently in this chapter.

1.2.1 Mechatronic Transducers

Important components of mechatronic systems are transducers of different types that transform electrical energy into mechanical energy and vice versa.

In applications, we deal with various transducers transforming one kind of energy into completely other kinds. This takes place especially in the metrology of mechanical quantities, where various dynamical processes are measured with electrical methods. Then the mechatronic transducer plays the role of a sensor; it is possible to distinguish two types of sensors.

Changes in mechanical processes generate in *modulating sensors (passive sensors)* changes in electrical quantities such as voltage, resistance, capacitance, inductance, current intensity, frequency of current, or phase shift.

One may distinguish the following *modulating sensors*:

(a) Resistive (resistance of the sensor depends on its geometry).
(b) Thermometric (resistance of the sensor depends on its temperature).
(c) Photoelectric (energy of radiation changes the sensor's resistance).
(d) Inductive (induction of the sensor depends on its geometry).
(e) Magnetoelastic (magnetic permeability of a ferromagnetic material depends on mechanical stress).
(f) Capacitive (capacitance of the sensor depends on its geometry, configuration of electrodes, and permittivity of the medium).

The second type of sensor includes *self-generating sensors (active sensors)* such as

(a) Dynamic (here the phenomenon of electromagnetic induction is used).
(b) Thermoelectric (here the phenomenon of generation of a thermoelectric force resulting from temperature difference is used).
(c) Piezoelectric (here the piezoelectric effect is used).

Later we will describe briefly some sensors that transform mechanical energy into electrical energy and vice versa, all the while focusing on the derivation of approximate mathematical models of such simple mechatronic systems.

1. *Resistive Displacement Transducers*
   Resistive displacement transducers transform linear or rotational displacement into constant or variable voltage of the current as a result of changes in resistance caused by the displacement. Figure 1.6 shows a schematic of such a transducer with linear displacement.
   According to Fig. 1.6 we have

$$I = I_1 + I_2, \quad R_1 + R_2 = R_0, \quad R_1/R_0 = x/l_0,$$
$$I_1 R_1 = I_2 R_3, \quad U_3 = R_3 I_2, \quad U_0 = I_1 R_2 + I_2 R_3. \tag{1.49}$$

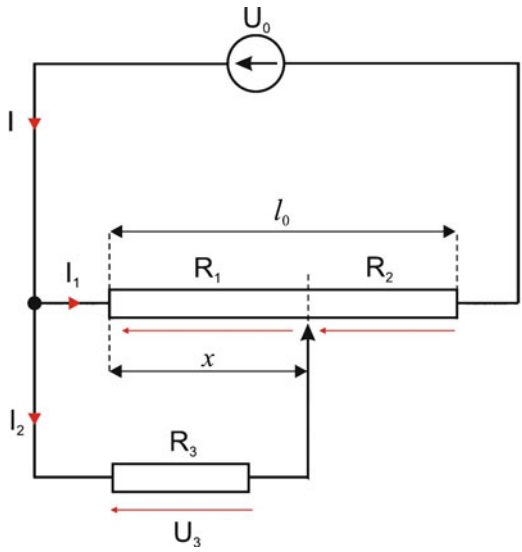

Fig. 1.6 Schematic diagram of a resistive linear displacement transducer

From the preceding equation we determine

$$U_3 = U_0 \frac{R_1}{R_0} \tag{1.50}$$

or, in equivalent form,

$$U_3 = U_0 \frac{x}{l_0}. \tag{1.51}$$

This means that the input signal x is proportional to the voltage U_3 measured on the resistor R_3.

2. *Resistance-based Sensors*
Resistance of a sensor is described by the equation

$$R = \frac{\rho l}{A}, \tag{1.52}$$

where ρ is the resistivity of the conductor material, l its length, and A its cross section. Resistance-based sensors include carbon sensors, fluid sensors, strain gauges, and others.

In the mechanics of deformable bodies for the measurement of stresses and displacements, strain gauges are commonly applied. If we glue a strain gauge onto the mechanical element being loaded, then, under the influence of stress, it changes its geometrical dimensions, and thus its resistance R changes according to (1.52).

Applying the logarithm function to both sides of (1.52), and then differentiating, we obtain

$$\frac{\mathrm{d}R}{R} = \frac{\mathrm{d}\rho}{\rho} + \frac{\mathrm{d}l}{l} - \frac{\mathrm{d}A}{A}. \tag{1.53}$$

Introducing a deformation sensitivity coefficient

$$\alpha = \frac{\mathrm{d}R}{R} \Big/ \frac{\mathrm{d}l}{l}, \tag{1.54}$$

from (1.53) we obtain

$$\alpha = 1 + 2\nu + \frac{\rho_r}{\varepsilon}, \tag{1.55}$$

where

$$\nu = -\frac{1}{2}\left(\frac{\mathrm{d}A}{A}\right) \Big/ \left(\frac{\mathrm{d}l}{l}\right), \quad \rho_r = \frac{\mathrm{d}\rho}{\rho}, \quad \varepsilon = \frac{\Delta l}{l}. \tag{1.56}$$

According to Hooke's law for a unidirectional state of deformation we have

$$\varepsilon = \frac{F}{EA}, \tag{1.57}$$

where E is Young's modulus of the resistive material and F is a tensile (compressive) force.

From (1.55), taking into account (1.54), (1.56), and (1.57), and replacing the differential operator with increment Δ, we obtain

$$\frac{\Delta R}{R} = \frac{F}{A}\frac{\alpha}{E} = C\sigma, \tag{1.58}$$

where $\sigma = F/A$ is the stress and $C = \alpha/E$ is constant for the given tensometer.

From (1.58) it follows that the relative change in resistance of the strain gauge is proportional to the change of stress existing in the sensor (the resistance wire).

3. *Inductive Transducers*

The operation of inductive transducers relies on changes in inductive resistance during the displacement of an armature Z outside the ferromagnetic core R, which is shown in Fig. 1.7.

If we take the displacement x for the input quantity, then through the coils of inductance L (according to Ohm's law) in the electric circuit will flow the current of intensity

$$I = \frac{U}{R_L} = \frac{U}{\sqrt{R^2 + (\omega L)^2}}, \tag{1.59}$$

where R_L is the inductive resistance and ωL the inductive reactance of the coil.

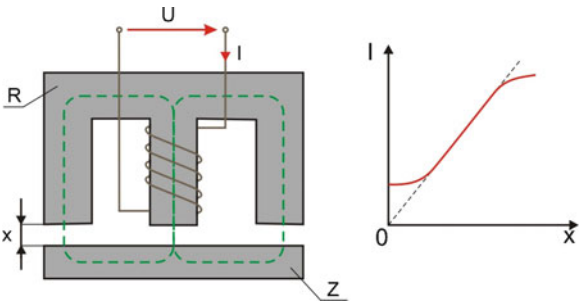

Fig. 1.7 Schematic diagram of an inductive transducer (**a**) and function $I(x)$ (**b**)

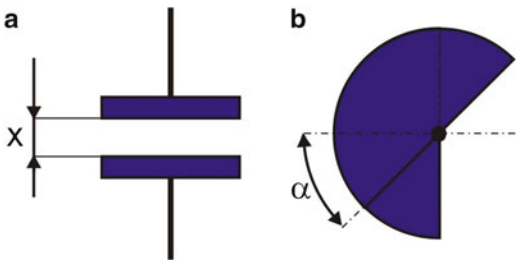

Fig. 1.8 Schematic diagram of a capacitive transducer of linear displacement (**a**) and angular displacement (**b**)

The inductance of the coil is equal to

$$L \cong \frac{0.2\pi N^2 A}{X} 10^{-8}, \tag{1.60}$$

where A denotes the cross-section area of the magnetic field and N is the number of turns of the coil winding. In practice $R \ll \omega L$, and in view of that $R_L \cong \omega L$. According to (1.59) we obtain

$$I(t) = \frac{Ux}{0.2\pi N^2 A\omega} 10^8 \equiv Cx(t), \tag{1.61}$$

where C is a constant characteristic for the given inductive sensor.

From (1.61) it follows that the current flowing in the coil winding is proportional to the air gap, and the ammeter measuring current intensity I can be calibrated directly in the units of gap length.

4. *Capacitive Transducers*

In a capacitive transducer, the input quantity is linear or angular displacement, and the output quantity is electrical capacitance (Fig. 1.8)

In the case of the schematic in Fig. 1.8a, the relationship $C(x)$ is described by the following equation:

$$C = \frac{\varepsilon A}{4\pi x}, \tag{1.62}$$

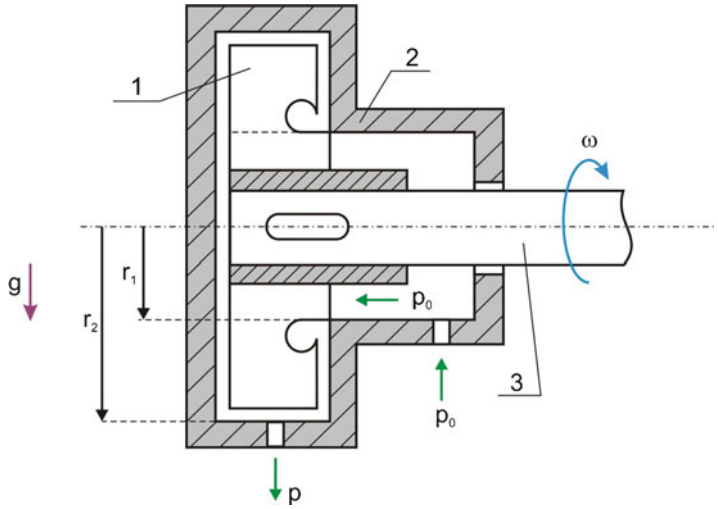

Fig. 1.9 Transducer for measurement of angular velocity ω

where ϵ is a dielectric constant, A denotes the active area of the capacitor, and x is the distance between capacitor plates.

In the case of the schematic from Fig. 1.8b we have

$$C = \frac{\varepsilon A}{4\pi d}\left(1 - \frac{\alpha}{\pi}\right), \tag{1.63}$$

where d is the distance between the rotor plates of the capacitor.

Capacitive sensors allow for a change in the capacitance not only by changes in the distance between plates (Fig. 1.8a) but also by changes in the active area of the capacitor plates or by the application of different dielectrics, e.g., air, or a layer of material of a different dielectric constant between the plates of the capacitor. Changes in mechanical quantities are registered through changes in the capacitance and then measured in an electrical measuring system. Capacitive sensors are characterized by a small force required for the displacement of the moving electrode of the sensor. Moreover, they enable contactless measurement and possess a small moving-electrode mass and large sensitivity.

5. *Angular Velocity Transducers*

An angular velocity transducer (Fig. 1.9) can be a mechanical part of a system, but, as distinct from the problems of the mechanics of a rigid body described so far, here we address the mechanics of fluid flow (a hydraulic transducer or gas flow transducer).

The measured angular velocity of shaft 3 is transmitted onto a paddle mixer 1 connected to casing 2. The pressure of a gas or liquid p_0 entering the working

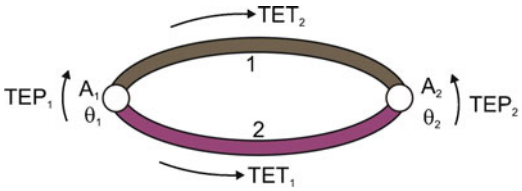

Fig. 1.10 Two conductors joined together (the thermocouple) and four thermoelectric forces

part of the angular velocity sensor passes through the paddle mixer, and at a hole in the casing the pressure p is seen, described by the equation

$$p = p_0 + \frac{\rho}{2g}\omega^2 \left(r_2^2 - r_1^2\right), \tag{1.64}$$

where ρ is the density of the medium

6. *Temperature Transducers*
   In this case, the change in resistance of a conductor R_Θ is associated with a change in temperature Θ according to the equation

$$R_\theta = R_0 \left(1 + \alpha \left(\theta - \theta_0\right)\right), \tag{1.65}$$

where R_0 is the resistance of the conductor at temperature Θ_0. The coefficient $\alpha[°C^{-1}]$ for iron is equal to 0.002–0.006, for aluminium 0.0045, and for carbon 0.0007.

Such a direct temperature measurement using temperature sensors called thermometers can span a range from −170°C to 700°C.

Also in use are *thermistors*, that is, semiconductors of large temperature coefficients of resistance. The dependency of resistivity (a specific resistance) of a thermistor on temperature is described by the equation

$$\rho_\theta = \rho_0 e^{(\alpha/\theta - \alpha/\theta_0)}, \tag{1.66}$$

where ρ_0 and ρ_Θ are the resistivities of a resistor corresponding to temperatures Θ_0 and Θ measured in degrees Kelvin, and α is a constant ($\sim 4,000$). Thermistors are used to measure temperature in a range of 60°C–120°C with an accuracy of up to 0.0005°C.

7. *Thermocouples*
   Thermocouples are used in various kinds of automatic control systems for the measurement of temperature. A thermocouple consists of two conductors, welded together, of different properties of resistance change vs. the measured temperature, e.g., one electrode is made of pure platinum and the other is an alloy of platinum (90%) and rhodium (10%). Such thermocouples can be used to measure temperatures reaching up to 1,600°C.

   If two metals 1 and 2 are joined together (Fig. 1.10) and their points of contact A_1 and A_2 are at different temperatures Θ_1 and Θ_2, then four thermoelectric

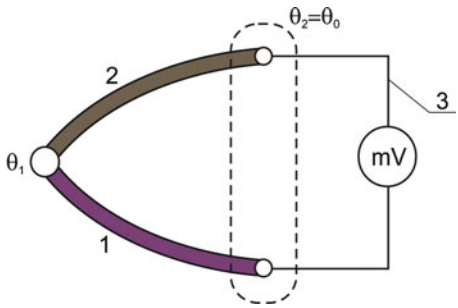

Fig. 1.11 A thermocouple (1, 2) forming a circuit with metal 3

forces e will appear in the closed circuit. "Cold" ends of the thermocouple are connected to the system of potentiometers, and the "hot" end is in contact with a medium (an element) whose temperature is to be measured.

Undesirable changes in ambient temperature affecting the cold ends of a thermocouple are compensated by introducing a bridge with a thermometer R_t that measures the temperature of the cold ends.

The force TEP_i is the *Peltier thermoelectric force* at the junction A_i and the force TET_i is the *Thomson thermoelectric force* in the wire i $(i = 1, 2)$. The net thermoelectric force is equal to

$$TE = TEP_1 - TEP_2 + TET_2 - TET_1. \tag{1.67}$$

Because of difficulties in the identification of particular Peltier and Thomson thermoelectric forces, the following equation is used:

$$TE = TE(\theta_1) - TE(\theta_2), \tag{1.68}$$

where $TE(\Theta_1)$ is the thermoelectric force at point A_1 (temperature Θ_1) and $TE(\Theta_2)$ is the thermoelectric force at point A_2 (temperature Θ_2).

In practice two metals 1 and 2 are used for temperature measurement by means of their connection to a meter (e.g., a millivoltmeter). In this way, an additional metal 3 is introduced into the circuit, and the measuring wires and internal circuit of the meter are made of this third metal (Fig. 1.11).

The thermoelectric force in the circuit shown in Fig. 1.11 is equal to

$$TE = TE_{12}(\theta_1) + TE_{23}(\theta_0) + TE_{31}(\theta_0). \tag{1.69}$$

Because for $\Theta = \Theta_0$ we have $TE(\Theta_0) = 0$, from (1.69) we obtain

$$TE_{23}(\theta_0) + TE_{31}(\theta_0) = -TE_{12}(\theta_0). \tag{1.70}$$

Substituting (1.70) into (1.69) we obtain

$$TE = TE_{12}(\theta_1) - TE_{12}(\theta_0). \tag{1.71}$$

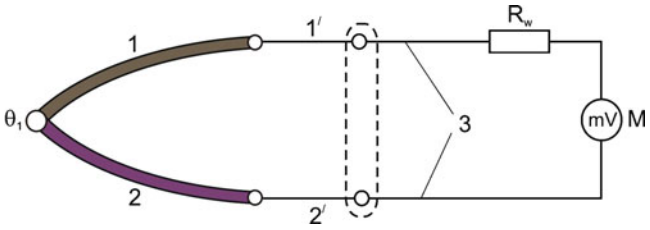

Fig. 1.12 Swing system applied to temperature measurement

The preceding equation holds on the condition that the introduction of a third metal into the system composed of metals 1 and 2 does not affect the value of the net thermoelectric force and both ends of metal 3 are at the same temperature.

The oldest, simplest, and the most commonly used system of thermoelectric thermometer in industry is the schematic of the so-called swing thermometer shown in Fig. 1.12.

In the schematic in Fig. 1.12, 1 and 2 denote thermoelements, $1'$ and $2'$ are compensating wires, R_w is the compensating resistor (selected in such a way that the external resistance of the meter $R_z = R_{zn}$, where R_{zn} is the nominal resistance of the meter, calibrated in degrees Celsius), and M is a millivoltmeter. The millivoltmeter M measures the voltage U, which is equal to

$$U = ET\frac{R_m}{R_z + R_m}, \tag{1.72}$$

$$R_z = R_{12} + R_{1'2'} + R_3 + R_w, \tag{1.73}$$

where R_{12} is the resistance of thermoelements 1 and 2, $R_{1'2'}$ is the resistance of compensating wires $1'$ and $2'$, R_3 is the resistance of connecting wires 3, and ET denotes the thermoelectric force of a thermoelement at the measured temperature Θ_1 and reference temperature Θ_0.

8. *Pressure Transducers*

Transducers for pressure measurement can be divided into two types. The first type includes transducers whose principal working elements are mechanical elastic elements, the deformations of which are transformed into electrical signals using capacitive elements, inductive elements, or strain gauges.

The second type includes transducers where the main working elements are magnetoelastic cylinders.

Figure 1.13 shows examples of sensors of the first type for measurement of pressure of a flowing gas (a) and liquid (b).

The bellows sensor for pressure measurement of a gas consists of a tube of undulating shape (a bellows) 1, a rack 2, and a pinion 3 connected to the terminal of the potentiometer 4. The pressure p causes stretching of the bellows 1 and displacement of the rack 2, and consequently a change in position

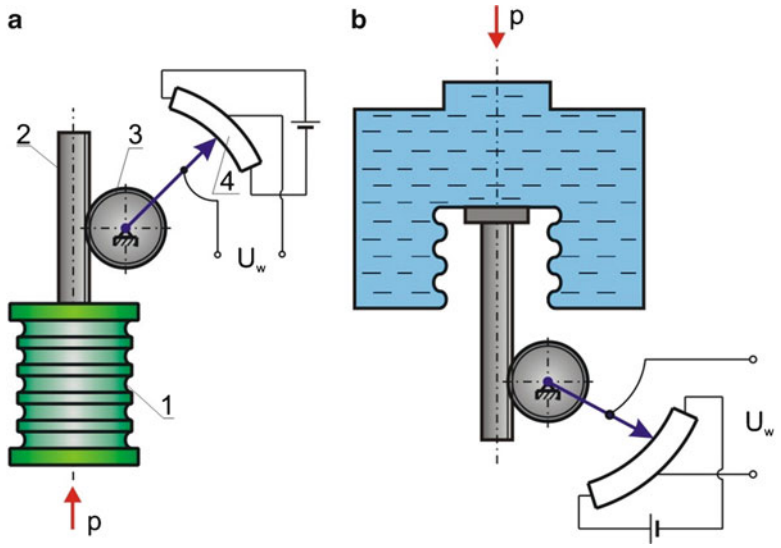

Fig. 1.13 Schematic diagram of pressure sensor of a flowing gas (**a**) and flowing liquid (**b**)

of the potentiometer terminal, which leads to a change in output voltage U_w. On the assumption that the relationship $U_w(p)$ is linear, the equation connecting the output voltage and the pressure has the form

$$U_w = \alpha p, \tag{1.74}$$

where α is a proportionality factor. Displacement of the rack x can be determined after solution of the following second-order differential equation:

$$M\ddot{x} + c\dot{x} + kx = Ap, \tag{1.75}$$

where M denotes the mass of moving parts of the sensor, c is the viscous damping coefficient, k denotes bellows stiffness, and A is the cross-section area of the bellows. The problem can be reduced to a model of second-order inertial elements of the form (see Chap. 6 of [3])

$$T^2\ddot{x} + 2\xi T\dot{x} + x = \alpha p, \tag{1.76}$$

where $T = \sqrt{\frac{M}{k}}$, $\xi = \frac{c}{2\sqrt{kM}}$, $\alpha = \frac{A}{k}$, and the right-hand side of this equation is equal to U_w [see (1.74)].

Equation (1.76) describes also the dynamics of the meter from Fig. 1.11b, and in this case the bellows is filled up with a liquid.

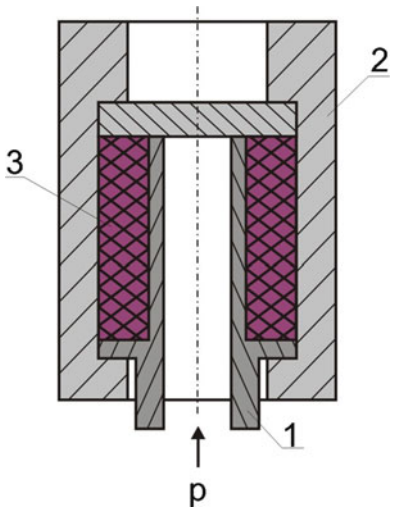

Fig. 1.14 Magnetoelastic element of a pressure sensor

9. *Magnetoelastic Sensors*
   In Fig. 1.14 the schematic of a magnetoelastic element of a (second type) transducer for pressure measurement is shown.

   Axial forces acting on a ferromagnetic element cause a change in the magnetic permeability of this element. The steel pipe 1 was covered with a pipe made of invar alloy. Inside was placed a choking coil 3. The pressure p causes expansion of the pipe 2, which leads to a change in the magnetic permeability of invar μ, which in turn affects the value of self-inductance of the coil according to the equation

$$L = 0.4\pi N^2 10^{-8} \frac{\mu A}{l}, \tag{1.77}$$

   where N is the number of coil turns, A denotes the cross-section area of the invar pipe, and l is its length. The coil is connected to a bridge, and the change in inductance of the coil results in a change in current intensity proportional to the pressure magnitude.

   The measuring ammeter can be directly calibrated in units of force. Magnetoelastic sensors are also used for the measurement of large static and dynamic forces. The magnetoelastic effect apart from the aforementioned invar is also characteristic of nickel, permalloy, and iron.
10. *Piezoelectric Transducers*
    The piezoelectric effect discovered in 1880 by Marie and Pierre Curie consists in the generation of electric charges on faces of crystals loaded with tensile or compressive forces (e.g., quartz, Seignette's salt, or barium titanate).

In Fig. 1.15 the frequency response of a piezoelectric sensor is shown.

Because the force acting on a sensor plate is usually produced by a moving element of mass m, the signal obtained from the sensor is proportional to the

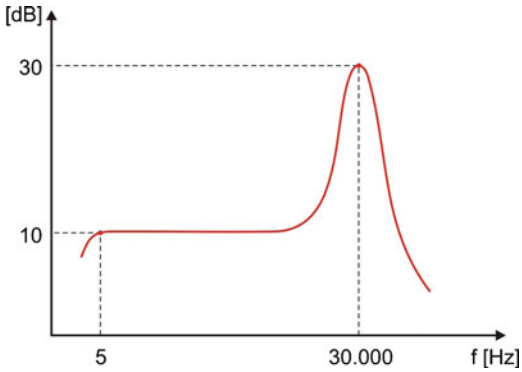

Fig. 1.15 Frequency response of a piezoelectric sensor

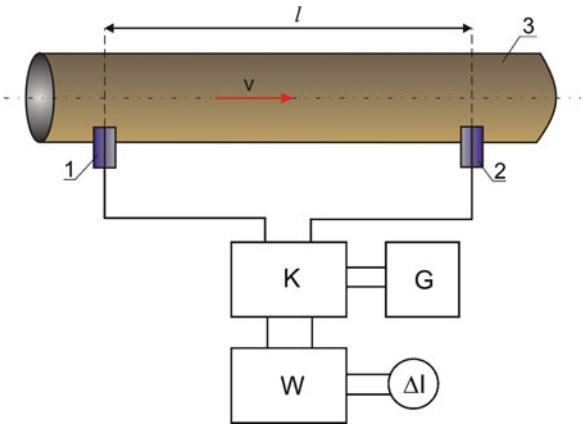

Fig. 1.16 Measurement of flow energy losses by means of piezoelements

acceleration of this element. The operating range of the sensor is 1–300 Hz, and the resonance frequency of this sensor is equal to about 30 kHz.

Piezoelectric sensors have a very wide range of application for the measurement of frequency and acceleration. Their disadvantage is the requirement of dynamic calibration.

The application of piezoelectric transducers is broad, but here we will limit ourselves to determining the loss of energy of fluid flow on the basis of determining the difference in propagation velocity of ultrasonic vibrations. Figure 1.16 shows a schematic of measurement of energy loss of the fluid flowing in pipe 3 with velocity v between two piezoelements 1 and 2 separated by distance l.

The generator G and the phase amplifier are alternately switched in by a commutator K in such a way that the piezoelements act at first as transmitters (radiators) and then as receivers of energy.

The instantaneous voltage of the radiating piezoelement

$$U_1 = U_{10} \sin \omega t, \tag{1.78}$$

and the instantaneous voltage on the receiving piezoelement is equal to

$$U_2 = U_{20} \sin \omega \left(t - T\right), \tag{1.79}$$

where T denotes the time it takes the ultrasonic wave to cover distance l.

The phase difference between a steady-state vibration regime (when the medium is stationary) and vibration of a fluid is equal to

$$\Delta\varphi_1 = \frac{l\omega}{c - v}, \tag{1.80}$$

and the difference between the standard vibration and a vibration whose sense is opposite to the velocity of the fluid v is equal to

$$\Delta\varphi_2 = \frac{l\omega}{c + v}, \tag{1.81}$$

where c is the velocity of propagation of ultrasound in the fluid and v is the velocity of the fluid.

The phase difference is equal to

$$\Delta = \Delta\varphi_1 - \Delta\varphi_2 = \frac{2\omega l v}{c^2 - v^2} \cong \frac{2\omega l v}{c^2} \tag{1.82}$$

for $c \gg v$. The voltage of the piezoelement will be inversely proportional to velocity, that is,

$$U_1 = \frac{\alpha}{c + v}, \qquad U_2 = \frac{\alpha}{c - v}, \tag{1.83}$$

where α is a proportionality factor. The values of current intensities in the amplifier are equal to

$$I_1 = \frac{\alpha_1 \left(c + v\right)}{\alpha}, \qquad I_2 = \frac{\alpha_1 \left(c - v\right)}{\alpha}, \tag{1.84}$$

hence we calculate

$$\Delta I = I_1 - I_2 = \beta v, \tag{1.85}$$

where $\beta = \frac{2\alpha_1}{\alpha}$ is a proportionality factor. From this the conclusion follows that for a constant volume of the pipe through which the fluid flows, losses of the flow will be proportional to the velocity of the flowing fluid.

1.2.2 Magnetic Force in a Single Mechatronic System

This problem was already partly considered in the section concerning inductive transducers. Let the single mechatronic system consist of a magnet core (1) with wounded coil of N turns (2), and armature (3), shown in Fig. 1.17.

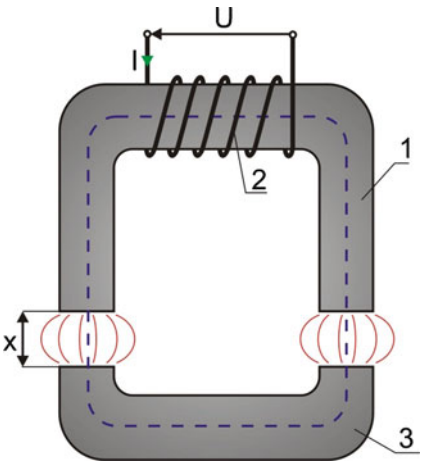

Fig. 1.17 Schematic diagram of a magnetic circuit in system of core (1), armature (3), and two air gaps

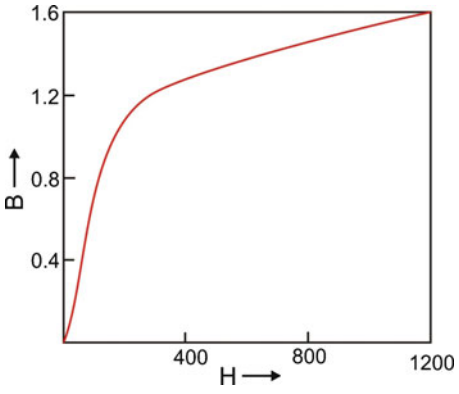

Fig. 1.18 $B(H)$ dependency for ARNON material used for transformer plates

The aim of these considerations is the determination of a magnetic force that attracts the armature (3) to the electromagnet (1) as a function of the current intensity I in the coil, the width of the air gap x, the cross-section area of core A, the length of the ferromagnetic part of the magnetic circuit l_r, and the number of turns of coil winding N. We will neglect the hysteresis phenomenon in the core and assume the magnetic permeability of the air to be equal to magnetic permeability of vacuum. The magnetic induction $B(T)$ generated in the circuit depends on the magnetic field H[A/m], for example, as presented in Fig. 1.18.

Let us note that the function $B(H)$ is bijective, making it is easy to build the inverse function $H(B)$. The aforementioned non-linear functions can be described after the introduction of relative permeability $\mu = \mu(B)$ or $\mu = \mu(H)$, and the function $B(H)$ takes the form

$$B = \mu(H)\mu_0 H, \tag{1.86}$$

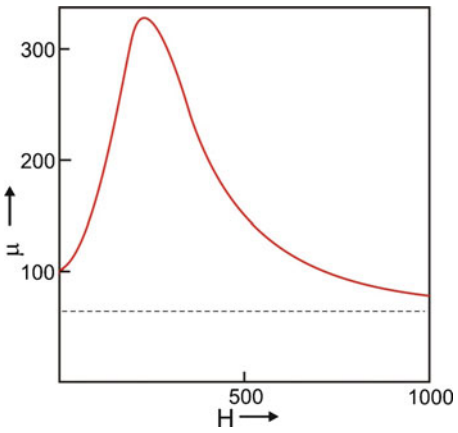

Fig. 1.19 Example of $\mu(H)$ dependency for ARNON material

where μ_0 is the vacuum permeability and is equal to $\mu_0 = 4\pi \cdot 10^{-7}\,[\frac{\mathrm{Vs}}{\mathrm{Am}}]$. A sample plot of the function $\mu(H)$ is shown in Fig. 1.19.

Let us note that $\lim_{H\to\infty} \mu(H) = 1$. From Kirchhoff's voltage law for a magnetic circuit from Fig. 1.18 we obtain

$$I(t) = \frac{(2R_{sz} + R_r)\,\Phi\,(t)}{N} \tag{1.87}$$

$$R_{sz} = \frac{x}{\mu_0 A}, \qquad R_c = \frac{l_r}{\mu_0 \mu A}, \tag{1.88}$$

where R_{sz} (R_r) denotes respectively the *reluctance* of two air gaps (reluctance of the ferromagnetic core and the armature) and $\Phi = \Phi[\mathrm{Tm}^2]$ is the magnetic flux, assumed to be uniform at each point of a magnetic circuit.

From (1.87) we obtain

$$I(t) = \frac{1}{\mu_0 A N}\left(2x + \frac{l_r}{\mu}\right)\Phi\,(t)\,, \tag{1.89}$$

hence

$$\frac{\Phi}{A} = \mu_0 N I \left(\frac{1}{2x + \frac{l_r}{\mu}}\right). \tag{1.90}$$

Because the magnetic flux

$$\Phi = BA, \tag{1.91}$$

from (1.91) and (1.90) we obtain

$$B = \frac{\Phi}{A} = \frac{\mu_0 I N}{2x + \frac{l_r}{\mu(B)}}. \tag{1.92}$$

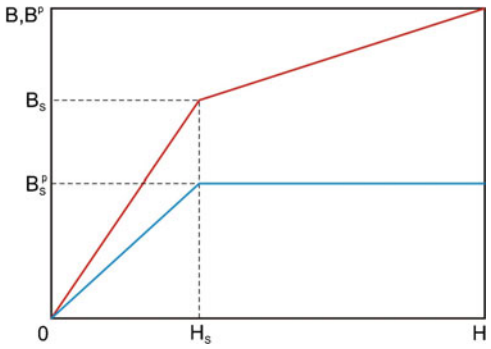

Fig. 1.20 Bilinear characteristics of $B^{\mathrm{p}}(H)$ and $B(H)$

Equation (1.92) is a non-linear algebraic equation, where for fixed parameters we determine function B by means of numerical calculations. From (1.92) and exploiting (1.86) we obtain

$$H = \frac{NI}{2x\mu\,(H) + l_r}. \tag{1.93}$$

Knowing function H [determined numerically from (1.93)] we determine its corresponding value of magnetic induction from (1.86).

Assuming a uniform magnetic field strength in the air gap, denoted H_0, the potential energy accumulated in the gap is equal to

$$V\,(x) = \frac{A}{2}\int_0^x B\,H_0 \mathrm{d}x. \tag{1.94}$$

The desired force acting on the armature is equal to

$$F = 2\frac{V\,(x)}{\partial x} = AB\,H_0 = \frac{AB^2}{\mu_0}, \tag{1.95}$$

where during transformations (1.86) and the value $\mu(H_0) = 1$ were used.

The relationship $B(H)$ presented in Fig. 1.18 and the so-called *phenomenon of magnetic polarization of the core* B^{p} as a function of H allow for the introduction of a bilinear magnetization curve. Since it turns out that with an increase of H polarization increases linearly and after passing the value H_{s}, the value of the polarization reaches a constant value $B^{\mathrm{p}} = B_{\mathrm{s}}^{\mathrm{p}}$ for $H \geq H_{\mathrm{s}}$ [1]. Assuming a simplified magnetization model, both $B(H)$ and $B^{\mathrm{p}}(H)$ have the bilinear characteristics shown in Fig. 1.20.

Piecewise linear changes in magnetic induction $B(H)$ and $B^{\mathrm{p}}(H)$ allow for the introduction of the following simplified equation:

$$B = \mu_0 H + B^{\mathrm{p}}. \tag{1.96}$$

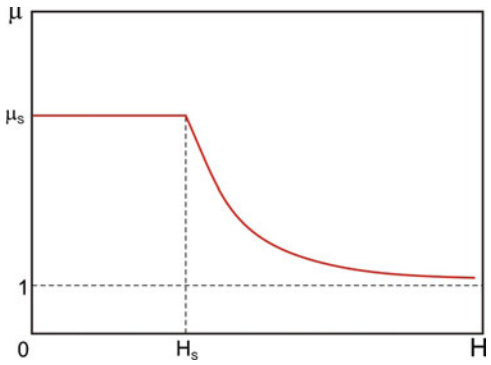

Fig. 1.21 Function of relative magnetic permeability $\mu(H)$ corresponding to the bilinear magnetization curve

The quantities H_s (saturation magnetic field strength), B_s^p (saturation polarization), and B_s (saturation induction), shown in Fig. 1.20, can be taken as material constants. Finally, the approximation of characteristics $B(H)$ can be conducted based on two material constants B_S and H_S, and its bilinear approximation has the form

$$\begin{aligned} B\,(H) &= \frac{B_\mathrm{s}}{H_\mathrm{s}} \quad \text{for} \quad 0 \le H \le H_\mathrm{s}, \\ B\,(H) &= B_\mathrm{s} + \mu_0\,(H - H_\mathrm{s}) \quad \text{for} \quad H > H_\mathrm{S}. \end{aligned} \tag{1.97}$$

To point $B_S(H_S)$ corresponds $\mu_S = \frac{B_S}{\mu_0 H_S}$, and the relative permeability $\mu = \mu(H)$ is described by the two equations

$$\begin{aligned} \mu\,(H) &= \mu_s \quad \text{for} \quad 0 \le H \le H_\mathrm{s}, \\ \mu\,(H) &= 1 + \frac{H_\mathrm{s}\,(\mu_s - 1)}{H} \quad \text{for} \quad H > H_\mathrm{S}, \end{aligned} \tag{1.98}$$

shown in Fig. 1.21.

Kirchhoff's voltage law when the bilinear approximation is used will take the following form:

$$NI = \frac{2x}{\mu_0}B + \begin{cases} l_r \frac{H_\mathrm{s}}{B_\mathrm{s}} B & \text{for} \quad B \le B_\mathrm{s}, \\ l_r \left[\frac{B}{\mu_0} + H_\mathrm{s} - \frac{B_\mathrm{s}}{\mu_0}\right] & \text{for} \quad B > B_\mathrm{s}. \end{cases} \tag{1.99}$$

The desired magnetic force is equal to

$$\begin{aligned} F &= \mu_0 A N^2 \frac{I^2}{\left(2x + \frac{l_r}{\mu_s}\right)^2} \quad \text{for} \quad \frac{\mu_0 N I}{2x + \frac{l_r}{\mu_s}} \le B_\mathrm{s}, \\ F &= \mu_0 A \frac{\left(NI + l_r\left(\frac{B_\mathrm{s}}{\mu_0} - H_\mathrm{s}\right)\right)^2}{(2x + l_r)^2} \quad \text{for} \quad \frac{\mu_0 N I}{2x + \frac{l_r}{\mu_s}} > B_\mathrm{s}. \end{aligned} \tag{1.100}$$

The simplification often used during the analysis of electromagnetic circuits is the assumption that $2x\mu \ll l_r$, which in many cases is justified, especially for small values of x. In this case from (1.93) we obtain

$$H = \frac{NI}{l_r}, \tag{1.101}$$

and in turn from (1.92) we get

$$B = \frac{\mu_0 NI}{2x + \frac{l_r}{\mu(I)}}. \tag{1.102}$$

The force acting on the armature, according to (1.95), is equal to

$$F = A\frac{\mu_0 N^2 I^2}{\left(2x + \frac{l_r}{\mu(B)}\right)^2}. \tag{1.103}$$

According to Kirchhoff's voltage law, the relationship between the voltage supplying the circuit U and the current intensity in circuit I has the form

$$U = IR - N\frac{\mathrm{d}\Phi}{\mathrm{d}t}, \tag{1.104}$$

where R is the resistance of the winding.

However, in the case under consideration, now changes in the magnetic flux Φ are the result of changes in both the current intensity and the width of the air gap x. Differentiating (1.91) we have

$$\dot{\Phi} = A\dot{B}, \tag{1.105}$$

where, according to (1.102), we have

$$\dot{B} = \mu_0 N\left[\frac{\dot{I}}{2x + \frac{l_r}{\mu(B)}} - \frac{2I\dot{x}}{\left(2x + \frac{l_r}{\mu(B)}\right)^2} + \frac{\dot{B}\frac{\mathrm{d}\mu}{\mathrm{d}B}\frac{l_r}{\mu^2(B)}}{\left(2x + \frac{l_r}{\mu(B)}\right)^2}\right]. \tag{1.106}$$

Complete coupled non-linear algebraic-differential equations describing the electromagnetomechanical (mechatronic) circuit from Fig. 1.17 have the form

$$\begin{aligned} U &= IR - NA\dot{B}, \\ B &= \frac{\mu_0 NI}{2x + \frac{l_r}{\mu(B)}}, \end{aligned} \tag{1.107}$$

and the force F acting on the armature is described by (1.95). If the field strength H is proportional to the current intensity I, then the preceding (1.107) are reduced to one equation of the form

$$U = IR - \frac{\mu_0 NA}{\left(2x + \frac{l_r}{\mu(I)}\right)^2}\left[2x + \frac{l_r}{\mu(I)} + \frac{I l_r}{\mu^2(I)}\frac{\mathrm{d}\mu}{\mathrm{d}t}\dot{I} - 2I\dot{x}\right], \tag{1.108}$$

where $U = U(t)$ is the voltage applied to the mechatronic system. The force F exerted by the electromagnet on the armature is described by (1.103), where the function $\mu = \mu(I)$ occurs in the denominator.

1.3 Magnetic Levitation

Magnetic levitation is a known topic and can be realized in several ways [4–6], but the most spectacular effects can be observed when an electromagnet made of superconductor is used. A simpler way to create a system for the investigation of the levitation phenomenon is to use a system with an infrared light sensor (barrier) that traces the position of the levitating mass placed in the magnetic field generated by the electromagnet.

For the purpose of the experiment presented here the role of sensor is played by the infrared light barrier, which traces the actual position of the cylindrical mass (Fig. 1.22).

The development toward future applications of fast and accurate position control systems used in optoelectronics, computer hardware, precision machining, robotics, and automotive has stimulated high-level engagement in the creation of non-conventional implementations [6, 7]. In this section, a numerical analysis devoted to that domain concerning non-contact (frictionless) fixing of some cylindrical mass

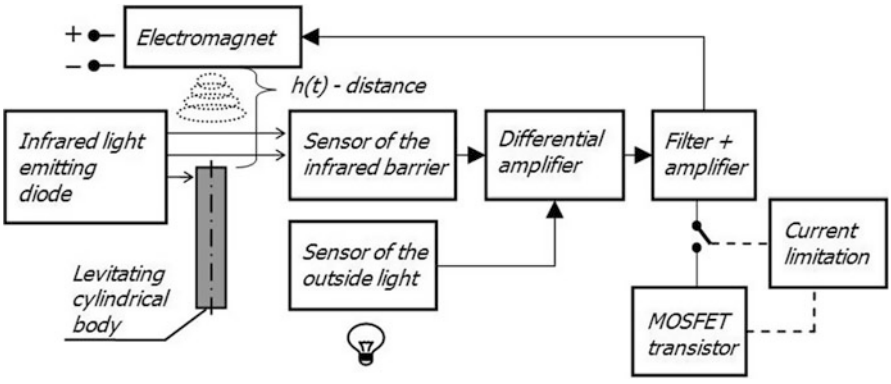

Fig. 1.22 Schematic block diagram of hardware, signal connections, and levitating solid body

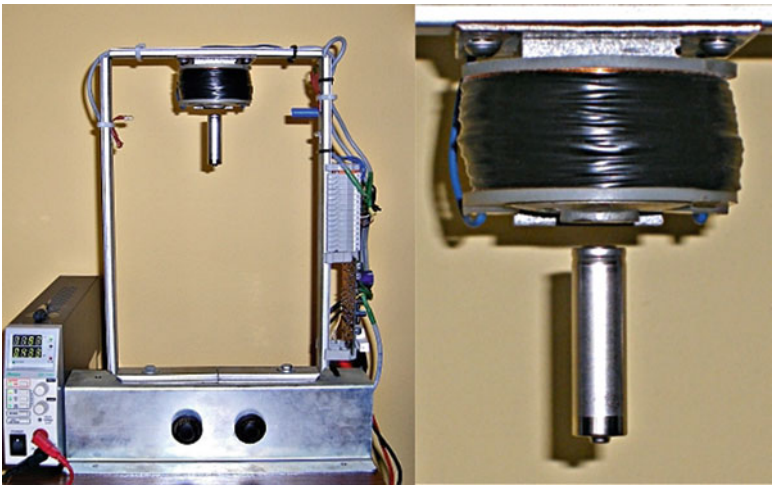

Fig. 1.23 Experimental setup of control system of levitating cylindrical light mass (constructed by Piotr Jędrzejczyk, student of second-degree studies at the Faculty of Mechanical Engineering of the Technical University of Lodz, Poland)

in an alternating magnetic field is carried out [8]. The calculations given are an introductory step to the identification of electromagnet parameters and magnetic fields in the experimental realization of the problem, shown in Fig. 1.22. The mass levitates in the field generated by the electromagnet system supplied by a voltage of 12 V. Next to the numerical algorithm of voltage feedback there a modified PID control [7] of transient oscillations of the levitating light mass was also used. These were recorded until it reached a stable equilibrium position. The results of the experiments are presented on time plots of displacement $h(t)$ measured between the opposite facing surfaces of the electromagnet core and the top surface of the levitating mass.

1.3.1 The Analyzed System

The electronic part of the system uses two light-sensitive resistors, the first one of which acts together with an infrared-light-emitting diode as a simple barrier tracing the cylindrical solid body position. Due to the existence in the surrounding space of many infrared-light-emitting sources such as the sun or lightbulbs (producing disturbance signals to the barrier), the second resistor measures the amount of light coming into the system from the surrounding space. If the barrier sensor is only partially illuminated (the result of being obstructed by the levitating body), the voltage difference appears and is input to the differential amplifier for the generation of the updated value of voltage supplying the electromagnet circuit. Experimental realization of the schematic diagram presented in Fig. 1.22 is shown in Fig. 1.23.

The system shown in Fig. 1.23 can be modeled by a dynamical system of three first-order differential (1.109) describing the motion of the mass levitating in magnetic and gravitational fields and the voltage equation for the electric circuit with alternating current. The meaning of the elements of the system-state vector $\mathbf{x}$ is as follows: $x_1 \to h$ is the displacement of the levitating mass measured downward from the electromagnet surface, $x_2 \to \mathrm{d}h/\mathrm{d}t$ the corresponding velocity of the displacement, and $x_3 \to i$ the electric current in the electromagnet electric circuit.

The governing equations follow:

$$\begin{aligned}
\dot{x}_1(t) &= x_2(t), \\
\dot{x}_2(t) &= g - \frac{k}{m}\left(\frac{x_3(t)}{x_1(t)}\right)^2 + u(t)\,\big|_{1\,\mathrm{case}}, \\
\dot{x}_3(t) &= \frac{1}{L}\left(v(t)\,\big|_{2\,\mathrm{case}} - Rx_3(t)\right),
\end{aligned} \tag{1.109}$$

where the electrical and physical constants are as follows: $L = 0.002\,H$ is the coefficient of inductance, $R = 0.29\,\Omega$ the coefficient of resistance, $k = 10^{-4}\,\mathrm{kg}\cdot\mathrm{m}^2/\mathrm{C}^2$, C the magnetic flux, $m = 0.0226\,\mathrm{kg}$ the mass of the levitating body.

1.3.2 Two Cases of Numerical Control

Voltage $v(t)$ and force excitation $u(t)$ are the two control signals. They are considered in two separate cases, namely: (1) $u(t)$ is feedback from position h in the system with a *PID* controller having the transfer function $\mathrm{PID}(s) = k_P + (s + k_I)/s + k_D s$ inserted into the first axis of the block diagram shown in Fig. 1.24, while $v(t)$ is a constant voltage source of 12 V; (2) a time-dependent control input voltage having the Laplace representation $V(s) = -((k_1 + k_2 s + k_3 s^2)H(s) - k_1 h_0)$ to the analyzed dynamical system working as the plant in the closed-loop control system with feedback from the full state vector (a numerical model of the control strategy is shown in Fig. 1.25). Disturbances coming from any external light sources have been neglected.

Both of the numerical models presented contain characteristics of the operation of an infrared light barrier $\mathrm{IRR}(t) = 1 - b_{\mathrm{IRR}} h(t)^{-2}$. This approximation with damping (sensitivity) constant b_{IRR} measures the amount of infrared light transferred from the emitting diode to the light-sensitive resistor with the levitating body serving as the barrier.

Figure 1.26 shows the well-studied effect of introducing an infrared light barrier. The case for a short range of values of the IRR factor was described as the correct one, being more realistic in relation to the motion of mass m observed on the experimental rig. During this experiment one tries to fix the mass at height $h_f = 1\,\mathrm{cm}$ with the initial condition $h_0 = 3\,\mathrm{cm}$. It is clear that the mass is quickly attracted to the steady-state position but is achieved in a different manner.

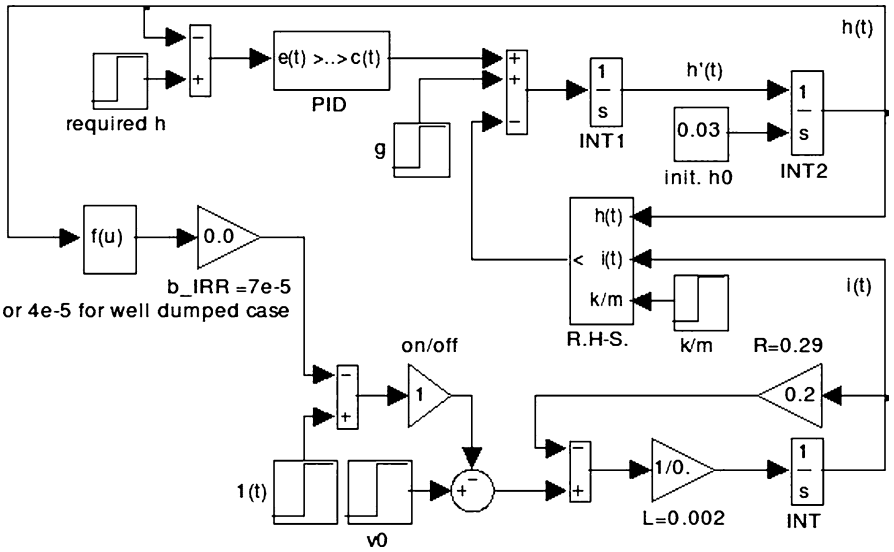

Fig. 1.24 Feedback from displacement of levitating mass in *PID* control for $k_P = 250, k_I = 800, k_D = 13$

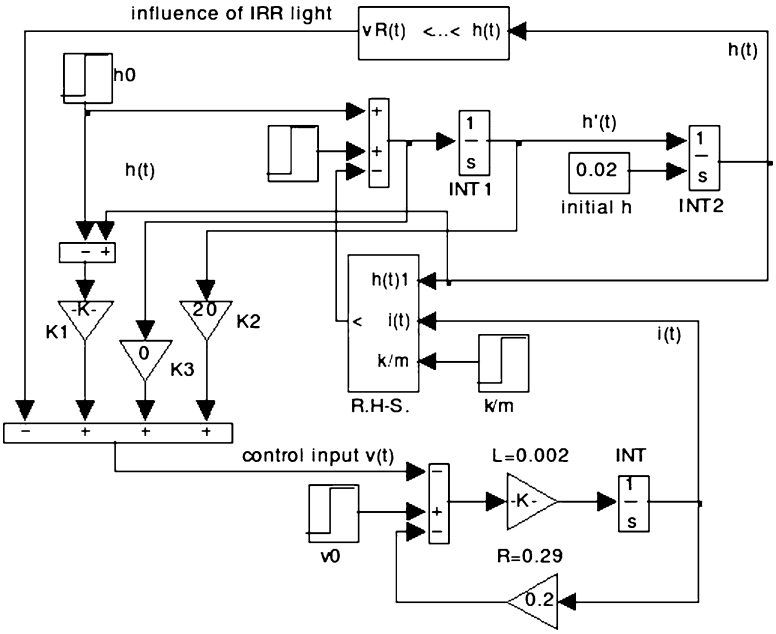

Fig. 1.25 Closed-loop input voltage control with use of full state-vector feedback for $k_1 = 10^3$, $k_2 = 20$, $k_3 = \{0.0, 0.2\}$ in a model made in Simulink

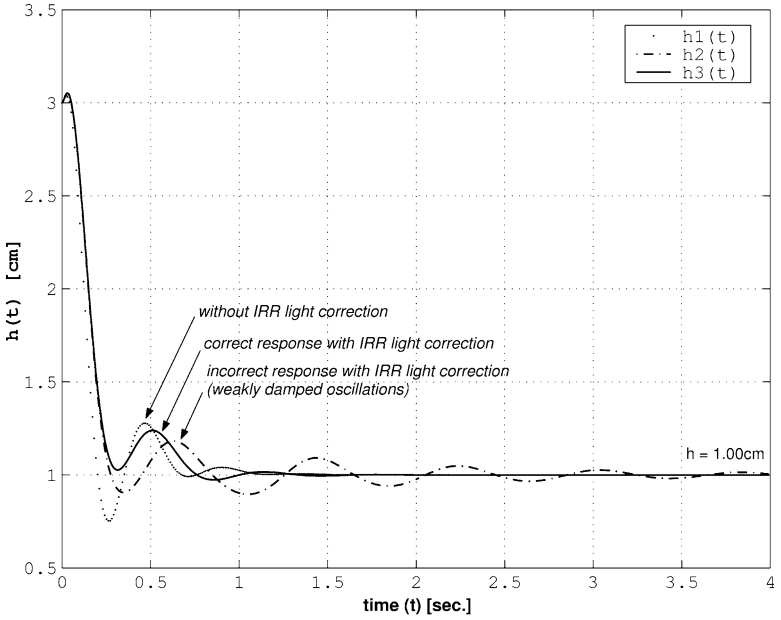

Fig. 1.26 Time plots of $h(t)$ obtained from diagram shown in Fig. 1.24 for different values of the infrared light barrier factor $b_{\mathrm{IRR}\{1,2,3\}} = \{\text{IRR off}, 0.7 \cdot 10^{-4}, 0.4 \cdot 10^{-4}\}$ in the closed-loop position feedback control and for $h_0 = 3\,\mathrm{cm}$

Frictionless oscillations in the transition to a stable position can be damped very well (Fig. 1.27) with the use of the second case of the control strategy based on feedback from the full state vector, as shown in Fig. 1.25. For a different initial position ($h_0 = 2\,\mathrm{cm}$) of mass m there is visible a quicker (because of the voltage, not external force feedback, as examined in the first approach) and better damped attraction of the mass to the steady-state position. With respect to application of a different method of control (with a control with feedback to the voltage time variable input v), the whole system is characterized by a slightly different dynamics, so the position of convergence changes with the use of larger values of $b_{\mathrm{IRR}\{1,2,3\}} = \{7, 0.7, 22.2\} \cdot 10^{-4}$. Factor $b_{\mathrm{IRR}\{3\}}$ is the highest available here, and the control nicely fixes the levitating mass at $h_3 = 1.67\,\mathrm{cm}$. At this position the stabilized voltage supplying the electromagnet equals 13.66 V. The time plot of h_4 in Fig. 1.27 is an unnatural effect of a non-zero coefficient of feedback from acceleration ($k_3 = 0.2$; see Fig. 1.25). The desired position is achieved in about 1.2 s, and it confirms that the vector component of feedback from acceleration is not necessary in this application.

Depending on the presence of an IRR light barrier and the values of its sensitivity factor (b_{IRR}), various shapes of the step response can be distinguished. The convergence is quite fast and well damped when the IRR light correction exists and, additionally, takes a correct value of its significance. The choice of incorrect value of b_{IRR} results in the mass being brought into small-amplitude, weakly damped

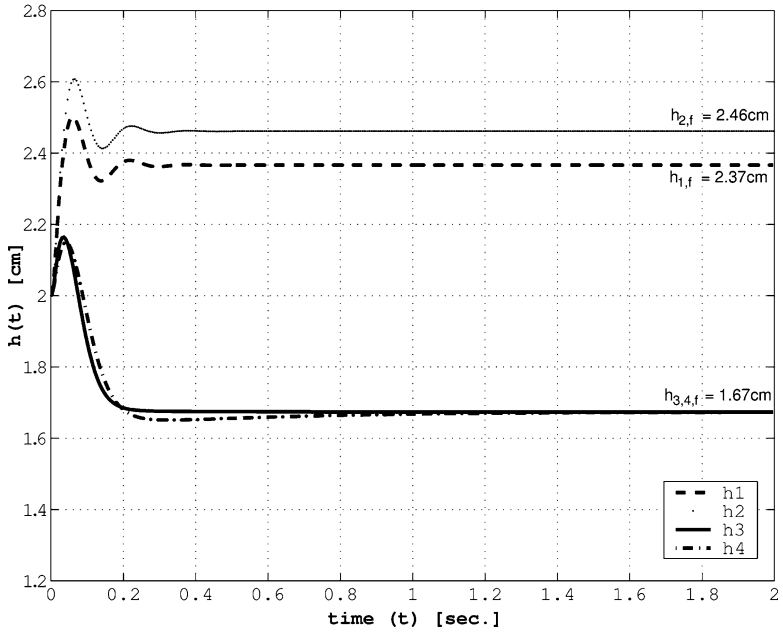

Fig. 1.27 Time plots of $h(t)$ evaluated from diagram shown in Fig. 1.25 for different values $b_{\mathrm{IRR}\{1,2,3\}} = \{7,\ 0.7,\ 22.2\} \cdot 10^{-4}$ corresponding to $h_{\{1,2,3\}}$ (for $k_3 = 0$), respectively. Infrared light sensitivity factor $b_{\mathrm{IRR}\{4\}} = b_{\mathrm{IRR}\{3\}}$ (for $k_3 = 0.2$), and $h_0 = 2\,\mathrm{cm}$

oscillations about its desired steady-state position. In some conditions, such an effect is observable also at a real laboratory rig and is undesirable if we need to fix the levitating mass at a constant height. Therefore, the introduced feedback from the infrared light barrier with mass m working as the armature of the electromagnet is justified. Better shapes of characteristics of the transition to steady-state responses were confirmed by the second control strategy. They are faster and more stable, and no oscillations are reported after examination of system parameters. The magnetic field allowed for elimination of any kinds of friction that are usually required in various realizations of fixings. Our experimental investigations will turn to the identification of electromagnetic parameters of the complete mechatronic system and the associated magnetic field. This is expected to help improve both the numerical adequacy of the presented approach and the tested strategy of control.

1.4 String-Type Generator

The dynamics of non-linear discrete-continuous systems governed by ordinary differential equations and partial differential equation often causes difficulties in numerical analysis. The reason lies not only in non-linear terms but mainly in time-consuming numerical techniques used to find the solution of the partial

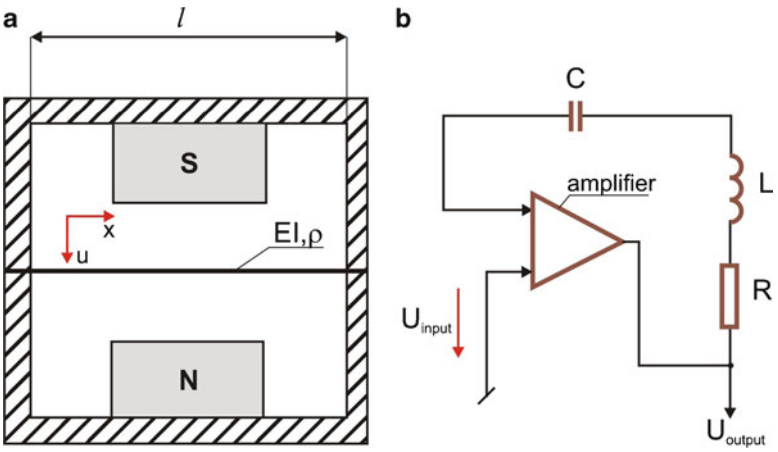

Fig. 1.28 Scheme of string embedded in magnetic field (**a**) and electrical model (**b**)

differential equations. Furthermore, usually real physical systems possess many parameters that can be changed over wide regions, and in practice direct simulation of the governing equations is costly and very tedious. Sometimes it does not provide physical insight into the obtained results. A deeper understanding of the dynamical behavior of the system under consideration can be discovered by the application of appropriate scaling and the proper use of averaging techniques [9–11]. In this section the electromechanical system under consideration serves as an example for a systematic strategy for solving many other related problems encountered in non-linear mechanical, biological, or chemical dynamical systems. First, an averaging method is proposed that is supported by a program for symbolic computation, and then further systematical study of the obtained ordinary differential equations is developed.

1.4.1 Analyzed System

The electromechanical model under consideration consists of a distributed mass system (string) whose oscillations are governed by a PDE (a detailed discussion of the model is given in [12–14]). The string is embedded in the magnetic field and crosses a magnetic flux perpendicularly (Fig. 1.28a). On the other hand, the string is made of steel and has its own inductance L, resistance R, and capacitance C. It appears that the equilibrium position of the string is unstable. The existence of the magnet induction and movement of the string causes the occurrence of voltage and then of a current in the string. The amplitude of the current undergoes change controlled by the amplifier with a time delay. Figure 1.28b shows the schematic of the electric system. The output and input voltages are governed by a non-linear cubic-type relation.

The magnetic induction $B(x)$ acting along the string generates voltage at the ends of the string according to the following equation:

$$U_{\text{input}}(t) = \int_0^l B(x)\frac{\partial u(t,x)}{\partial t}\mathrm{d}x, \tag{1.110}$$

where x is the spatial coordinate, t denotes time, $u(t,x)$ is the string displacement in the point (t,x), and l is the length of the string. The amplifier gives the output voltage

$$\widetilde{U}_{\text{output}} = \widetilde{h}_1 U_{\text{input}}(t) - \widetilde{h}_2 U^3_{\text{input}}(t), \tag{1.111}$$

where $\widetilde{h}_i$ $(i = 1, 2)$ are constant coefficients.

The current oscillations, including a time delay τ in the amplifier, are governed by the equation

$$\ddot{I}(t) + 2\lambda\dot{I}(t) + kI(t) = \dot{U}_{\text{output}}(t-\tau), \tag{1.112}$$

where

$$2\lambda = RL^{-1}, \qquad k = (LC)^{-1}, \qquad h_1 = L^{-1}\widetilde{h}_1, \qquad h_2 = L^{-1}\widetilde{h}_2,$$

$$U_{\text{output}}(t) = h_1 U_{\text{input}}(t) - h_2 U^3_{\text{input}}(t),$$

and the dot denotes differentiation with respect to t and $I(t)$ denotes the changes of the current. The changes in time of $I(t)$ and the changes in x of $B(x)$ play the role of force acting on the string whose oscillations are governed by the equation

$$\frac{\partial^2 u(t,x)}{\partial t^2} - c^2\frac{\partial^2 u(t,x)}{\partial x^2} = -\frac{\varepsilon}{\rho}\left(2h_0\frac{\partial u(t,x)}{\partial t} - B(x)I(t)\right), \tag{1.113}$$

where h_0 is the external damping coefficient, ρ is the mass density along the unit length, and ε is the small positive parameter.

The frequencies of free oscillations of the string are given by $\omega_s = \pi cs/l$, and the homogeneous boundary conditions are as follows:

$$u(t,0) = u(t,l) = 0. \tag{1.114}$$

1.4.2 Averaging Method

Our consideration is limited to first-order averaging. For $\varepsilon = 0$ the solution to (1.113) can be approximated by

$$u_0 = a_1\cos(\omega_1 t + \theta_1)\sin\left(\frac{\pi x}{l}\right) + a_3\cos(3\omega_1 t + \theta_3)\sin\left(\frac{3\pi x}{l}\right), \tag{1.115}$$

where a_1, a_3 are the amplitudes, and θ_1, θ_3 the phases.

Only two modes are taken into account because the others are quickly damped during the string dynamics and their influence on the results can be neglected.

For a small enough $\varepsilon \neq 0$ the solution to (1.113) is expected to be of the form

$$u = u_0 + \varepsilon u_1(x, a_1, a_3, \theta_1, \theta_3) + O(\varepsilon^2). \tag{1.116}$$

Supposing that $B(x)$ is symmetric with respect to the ends of the string, i.e., $B(x) = B(l - x)$, we take

$$B = B_1 \sin(\pi x/l) + B_3 \sin(3\pi x/l). \tag{1.117}$$

This assumption clarifies the selection of modes in (1.115). From (1.110) we obtain

$$U_{\text{input}} = -\frac{1}{2} B_1 a_1 \omega_1 l \sin(\omega_1 t + \theta_1) - \frac{3}{2} B_3 a_3 \omega_1 l \sin(3\omega_1 t + \theta_3), \tag{1.118}$$

and the right-hand side of (1.112) is calculated using a symbolic calculation (in *Mathematica*)

$$\begin{aligned}
\dot{U}_{\text{output}}(t - \tau) = &-\frac{1}{2} B_1 a_1 h_1 l \omega_1^2 \cos\psi_{10} - \frac{9}{2} B_3 a_3 h_1 l \omega_1^2 \cos\psi_{30} \\
&+ \frac{3}{8} B_1^3 a_1^3 h_2 l^3 \omega_1^4 \cos\psi_{10} \sin^2\psi_{30} \\
&+ \frac{27}{8} B_1^2 B_3 a_1^2 a_3 h_2 l^3 \omega_1^4 \cos\psi_{30} \sin^2\psi_{10} \\
&+ \frac{9}{8} B_1^2 B_3 a_1^2 a_3 h_2 l^3 \omega_1^4 \sin 2\psi_{10} \sin\psi_{30} \\
&+ \frac{81}{8} B_1 B_3^2 a_1 a_3^2 h_2 l^3 \omega_1^4 \sin 2\psi_{30} \sin\psi_{10} \\
&+ \frac{27}{8} B_1 B_3^2 a_1 a_3^2 h_2 l^3 \omega_1^4 \cos\psi_{10} \sin^2\psi_{30} \\
&+ \frac{243}{8} B_3^3 a_3 h_2 l^3 \omega_1^4 \cos\psi_{30} \sin^2\psi_{30},
\end{aligned} \tag{1.119}$$

where

$$\psi_{10} = \omega t + \theta_1 - \mu t, \qquad \psi_{30} = 3\omega t + \theta_3 - 3\mu t, \qquad \mu = \frac{\tau\omega}{t}. \tag{1.120}$$

From (1.119) we take only the harmonics $\sin i\omega_1 t$, $\cos i\omega_1 t$ $(i = 1, 3)$, and therefore

$$\dot{U}_{\text{output}}(t - \tau) = b_{1c} \cos\omega_1 t + b_{1s} \sin\omega_1 t + b_{3c} \cos 3\omega_1 t + b_{3s} \sin 3\omega_1 t, \tag{1.121}$$

where

$$
\begin{aligned}
b_{1c} &= A\cos\theta_1^* - \frac{9}{32}B_1^2B_3a_1^2a_3h_2l^3\omega_1^4\cos(2\theta_1^* - \theta_3^*),\\
b_{1s} &= -A\sin\theta_1^* + \frac{45}{64}B_1^2B_3a_1^2a_3h_2l^3\omega_1^4\sin(2\theta_1^* - \theta_3^*),\\
b_{3c} &= C\cos\theta_3^* - \frac{3}{32}B_1^3B_3a_1^3a_3h_2l^3\omega_1^4\cos(3\theta_1^*),\\
b_{3s} &= -C\sin\theta_3^* + \frac{3}{32}B_1^3a_1^3h_2l^3\omega_1^4\sin(3\theta_1^*),\\
A &= -\frac{1}{2}B_1a_1h_1l\omega_1^2 + \frac{3}{12}B_1^3a_1^3h_2l^3\omega_1^4 + \frac{27}{16}B_1B_3^2a_1a_3^2h_2l^3\omega_1^4,\\
C &= -\frac{9}{2}B_3a_3h_1l\omega_1^2 + \frac{27}{16}B_1^2a_1^2a_3h_2l^3\omega_1^4 + \frac{243}{32}B_3^3a_3^3h_2l^3\omega_1^4,\\
\theta_1^* &= \theta_1 - \mu t, \qquad \theta_3^* = \theta_3 - 3\mu t.
\end{aligned}
\tag{1.122}
$$

A solution to the linear (1.112) has the form

$$
I_0(t) = \sum_{i=1,3}\{(b_{ic}M_i - b_{is}N_i)\cos \mathrm{i}\omega_1 t + (b_{ic}N_i - b_{is}M_i)\sin \mathrm{i}\omega_1 t\} + h.h.,
\tag{1.123}
$$

where M_i, N_i are given below:

$$
M_i = \frac{k - i^2\omega_1^2}{(k - i^2\omega_1^2)^2 + 4i^2\lambda^2\omega_1^2}, \qquad N_i = \frac{2\lambda \mathrm{i}\omega_1}{(k - i^2\omega_1^2)^2 + 4i^2\lambda^2\omega_1^2}
\tag{1.124}
$$

and the abbreviation $h.h.$ denotes higher harmonics that are not taken into account.

Further analysis is straightforward for the perturbation technique, and the details can be found elsewhere [9, 15]. Because $B(x)$ and $I(t)$ are defined, (1.113) can be solved using a classical perturbation approach. (It is assumed that $u_1(x, a_1, a_3, \theta_1, \theta_3)$ is a limited and periodic function).

Substituting (1.116) into (1.113) and taking into account that $a_i = a_i(t)$ and $\theta_i = \theta_i(t)$ $(i = 1, 3)$ are slowly changing in time, from the right-hand side of (1.113) (henceforth referred to as R) the following resonance terms are computed:

$$
\begin{aligned}
R_{ic} &= \frac{2}{\pi l}\int_0^l\int_0^{2\pi} R\sin\frac{\pi i x}{l}\cos\psi_{i0}\mathrm{d}\psi_{i0},\\
R_{is} &= \frac{2}{\pi l}\int_0^l\int_0^{2\pi} R\sin\frac{\pi i x}{l}\sin\psi_{i0}\mathrm{d}\psi_{i0},\\
\psi_{i0} &= \mathrm{i}\omega_1 + \theta_i, \qquad i = 1, 3,
\end{aligned}
\tag{1.125}
$$

where R_{ic}, R_{is} correspond to the terms by $\cos\psi_{i0}$ and $\sin\psi_{i0}$, respectively. The comparison of the terms by $\cos\psi_{i0}$ and $\sin\psi_{i0}$ and generated by the left-hand side of (1.113) to those defined by (1.125) leads to the following average-amplitude equations:

$$\begin{aligned}
\dot{a}_1 &= -\frac{\varepsilon h_0 a_1}{\rho} - \frac{\varepsilon B_1}{2\rho\omega_1}\{(b_{1c}M_1 - b_{1s}N_1)\sin\theta_1 \\
&\qquad +(b_{1c}N_1 + b_{1s}M_1)\cos\theta_1\}, \\
\dot{a}_3 &= -\frac{\varepsilon h_0 a_3}{\rho} - \frac{\varepsilon B_3}{6\rho\omega_1}\{(b_{3c}M_3 - b_{3s}N_3)\sin\theta_3 \\
&\qquad +(b_{3c}N_3 + b_{3s}M_3)\cos\theta_3\}, \\
\dot{\theta}_1 &= -\frac{\varepsilon B_1}{2a_1\rho\omega_1}\{(b_{1c}M_1 - b_{1s}N_1)\cos\theta_1 \\
&\qquad -(b_{1c}N_1 + b_{1s}M_1)\sin\theta_1\}, \\
\dot{\theta}_3 &= -\frac{\varepsilon B_3}{6a_3\rho\omega_1}\{(b_{3c}M_3 - b_{3s}N_3)\cos\theta_3 \\
&\qquad -(b_{3c}N_3 + b_{3s}M_3)\sin\theta_3\}.
\end{aligned} \tag{1.126}$$

The preceding equations are coupled via (1.122). The first attempt to derive an averaged set of equations was made by Rubanik [12]. However, neither qualitative nor quantitative analysis or predictions of the possible behavior of the solutions to the equations obtained have been given.

The analyzed set of equations has some properties that can cause difficulties during numerical analysis. First of all, this is a stiff set of equations [note the occurrence of a_i $(i = 1, 3)$ in the denominator of the last two equations of (1.126)]. As is assumed by the averaging procedure, amplitudes a_i and θ_i change in time very slowly, and a long integration to trace the behavior of the system is required.

For the further analysis of the time-dependent solutions we transform (1.126) into amplitude equations. For this purpose we assume

$$u_0 = (Y_1\cos\omega_1 t + Y_2\sin\omega_1 t)\sin\frac{\pi x}{l} + (Y_3\cos 3\omega_1 t + Y_4\sin 3\omega_1 t)\sin\frac{3\pi x}{l}. \tag{1.127}$$

The comparison with (1.115) yields the following relations:

$$\begin{aligned}
Y_1(t) &= a_1(t)\cos\theta_1(t), \qquad Y_2(t) = -a_1(t)\sin\theta_1(t), \\
Y_3(t) &= a_3(t)\cos\theta_3(t), \qquad Y_4(t) = -a_3(t)\sin\theta_3(t).
\end{aligned} \tag{1.128}$$

In what follows the set of amplitude differential equations has the form

$$\begin{aligned}
\dot{Y}_1(t) &= \dot{a}_1(t)\cos\theta_1(t) - a_1(t)\dot{\theta}_1(t)\sin\theta_1(t),\\
\dot{Y}_2(t) &= -\dot{a}_1(t)\sin\theta_1(t) - a_1(t)\dot{\theta}_1(t)\cos\theta_1(t),\\
\dot{Y}_3(t) &= a_3(t)\cos\theta_3(t) - a_3(t)\dot{\theta}_3(t)\sin\theta_3(t),\\
\dot{Y}_4(t) &= -\dot{a}_3(t)\sin\theta_3(t) - a_3(t)\dot{\theta}_3(t)\cos\theta_3(t),
\end{aligned} \tag{1.129}$$

where $\dot{a}_i$ and $\dot{\theta}_i$ are given by (1.126) and

$$\begin{aligned}
\theta_1 &= \arctan(-Y_2/Y_1), \qquad & \theta_3 &= \arctan(-Y_4/Y_3),\\
a_1 &= (Y_1^2 + Y_2^2)^{1/2}, \qquad & a_3 &= (Y_3^2 + Y_4^2)^{1/2}.
\end{aligned} \tag{1.130}$$

1.4.3 Numerical Analysis and Results

In a standard approach to non-linear dynamical system analysis, time-dependent solutions are first considered and examined. For this purpose we consider a non-linear set of algebraic equations obtained from (1.126), where the left-hand sides are equal to zero. To solve the problem, a Powell hybrid method and a variation of Newton's method were used. They require a finite-difference approximation to the Jacobian with high-precision arithmetic. The root was accepted if the relative error between two successive approximations was less than 0.0001.

In a general case it can happen that the system of equations under consideration has one isolated solution or has a family of coexisting solutions for a fixed set of parameters. The system always possesses the trivial solution $a_1 = a_3 = \theta_1 = \theta_3 = 0$, which corresponds to the equilibrium position of the original system. Non-trivial solutions correspond to the periodic oscillations of the string described by the assumed solution (1.116). The stability of periodic oscillations corresponds to the stability of fixed points, i.e., to the stability of roots of the non-linear algebraic equations. To define the stability of the time-independent solutions obtained from the algebraic non-linear set of equations, we perturb them and then substitute for (1.116). Taking into account only the first powers of perturbations we get from (1.116) a linear set of differential equations. Based on these equations, a matrix corresponding to the analyzed fixed point is defined. In our case, because of the complicated equations, that matrix is obtained numerically. The eigenvalues of the matrix obtained determine the stability and bifurcation of the analyzed solutions (see monographs [16, 17]).

We present below two examples of such a computation. The following parameters were treated as fixed: $l = 0.1$, $\omega = 4.1$, $\lambda = 0.01$, $k = 25$, $h_1 = 0.01$, $h_2 = 0.6$, $\varepsilon/\rho = 1$, $h_0 = 0$, $B_3 = 0.4$. The coefficient μ and the amplitude B_1 served as the control parameters. In Fig. 1.29 one can observe that for $\mu = 0.001$ with an increase in the first amplitude of the electromagnetic induction, the amplitude a_1

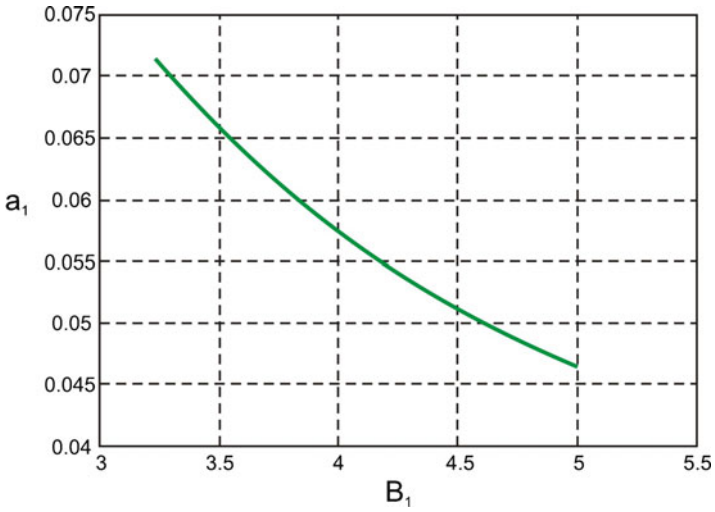

Fig. 1.29 First harmonic amplitude against B_1

decreases (the amplitude a_3 and the phases θ_1 and θ_3 remain almost constant). A similar situation is observed for $\mu = 0.01$ and $\mu = 0.1$. This means that for the considered set of fixed parameters, an increase in B_1 damps the magnitude of oscillations.

A question arises as to whether there is only one isolated solution that corresponds to the fixed value of B_1. We have found that in an interval $B_1 \in (3.0, 5.0)$ for each value of B_1 there exist two solutions for a_1 (marked with triangles) and one for a_3 (marked with crosses), as shown in Fig. 1.30. In both figures the obtained solutions are stable.

It is a difficult task to prove the existence of time-dependent solutions in the system of averaged (1.129). The most expected situation (confirmed by numerical computations) is to find stable fixed points that correspond to the oscillations with constant amplitudes in the original system. However, we have also found periodic orbits in the analyzed averaged differential equations. On the basis of this example, it is proper to describe the benefits obtained from the averaging technique applied. Instead of examining of a complicated system of non-linear partial and ordinary differential equations, we reduce the problem to the analysis of the four ordinary differential equations. Inserting the results obtained numerically into (1.127) we obtain an averaged solution corresponding to the original system.

We now briefly describe a numerical method for tracking down changes in periodic orbits, their stability, and potential bifurcations [16, 17]. For this purpose, let us consider an approximate position of the fixed point $Y_0^{(k)}$ close to the unknown exact one and perform numerical integration over the estimated period $T^{(k)}$. Actually, we have rescaled the equations according to the rule $\bar{t} = \Omega t$, where Ω serves as an unknown to be determined and the period is equal to 2π.

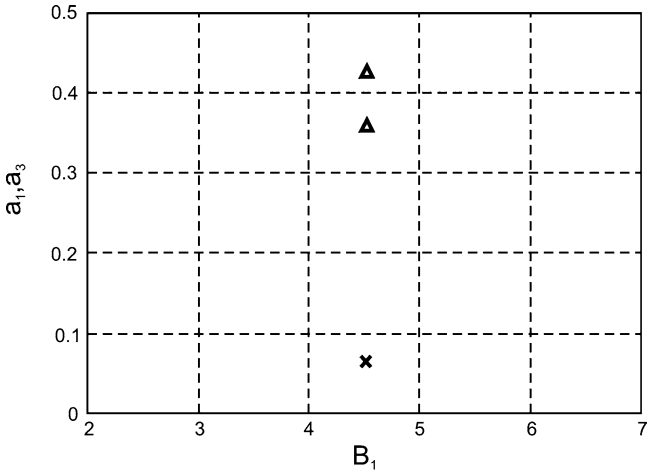

Fig. 1.30 Example of multiple set of solutions corresponding to $B_1 = 4.5$

The error $E = Y_0^{(k)} - G_0^{(k)}$ (where $G_0^{(k)} = G(Y_0^{(k)})$ is a point mapping) shows the accuracy of the calculations. Then, after a perturbation of the fixed point, its stability is determined based on the eigenvalues of a monodromy matrix. The results of calculation of the fixed points of the map (periodic orbits) as functions of B_1 for $l = 0.1$, $\mu = 0.1$, $\omega = 2.9$, $\lambda = 0.1$, $k = 9.0$, $h_1 = 0.05$, $h_2 = 0.01$, $\rho/\varepsilon = 1.0$, $h_0 = 0.02$, $B_3 = 0.8$ are presented in Fig. 1.31a, b. In this figure, Y_3 and Y_4 are much smaller than Y_1 and Y_2 and are assumed to be zero. Variation of the period following the change of B_1 is evident (Fig. 1.31b, where $Z = 1/\Omega$). The observed periodic orbit is "strongly" stable because the corresponding multipliers lie close to the origin. As an example, one of the periodic orbits is presented in Fig. 1.32a, b. One revolution of the variables $Y_{1,2}$ corresponds to two revolutions of $Y_{3,4}$ during the period 2π.

Special attention is focused on detecting the time-dependent aperiodic solutions to the averaged equations. Some interesting non-linear phenomena will be discussed subsequently and illustrated based on the gear simulation of the averaged equations.

Let us first consider the following fixed parameters: $l = 0.1$, $\mu = 0.15$, $\omega_1 = 190$, $\lambda = 0.1$, $k = 25.0$, $h_1 = 0.58$, $h_2 = 0.05544$, $\rho = 1.0$, $\varepsilon = 0.05$, $h_0 = 0.001$, $B_3 = 0.08$. Here the coefficient μ serves as a control parameter. Figure 1.33a illustrates the oscillations of $Y_{1,2}$ and the exponential decay of $Y_{3,4}$. The variables $Y_{1,3}$ and $Y_{2,4}$ correspond to the time evolution of the first two modes of the string arid their derivatives, respectively.

The amplitudes of the first mode oscillate, but those corresponding to the third mode decrease in time in a non-oscillatory (exponential) manner. The decrease in μ damps the oscillatory effects, which is shown in Fig. 1.33b for $\mu = 0.125$.

Figure 1.34 ($l = 0.1$, $\mu = 0.0$, $\omega_1 = 900.0$, $\lambda = 0.1515$, $k = 2750.0$, $h_1 = 5.48$, $h_2 = 70.0$, $\rho = 1.0$, $\varepsilon = 0.009$, $h_0 = 0.00001$, $B_1 = 0.65$, $B_3 = 0.89$)

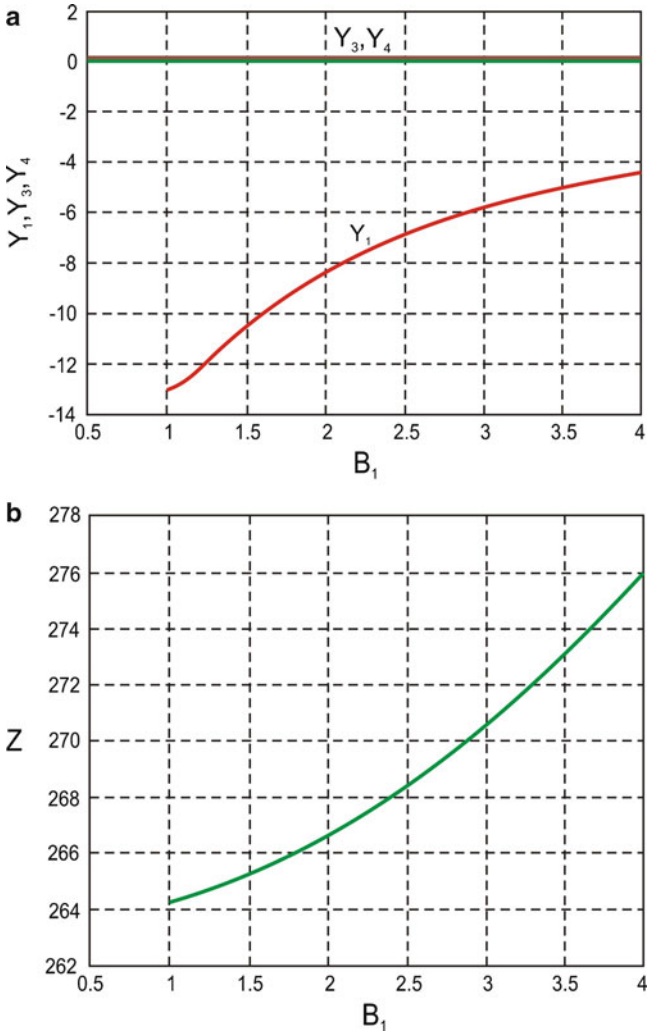

Fig. 1.31 Fixed points of Y_1, Y_3, Y_4 (**a**) and $Z = 1/\Omega$ (**b**) against control parameter B_1

illustrates an unexpected non-linear phenomenon. A long time-transitional process has been interrupted by the sudden occurrence of the strong nonlinear $Y_{1,2}$ oscillations.

In Fig. 1.35 the coexistence of the periodic oscillations $Y_{1,2}(t)$ with the exponential decay of $Y_{3,4}(t)$ is shown. The simulation was performed for the following fixed parameters: $l = 0.1$, $\mu = 0.1$, $\omega_1 = 0.1$, $\lambda = 0.1$, $k = 7250.0$, $h_1 = 0.1$, $h_2 = 0.1$, $\rho = 1.0$, $\varepsilon = 0.05$, $h_0 = 0.001$, $B_1 = 6.3$, $B_3 = 0.08$. Because $Y_{1,2}$ and $Y_{3,4}$ correspond to the first and third modes of the string, respectively, this result can be interpreted as the independent mode behavior.

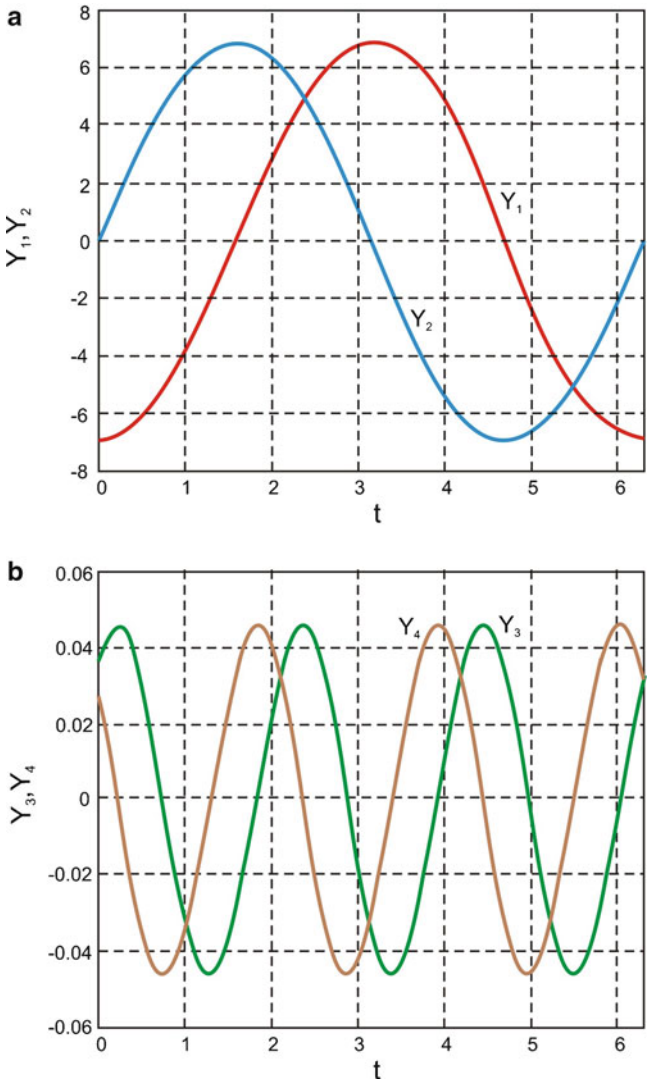

Fig. 1.32 Periodic orbits $Y_{1,2}$ (**a**) and $Y_{3,4}$ (**b**) with normalized 2π period

The result obtained also illustrates another interesting non-linear behavior. The solution to the averaged non-linear differential equations can be assumed analytically in a different form: an exponential decay function and an oscillatory function with a constant amplitude.

Figure 1.36 ($l = 0.1$, $\mu = 0.1$, $\omega_1 = 190.0$, $\lambda = 0.1$, $k = 25.0$, $h_1 = 0.58$, $h_2 = 0.05544$, $\rho = 1.0$, $\varepsilon = 0.005$, $h_0 = 0.00999$, $B_1 = 6.3$, $B_3 = 0.08$) presents a strange time evolution leading to instability. Here also $Y_{1,2}(t)$ increases

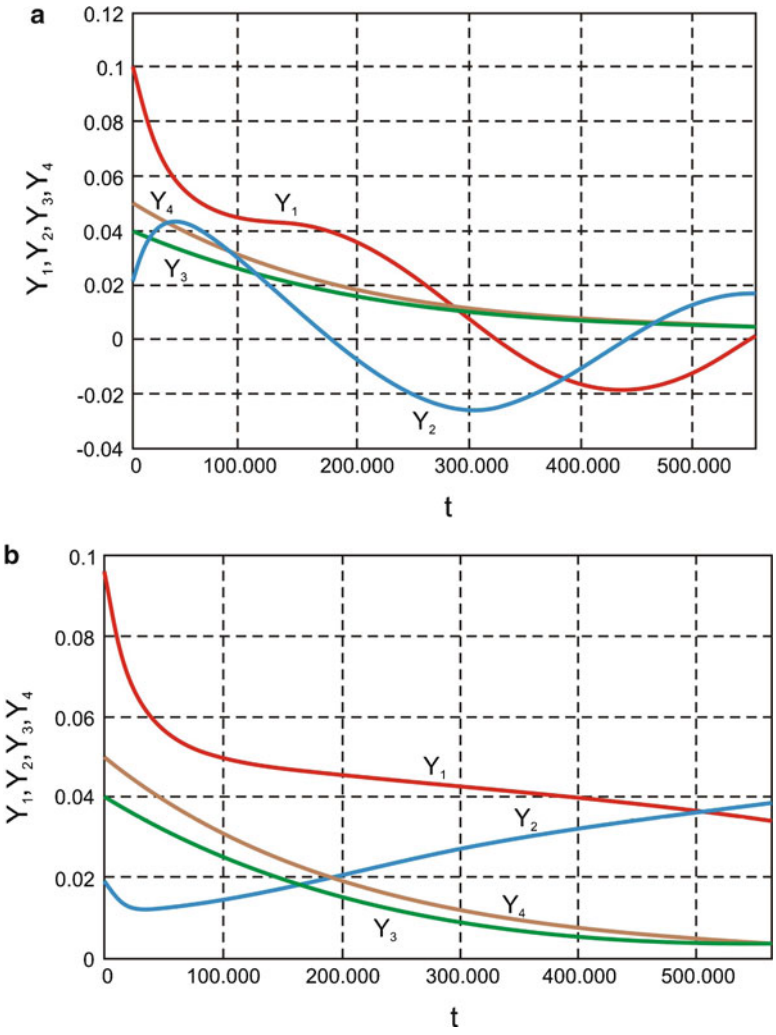

Fig. 1.33 Time evolutions of amplitudes: (**a**) $\mu = 0.15$, (**b**) $\mu = 0.125$

with oscillations, while $Y_{3,4}(t)$ slightly decreases almost linearly. After a long transitional state, barrierlike phenomena appear. Finally, strong nonlinear pressing effects, leading to the vertical unlimited increase in $Y_{1,2}(t)$, are observed.

This behavior can be explained as follows. An almost linear decrease in $Y_{3,4}(t)$ leading asymptotically to zero causes the occurrence of a sudden increase in $Y_{1,2}(t)$ due to the existence of a_3 in the denominator of the last equation of (1.126). However, typically the system does not exhibit such instability effects.

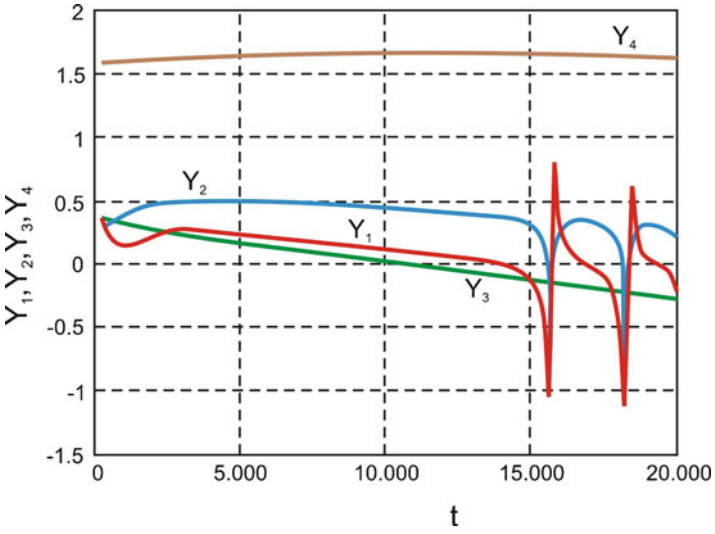

Fig. 1.34 Strong non-linear oscillations of amplitudes

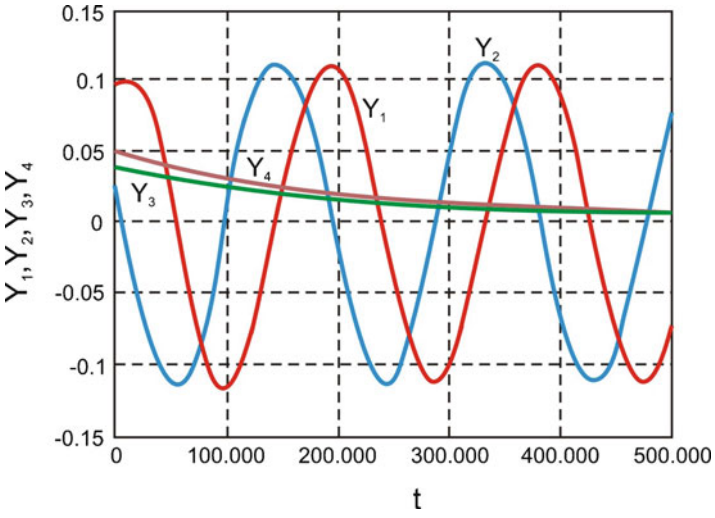

Fig. 1.35 Amplitude versus time

Finally, consider the following set of fixed parameters: $l = 0.1$, $\mu = 0.00001$, $\omega_1 = 900.0$, $\lambda = 0.1515$, $k = 7250.0$, $h_1 = 5.48$, $h_2 = 65.0$, $\rho = 1.0$, $\varepsilon = 0.009$, $h_0 = 0.00001$, $B_1 = 0.65$, $B_3 = 0.23$. A strong non-linear transitional oscillation of $Y_1(t)$ is shown in Fig. 1.37. The variables $Y_{3,4}(t)$ again change in a non-oscillatory manner quite independently in comparison with the first oscillation mode.

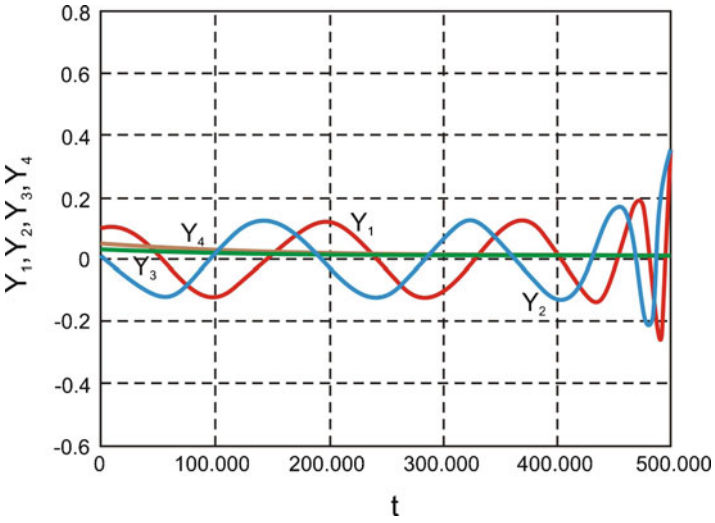

Fig. 1.36 Independent transitional time evolution of amplitudes leading to instability

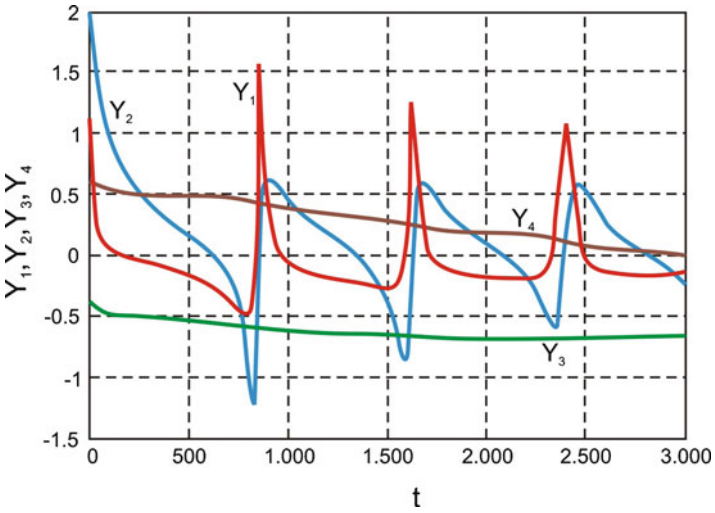

Fig. 1.37 Strong non-linear transitional oscillations

1.5 Rotor Supported by Magnetohydrodynamic Bearing

In general, rotating machinery elements are frequently encountered in mechanical/mechatronic engineering, and in numerous cases their non-linear dynamics causes many harmful effects, i.e., noise and vibrations. In particular, non-linear rotordynamics plays a crucial role in understanding various non-linear phenomena

and despite its long research history (see, e.g., [18–22] and references therein), it continues to attract the attention of many researchers and engineers. Since the topics related to non-linear rotordynamics are broad ranging and cover many interesting aspects related to both theory and practice, in this section we aim only at the analysis of some problems related to a rotor suspended in a magnetohydrodynamic field in the case of soft and rigid magnetic materials.

Magnetic, magnetohydrodynamic, and piezoelectric bearings are used in many mechanical engineering applications to support a high-speed rotor, provide vibration control, minimize rotating friction losses, and potentially avoid flutter instability. Many publications are dedicated to the dynamic analysis and control of a rotor supported on various bearing systems. The conditions for active closed-/open-loop control of a rigid rotor supported on hydrodynamic bearings and subjected to harmonic kinematical excitation are presented in [23, 24]. The methodology for modeling lubricated revolute joints in constrained rigid multibody systems is described in [25]. The hydrodynamic forces used in the dynamic analysis of journal bearings, including both squeeze and wedge effects, are evaluated from the system-state variables and included in the equations of motion of multibody systems. To analyze the dynamic behavior of a rub-impact rotor supported by turbulent journal bearings and lubricated with couple stress fluid under quadratic damping, the authors of reference [26] used system-state trajectory, Poincar maps, power spectrum, bifurcation diagrams, and Lyapunov exponents. Dynamic motion was detected to be periodic, quasiperiodic, and chaotic.

Rotor-active magnetic bearing (AMB) systems with time-varying stiffness are considered in [27]. Using the method of multiple scales, a governing non-linear equation of motion for the rotor-AMB system with one degree of freedom is transformed into an averaged equation, and then bifurcation theory and a bifurcation method of the detection function are used to analyze the bifurcations of multiple limit cycles of the averaged equation.

Rotors supported by floating ring bearings may exhibit instabilities due to self-excited vibrations [28]. The authors applied linear stability analysis to reveal a sign change of real parts of the conjugated eigenvalue pairs, and a center manifold reduction approach allowed them to explain the rotor destabilization via Hopf bifurcation. Owing to the analytical predictions that were applied, both sub- and supercritical bifurcations were found, and the analytical results were compared with numerical ones using a continuation method. Observe that rotors supported by a simple fluid film bearing the so-called oil whirl and oil whip dynamics ad been studied analytically in [18, 20–23]. Additionally, this problem was reconsidered recently with respect to inner and outer oil films and synchronization [29]. The full annular rub motion of a flexible rotor induced by mass unbalance and contact rub force with rigid and flexible stators, taking into account dry friction between the stator and rotor, is studied in [30]. Stability and synchronous problems of full annular rub motions are discussed, and a simplified formula for the dynamic stability of the system being investigated is derived.

Ishida et al. [31] investigate the vibrations of a flexible rotor system with radial clearance between an outer ring of the bearing and a casing using numerical and experimental studies. The following non-linear behavior was detected, illustrated, and discussed: (a) sub-, super-sub, and combined resonances; (b) self-excited vibrations of forward whirling mode; and (c) transitions from self-excited to forced system vibrations. In particular, the influence of static force and bearing damping was analyzed using the harmonic balance method.

Quinn [32] studied the non-linear output of a damped Jeffcott rotor with anisotropic stiffness and imbalance. It was shown that for sufficiently small external torque (or large imbalance), resonance capture may occur whereby the rotational shaft velocity cannot increase beyond the fundamental resonance between the rotational and translational motion providing a mechanism for energy transfer. Prediction of the system behavior on the basis of the reduced-order averaged model is verified and validated against numerical studies of the original ODE-governed model.

In this section, the two-degree-of-freedom non-linear dynamics of a rotor supported on a magnetohydrodynamic bearing system (MHDB) is analyzed in the cases of soft and rigid magnetic materials. In the case of soft magnetic materials, the analytical solutions were obtained using the method of multiple scales [9, 15]. Rigid magnetic materials possess hysteretic properties that are realized in the present work by means of the Bouc–Wen hysteretic model [33, 34]. This model enables simulation of hysteretic loops of various forms for systems from very different fields such as mechanics, biology, electronics, ferroelectricity, and magnetism [35]. In particular, in mechanical/civil and mechatronic engineering, hysteresis occurs as the natural inclination of materials to yield to restoring forces against motion and dissipate energy, and it often deals with the memory nature of inelastic material properties, where the restoring forces (torques) depend on the deformation process history. In general, the classic Bouc–Wen model is described by the first-order non-linear ODE governing the input (displacement rotations) and output (restoring force/torque) signals in a hysteretic way. Furthermore, a proper choice of the Bouc–Wen parameters allows one to control their behavior so that it is similar to that of real hysteresis looplike processes. Observe that despite the simplicity of the Bouc–Wen model, its behavior and possible application still attract many researchers, in particular regarding the following topics:

(a) Ways of tuning the Bouc–Wen control parameters to match application-oriented hysteretic material properties (identifications process).
(b) Numerical analysis of a given full mathematical model including its control.
(c) Rigorous mathematical background devoted to proofs of the convergence between the Bouc–Wen-like models and their real application-oriented counterpart dynamic objects.

An extensive list of references related to the Bouc–Wen model and beyond, together with results of the researches associated with the analysis, identification, and control of the Bouc–Wen-like models, are reported in the monograph by Ikhouave and Rodellar [36], where the following topics are illustrated and discussed:

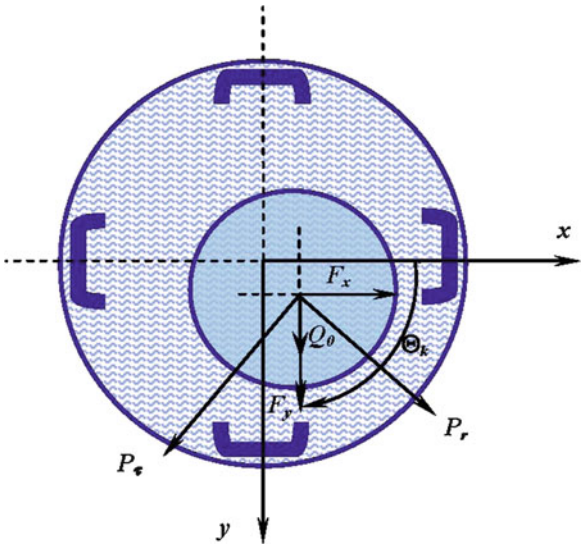

Fig. 1.38 Cross-section diagram of a rotor symmetrically supported on magnetohydrodynamic bearing

compatibility of the model versus physical laws, model parameters and hysteresis loops, identification and control of dynamic systems with Bouc–Wen models. Finally, various mathematical approaches to the hysteresis phenomenon are given in a survey reference [37].

As was demonstrated by investigations in [35], systems with hysteresis may reveal an unexpected behavior. On the one hand, hysteresis, like any dissipation, promotes the stabilization of motion and may restrain the occurrence of chaos. On the other hand, it may cause chaotic vibrations in a system. This last property is confirmed by the results of this section. In the absence of hysteresis, chaos is not observed. Taking into account hysteretic properties leads to chaotic vibrations of a rotor under certain conditions. The effect of hysteretic dissipation on the emergence of chaos is investigated using a methodology based on an analysis of wandering trajectories [33, 38]. Chaotic regions were obtained in parametric planes characterized by dynamic oil film action, magnetic control parameters, hysteretic dissipation, and the amplitude and frequency of external excitation.

1.5.1 Mathematical Model

Let us consider a uniform symmetric rigid rotor (Fig. 1.38) supported by a magnetohydrodynamic bearing system. The four-pole legs are symmetrically placed in the stator. F_k is the electromagnetic force produced by the kth opposed pair of electromagnet coils. This force is controlled by electric currents

$$i_k = i_0 \pm \Delta i_k \tag{1.131}$$

and can be expressed in the form

$$F_k = -\frac{2\mu_0 A N^2 i_0}{(2\delta + l/\mu^*)^2}\Delta i_k, \tag{1.132}$$

where i_0 denotes the bias current in the actuators' electric circuits, μ_0 is the magnetic permeability of vacuum, A is the core cross-section area, N is the number of windings of the electromagnet, δ is the air gap in the central position of the rotor with reference to the bearing sleeve, l is the total length of the magnetic path, the constant value $\mu^* = B_S/(\mu_0 H_S)$ denotes the magnetic permeability of the core material; the values of the magnetic induction B_S and magnetizing force H_S define the magnetic saturation level [23, 24]. θ_k is the angle between axis x and the kth magnetic actuator, Q_0 is the vertical rotor load identified with its weight, and (P_r, P_τ) are the radial and tangential components of the dynamic oil-film action, respectively. The equations of motion of the rotor are represented in the following form [23, 24, 39]:

$$\begin{aligned}
m^*\ddot{x}^* &= P_r^*\left(\rho, \dot{\rho}^*, \dot{\phi}^*\right)\cos\phi - P_\tau^*\left(\rho, \dot{\phi}^*\right)\sin\phi \\
&\quad + \sum_{k=1}^{K} F_k^* \cos\theta_k + Q_x^*(t), \\
m^*\ddot{y}^* &= P_r^*\left(\rho, \dot{\rho}^*, \dot{\phi}^*\right)\sin\phi + P_\tau^*\left(\rho, \dot{\phi}^*\right)\cos\phi \\
&\quad + \sum_{k=1}^{K} F_k^* \sin\theta_k + Q_0^* + Q_y^*(t), \\
P_r^*\left(\rho, \dot{\rho}^*, \dot{\phi}^*\right) &= -2C^*\left\{\frac{\rho^2\left(\omega^* - 2\dot{\phi}^*\right)}{p(\rho)\, q(\rho)} + \frac{\rho\dot{\rho}^*}{p(\rho)} + \frac{2\dot{\rho}^*}{\sqrt{p(\rho)}}\arctan\sqrt{\frac{1+\rho}{1-\rho}}\right\}, \\
P_\tau^*\left(\rho, \dot{\phi}^*\right) &= \pi C^* \frac{\rho\left(\omega^* - 2\dot{\phi}^*\right)}{q(\rho)\sqrt{p(\rho)}}.
\end{aligned} \tag{1.133}$$

Here m^* denotes the rigid rotor mass, (x^*, y^*) are the Cartesian coordinates of the rotor center, $Q_x^*(t)$, $Q_y^*(t)$ are the external excitation characterizing bearing movements. We consider the vibrations of the rotor excited by the harmonic movements of the bearing foundation in the vertical direction:

$$Q_x^*(t) = 0, \qquad Q_y^*(t) = Q^* \sin\Omega^* t^*, \tag{1.134}$$

where Q^* and Ω^* are the amplitude and frequency of the external excitation, respectively. The constant C^* is defined as

$$C^* = \frac{6\mu_s R_c L_c}{\delta_s^2}. \tag{1.135}$$

The parameters μ_s, δ_s, R_c, and L_c denote the oil viscosity, relative bearing clearance, journal radius, and total bearing length, respectively. (ρ, ϕ) are the polar coordinates, and $p(\rho) = 1 - \rho^2, q(\rho) = 2 + \rho^2$.

To represent the equations of motion in a dimensionless form, the following changes in variables and parameters are introduced:

$$\begin{aligned}
&t = \omega^* t^*, \quad \dot{\phi} = \frac{\dot{\phi}^*}{\omega^*}, \quad \dot{\rho} = \frac{\dot{\rho}^*}{\omega^*},\\
&x = \frac{x^*}{c^*}, \quad \dot{x} = \frac{\dot{x}^*}{\omega^* c^*}, \quad \ddot{x} = \frac{\ddot{x}^*}{\omega^{*2} c^*},\\
&y = \frac{y^*}{c^*}, \quad \dot{y} = \frac{\dot{y}^*}{\omega^* c^*}, \quad \ddot{y} = \frac{\ddot{y}^*}{\omega^{*2} c^*},\\
&C = \frac{C^*}{m^* \omega^* c^*}, \quad \Omega = \frac{\Omega^*}{\omega^*}, \quad Q = \frac{Q^*}{m^* \omega^{*2} c^*}, \quad Q_0 = \frac{Q_0^*}{m^* \omega^{*2} c^*},\\
&F_k = \frac{F_k^*}{m^* \omega^{*2} c^*}, \quad P_r = \frac{P_r^*}{m^* \omega^{*2} c^*}, \quad P_\tau = \frac{P_\tau^*}{m^* \omega^{*2} c^*},
\end{aligned} \tag{1.136}$$

where ω^* is the rotation speed of the rotor and c^* is the bearing clearance.

Thus the dimensionless equations of motion take the form

$$\begin{aligned}
\ddot{x} &= P_r\left(\rho, \dot{\rho}, \dot{\phi}\right) \cos\phi - P_\tau\left(\rho, \dot{\phi}\right) \sin\phi + F_x,\\
\ddot{y} &= P_r\left(\rho, \dot{\rho}, \dot{\phi}\right) \sin\phi + P_\tau\left(\rho, \dot{\phi}\right) \cos\phi + F_y + Q_0 + Q \sin\Omega t,\\
P_r\left(\rho, \dot{\rho}, \dot{\phi}\right) &= -2C \left\{ \frac{\rho^2\left(1 - 2\dot{\phi}\right)}{p\left(\rho\right) q\left(\rho\right)} + \frac{\rho\dot{\rho}}{p\left(\rho\right)} + \frac{2\dot{\rho}}{\sqrt{p\left(\rho\right)}} \arctan\sqrt{\frac{1+\rho}{1-\rho}} \right\},\\
P_\tau\left(\rho, \dot{\phi}\right) &= \pi C \frac{\rho\left(1 - 2\dot{\phi}\right)}{q\left(\rho\right)\sqrt{p\left(\rho\right)}}.
\end{aligned} \tag{1.137}$$

Here

$$\begin{aligned}
&x = \rho\cos\phi, \quad y = \rho\sin\phi,\\
&\dot{\phi} = \frac{\dot{y}x - \dot{x}y}{\rho^2}, \quad \dot{\rho} = \frac{x\dot{x} + y\dot{y}}{\rho}, \quad \rho = \sqrt{x^2 + y^2},\\
&\cos\phi = \frac{x}{\sqrt{x^2 + y^2}}, \quad \sin\phi = \frac{y}{\sqrt{x^2 + y^2}},
\end{aligned} \tag{1.138}$$

and the magnetic control forces are expressed as follows

$$F_x = -\gamma\dot{x} - \lambda\left(x - x_0\right), \qquad F_y = -\gamma\dot{y} - \lambda\left(y - y_0\right), \tag{1.139}$$

where (x_0, y_0) are the coordinates of the rotor static equilibrium and γ and λ are the control parameters.

1.5.2 Soft Magnetic Materials

In this section, we consider the two-degree-of-freedom dynamics of the rotor in the MHDB system without taking hysteresis into account.

1.5.2.1 Non-resonant case

The right-hand sides of (1.137) were expanded into Taylor series, and the origin was shifted to the location of the static equilibrium (x_0, y_0) for the convenience of investigation. The linear and quadratic terms were retained, so the reformed equations of motion are as follows:

$$\begin{aligned}\ddot{x} + \alpha x - \beta \dot{y} &= -2\hat{\mu}_1 \dot{x} + \alpha_1 x^2 + \alpha_2 y^2 + \alpha_3 x\dot{x} \\ &\quad + \alpha_4 xy + \alpha_5 x\dot{y} + \alpha_6 \dot{x} y + \alpha_7 y\dot{y}, \\ \ddot{y} + \alpha y + \beta \dot{x} &= -2\hat{\mu}_2 \dot{y} + \beta_1 x^2 + \beta_2 y^2 + \beta_3 x\dot{x} \\ &\quad + \beta_4 xy + \beta_5 x\dot{y} + \beta_6 \dot{x} y + \beta_7 y\dot{y} + F\cos(\Omega t + \tau)\,. \end{aligned} \tag{1.140}$$

We seek the first-order solution for small but finite amplitudes in the form

$$\begin{aligned} x &= \varepsilon x_1(T_0, T_1) + \varepsilon^2 x_2(T_0, T_1) + \cdots, \\ y &= \varepsilon y_1(T_0, T_1) + \varepsilon^2 y_2(T_0, T_1) + \cdots, \end{aligned} \tag{1.141}$$

where ε is the small, dimensionless parameter related to the amplitudes and $T_n = \varepsilon^n t$ $(n = 0, 1)$ are the independent variables; T_0 is the "fast" time, whereas T_1 is the "slow" time. It follows that the derivatives with respect to t become expansions in terms of the partial derivatives with respect to T_n according to

$$\begin{aligned} \frac{\mathrm{d}}{\mathrm{d}t} &= \frac{\partial}{\partial T_0}\frac{\partial T_0}{\partial t} + \frac{\partial}{\partial T_1}\frac{\partial T_1}{\partial t} + \frac{\partial}{\partial T_2}\frac{\partial T_2}{\partial t} + \cdots \\ &= D_0 + \varepsilon D_1 + \varepsilon^2 D_2 + \cdots, \\ \frac{\mathrm{d}^2}{\mathrm{d}t^2} &= \left(D_0 + \varepsilon D_1 + \varepsilon^2 D_2 + \ldots\right)^2 \\ &= D_0^2 + 2\varepsilon D_0 D_1 + \varepsilon^2\left(D_1^2 + 2D_0 D_2\right) + \cdots, \end{aligned} \tag{1.142}$$

where $D_k = \frac{\partial}{\partial T_k}$.

To analyze the *non-resonant case* the forcing term is ordered so that it appears at order ε. Thus, we recall in (1.140) $F = \varepsilon f$, $\hat{\mu}_n = \varepsilon \mu_n$. Substituting (1.141) into (1.140) and equating the coefficients of similar powers of ε we obtain

Order ε

$$\begin{aligned} D_0^2 x_1 + \alpha x_1 - \beta D_0 y_1 &= 0, \\ D_0^2 y_1 + \alpha y_1 + \beta D_0 x_1 &= f\cos\left(\Omega T_0 + \tau\right). \end{aligned} \tag{1.143}$$

Order ε^2

$$\begin{aligned} D_0^2 x_2 + \alpha x_2 - \beta D_0 y_2 = & -2D_0\left(D_1 x_1 + \mu_1 x_1\right) \\ & +\beta D_1 y_1 + \alpha_1 x_1^2 + \alpha_2 y_1^2 + \alpha_3 x_1 D_0 x_1 \\ & +\alpha_4 x_1 y_1 + \alpha_5 x_1 D_0 y_1 + \alpha_6 y_1 D_0 x_1 + \alpha_7 y_1 D_0 y_1, \\ D_0^2 y_2 + \alpha y_2 + \beta D_0 x_2 = & -2D_0\left(D_1 y_1 + \mu_2 y_1\right) \\ & -\beta D_1 x_1 + \beta_1 x_1^2 + \beta_2 y_1^2 + \beta_3 x_1 D_0 x_1 \\ & +\beta_4 x_1 y_1 + \beta_5 x_1 D_0 y_1 + \beta_6 y_1 D_0 x_1 + \beta_7 y_1 D_0 y_1. \end{aligned} \tag{1.144}$$

The solution of (1.143) is expressed in the form

$$\begin{aligned} x_1 = & A_1\left(T_1\right)\exp\left(\mathrm{i}\omega_1 T_0\right) + A_2\left(T_1\right)\exp\left(\mathrm{i}\omega_2 T_0\right) \\ & +\Phi_1 \exp\left[\mathrm{i}\left(\Omega T_0 + \tau\right)\right] + CC, \\ y_1 = & \Lambda_1 A_1\left(T_1\right)\exp\left(\mathrm{i}\omega_1 T_0\right) + \Lambda_2 A_2\left(T_1\right)\exp\left(\mathrm{i}\omega_2 T_0\right) \\ & +\Phi_2 \exp\left[\mathrm{i}\left(\Omega T_0 + \tau\right)\right] + CC, \end{aligned} \tag{1.145}$$

where CC denotes the complex conjugate of the preceding terms, A_1 and A_2 are the arbitrary functions of T_1 at this level of approximation,

$$\begin{aligned} \Lambda_n &= \frac{\omega_n^2 - \alpha}{\omega_n \beta} i, \qquad \Phi_1 = \frac{i}{2}\frac{\beta\Omega f}{\left(\alpha - \Omega^2\right)^2 - \beta^2\Omega^2}, \\ \Phi_2 &= \frac{1}{2}\frac{f\left(\alpha - \Omega^2\right)}{\left(\alpha - \Omega^2\right)^2 - \beta^2\Omega^2}, \qquad (n = 1,\ 2), \end{aligned} \tag{1.146}$$

ω_n are assumed to be distinct, and ω_n^2 are the roots of the characteristic equation

$$\begin{aligned} \det\begin{pmatrix} -\lambda & 1 & 0 & 0 \\ -\alpha & -\lambda & 0 & \beta \\ 0 & 0 & -\lambda & 1 \\ 0 & -\beta & -\alpha & -\lambda \end{pmatrix} &= \lambda^4 + \left(2\alpha + \beta^2\right)\lambda^2 + \alpha^2 \\ &= \omega_n^4 - \left(2\alpha + \beta^2\right)\omega_n^2 + \alpha^2 = 0, \\ \lambda_{1,2} &= \pm\mathrm{i}\omega_1, \qquad \lambda_{3,4} = \pm\mathrm{i}\omega_2, \end{aligned}$$

$$\lambda_{1,2} = \pm\frac{1}{2}\sqrt{-4\alpha - 2\beta^2 + 2\beta\sqrt{\beta^2 + 4\alpha}},$$
$$\lambda_{3,4} = \pm\frac{1}{2}\sqrt{-4\alpha - 2\beta^2 - 2\beta\sqrt{\beta^2 + 4\alpha}}. \quad (1.147)$$

Substitution of (1.145) into (1.144) gives

$$\begin{aligned} D_0^2 x_2 + \alpha x_2 - \beta D_0 y_2 &= \left[-2\mathrm{i}\omega_1\left(A_1' + \mu_1 A_1\right) + \beta\Lambda_1 A_1'\right]\exp(\mathrm{i}\omega_1 T_0) \\ &+ \left[-2\mathrm{i}\omega_2\left(A_2' + \mu_1 A_2\right) + \beta\Lambda_2 A_2'\right]\exp(\mathrm{i}\omega_2 T_0) + \cdots + CC, \\ D_0^2 y_2 + \alpha y_2 + \beta D_0 x_2 &= \left[-2\mathrm{i}\omega_1\Lambda_1\left(A_1' + \mu_2 A_1\right) - \beta A_1'\right]\exp(\mathrm{i}\omega_1 T_0) \\ &+ \left[-2\mathrm{i}\omega_2\Lambda_2\left(A_2' + \mu_2 A_2\right) - \beta A_2'\right]\exp(\mathrm{i}\omega_2 T_0) + \cdots + CC. \end{aligned} \quad (1.148)$$

Terms that do not influence the solvability conditions are not presented in the last equations and were replaced by dots. To determine the solvability conditions of (1.144), following the method of undetermined coefficients we seek a particular solution in the form

$$\begin{aligned} x_2 &= P_{11}\exp(\mathrm{i}\omega_1 T_0) + P_{12}\exp(\mathrm{i}\omega_2 T_0), \\ y_2 &= P_{21}\exp(\mathrm{i}\omega_1 T_0) + P_{22}\exp(\mathrm{i}\omega_2 T_0), \end{aligned} \quad (1.149)$$

with unknowns P_{11}, P_{12}, P_{21}, and P_{22}. Substitution of expressions (1.149) into (1.148) and collecting the coefficients at $\exp(\mathrm{i}\omega_1 T_0)$ and $\exp(\mathrm{i}\omega_2 T_0)$ yield

$$\begin{aligned} \left(\alpha - \omega_n^2\right) P_{1n} - i\beta\omega_n P_{2n} &= R_{1n}, \\ i\beta\omega_n P_{1n} + \left(\alpha - \omega_n^2\right) P_{2n} &= R_{2n}, \quad n = 1, 2, \end{aligned} \quad (1.150)$$

where

$$\begin{aligned} R_{11} &= -2\mathrm{i}\omega_1\left(A_1' + \mu_1 A_1\right) + \beta\Lambda_1 A_1', \\ R_{12} &= -2\mathrm{i}\omega_2\left(A_2' + \mu_1 A_2\right) + \beta\Lambda_2 A_2', \\ R_{21} &= -2\mathrm{i}\omega_1\Lambda_1\left(A_1' + \mu_2 A_1\right) - \beta A_1', \\ R_{22} &= -2\mathrm{i}\omega_2\Lambda_2\left(A_2' + \mu_2 A_2\right) - \beta A_2'. \end{aligned} \quad (1.151)$$

Taking into account the characteristic (1.147), the determinant Δ of the set of linear algebraic equations relative to P_{1n}, P_{2n} [(1.150)] is equal to zero:

$$\Delta = \begin{vmatrix} \alpha - \omega_n^2 & -\mathrm{i}\beta\omega_n \\ \mathrm{i}\beta\omega_n & \alpha - \omega_n^2 \end{vmatrix} = \left(\alpha - \omega_n^2\right)^2 - \beta^2\omega_n^2 = 0. \quad (1.152)$$

According to the Kronecker–Kapelly theorem, the set of linear algebraic equations is compatible if and only if the matrix rank of the linear set is equal to the extended matrix rank. Therefore, the solvability conditions are

$$\begin{vmatrix} R_{1n} & -\mathrm{i}\beta\omega_n \\ R_{2n} & \left(\alpha - \omega_n^2\right) \end{vmatrix} = 0, \qquad n = 1, 2; \tag{1.153}$$

otherwise the set of linear algebraic (1.150) has no solutions. So

$$R_{1n} = \frac{\mathrm{i}\beta\omega_n R_{2n}}{\omega_n^2 - \alpha} \tag{1.154}$$

and the solvability conditions can be written in the form

$$R_{1n} = \frac{R_{2n}}{\bar{\Lambda}_n}, \quad n = 1, 2. \tag{1.155}$$

The differential equations to define $A_1(T_1)$ and $A_2(T_1)$ are the consequence of solvability conditions (1.155)

$$\begin{aligned} &\left(\beta\Lambda_1 - 2\mathrm{i}\omega_1 + \frac{2\mathrm{i}\omega_1\Lambda_1 + \beta}{\bar{\Lambda}_1}\right)A_1' + \left(\frac{2\mathrm{i}\omega_1\Lambda_1\mu_2}{\bar{\Lambda}_1} - 2\mathrm{i}\omega_1\mu_1\right)A_1 = 0, \\ &\left(\beta\Lambda_2 - 2\mathrm{i}\omega_2 + \frac{2\mathrm{i}\omega_2\Lambda_2 + \beta}{\bar{\Lambda}_2}\right)A_2' + \left(\frac{2\mathrm{i}\omega_2\Lambda_2\mu_2}{\bar{\Lambda}_2} - 2\mathrm{i}\omega_2\mu_1\right)A_2 = 0. \end{aligned} \tag{1.156}$$

It follows from (1.141), (1.145), and (1.156) that the complex solution of the differential set (1.140) is

$$\begin{aligned} x &= \varepsilon[\exp(-\varepsilon\nu_1 t)\, a_1 \exp(\mathrm{i}\omega_1 t) + \exp(-\varepsilon\nu_2 t)\, a_2 \exp(\mathrm{i}\omega_2 t) \\ &\quad + \Phi_1 \exp[\mathrm{i}(\Omega t + \tau)] + CC] + O\left(\varepsilon^2\right), \\ y &= \varepsilon[\Lambda_1 \exp(-\varepsilon\nu_1 t)\, a_1 \exp(\mathrm{i}\omega_1 t) + \Lambda_2 \exp(-\varepsilon\nu_2 t)\, a_2 \exp(\mathrm{i}\omega_2 t) \\ &\quad + \Phi_2 \exp[\mathrm{i}(\Omega t + \tau)] + CC] + O\left(\varepsilon^2\right). \end{aligned} \tag{1.157}$$

Then the real solution is as follows:

$$\begin{aligned} x &= \varepsilon[\exp(-\varepsilon\nu_1 t)\, a_1 \cos(\omega_1 t + \Theta_1) + \exp(-\varepsilon\nu_2 t)\, a_2 \cos(\omega_2 t + \Theta_2) \\ &\quad + 2\mathrm{Im}\Phi_1 \sin(\Omega t + \tau)] + O\left(\varepsilon^2\right), \\ y &= \varepsilon[\mathrm{Im}\Lambda_1 \exp(-\varepsilon\nu_1 t)\, a_1 \sin(\omega_1 t + \Theta_1) + \mathrm{Im}\Lambda_2 \exp(-\varepsilon\nu_2 t)\, a_2 \sin(\omega_2 t + \Theta_2) \\ &\quad + 2\Phi_2 \cos(\Omega t + \tau)] + O\left(\varepsilon^2\right), \end{aligned} \tag{1.158}$$

where

$$\nu_n = \frac{2\omega_n(\mu_1+\mu_2)}{4\omega_n - \beta\left(\mathrm{Im}\Lambda_n + \frac{1}{\mathrm{Im}\Lambda_n}\right)}, \tag{1.159}$$

and a_n and Θ_n are the real constants.

Figures 1.39–1.41 show a comparison of the numerical integration of (1.140) and the perturbation solutions (1.158) for the following parameters of set (1.140): $\alpha = 1,500$, $\beta = 70$, $\alpha_1 = 9.985\times10^2$, $\alpha_2 = 2\times10^3$, $\alpha_3 = 7.9588\times10^3$, $\alpha_4 = 0.002$, $\alpha_5 = -4.0794\times10^3$, $\alpha_6 = 4.0002\times10^3$, $\alpha_7 = 8.0005\times10^3$, $\beta_1 = 29.9975$, $\beta_2 = -0.001$, $\beta_3 = -4.1594\times10^3$, $\beta_4 = -1.9997\times10^3$, $\beta_5 = -7.9188\times10^3$, $\beta_6 = 0.7959$, $\beta_7 = -0.4083$; the initial conditions are $x(0) = 10^{-12}$, $y(0) = 10^{-10}$, $\dot{x}(0) = \dot{y}(0) = 0$.

In the case of non-resonant undamped vibrations of a rotor (Fig. 1.39), it is accepted for numerical integration that $\hat{\mu}_1 = 0$, $\hat{\mu}_2 = 0$, $F = 0$. According to (1.158), the perturbation solution is presented by the expressions

$$\begin{aligned} x &= 8.2686044\cdot10^{-6}\cos(17.2015t) + 1.6313956\cdot10^{-6}\cos(87.2015t),\\ y &= 8.2686044\cdot10^{-6}\sin(17.2015t) - 1.6313956\cdot10^{-6}\sin(87.2015t). \end{aligned} \tag{1.160}$$

Figure 1.40 corresponds to the non-resonant damped vibrations of a rotor. For this case, $\hat{\mu}_1 = 0.1$, $\hat{\mu}_2 = 0.15$, $F = 0$. The perturbation solution has the form

$$\begin{aligned} x &= 8.2686044\cdot10^{-6}\exp(-0.0412t)\cos(17.2015t)\\ &\quad +1.6313956\cdot10^{-6}\exp(-0.2088t)\cos(87.2015t),\\ y &= 8.2686044\cdot10^{-6}\exp(-0.0412t)\sin(17.2015t)\\ &\quad -1.6313956\cdot10^{-6}\exp(-0.2088t)\sin(87.2015t). \end{aligned} \tag{1.161}$$

For the non-resonant forced damped vibrations of a rotor (Fig. 1.41) it is accepted for numerical integration that $\hat{\mu}_1 = 0.1$, $\hat{\mu}_2 = 0.15$, $F = 0.005$, $\Omega = 10$, $\tau = -\pi/2$. The perturbation solution is

$$\begin{aligned} x &= 5.8241\cdot10^{-6}\exp(-0.0412t)\cos(17.2015t)\\ &\quad +1.69495\cdot10^{-6}\exp(-0.2088t)\cos(87.2015t)\\ &\quad -2.38095\cdot10^{-6}\sin(10t-\pi/2),\\ y &= 5.8241\cdot10^{-6}\exp(-0.0412t)\sin(17.2015t)\\ &\quad -1.69495\cdot10^{-6}\exp(-0.2088t)\sin(87.2015t)\\ &\quad +4.7619\cdot10^{-6}\cos(10t-\pi/2). \end{aligned} \tag{1.162}$$

Figures 1.39–1.41 demonstrate good agreement of the numerical and analytical solutions.

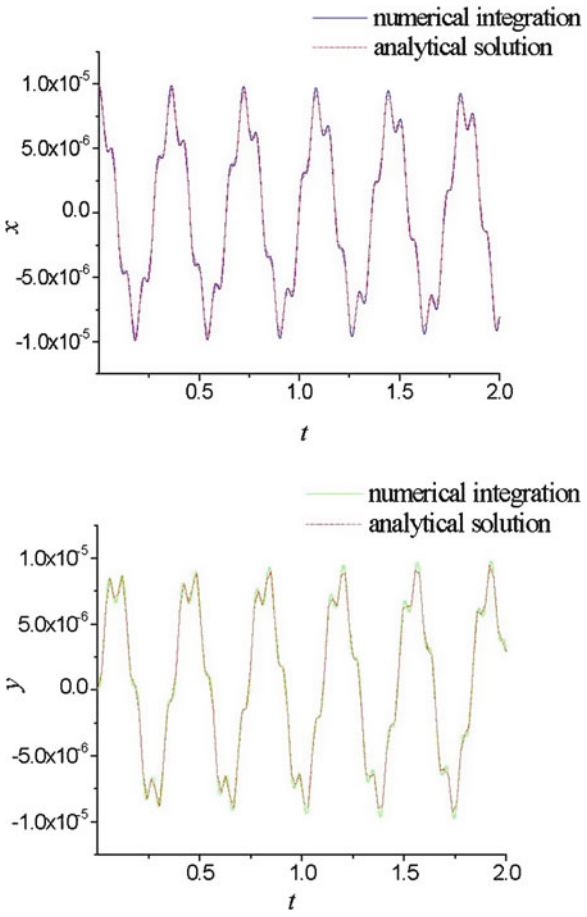

Fig. 1.39 Comparison of numerical integration (1.140) and perturbation solutions (1.158) in the case of non-resonant undamped vibrations of a rotor

1.5.2.2 Primary Resonance: The Cases of no Internal Resonance and an Internal Resonance

To analyze primary resonances, the forcing term is ordered such that it appears at order ε^2 or in the same perturbation equation as the non-linear terms and damping. Thus, we recall in (1.140) $F = \varepsilon^2 f$, $\hat{\mu}_n = \varepsilon \mu_n$. Consider the case where $\Omega \approx \omega_2$. The case $\Omega \approx \omega_1$ is analogous. Let us introduce the detuning parameter σ_1 and set $\Omega = \omega_2 + \varepsilon \sigma_1$.

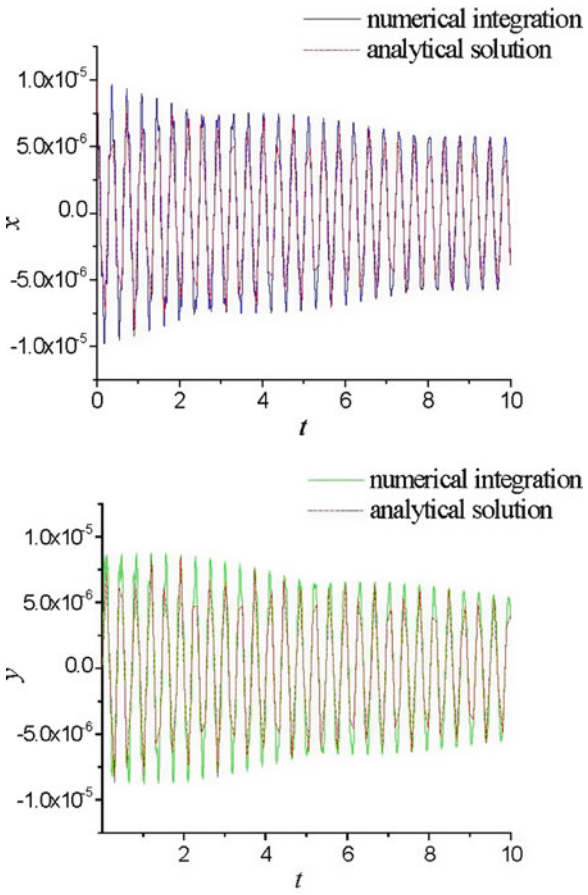

Fig. 1.40 Comparison of numerical integration (1.140) and perturbation solutions (1.158) in the case of non-resonant damped vibrations of a rotor

Substituting (1.141) into (1.140) and equating coefficients of similar powers of ε we obtain

Order ε

$$\begin{aligned} D_0^2 x_1 + \alpha x_1 - \beta D_0 y_1 &= 0, \\ D_0^2 y_1 + \alpha y_1 + \beta D_0 x_1 &= 0. \end{aligned} \tag{1.163}$$

Order ε^2

$$\begin{aligned} D_0^2 x_2 + \alpha x_2 - \beta D_0 y_2 = &-2D_0 (D_1 x_1 + \mu_1 x_1) + \beta D_1 y_1 \\ &+\alpha_1 x_1^2 + \alpha_2 y_1^2 + \alpha_3 x_1 D_0 x_1 + \alpha_4 x_1 y_1 \\ &+\alpha_5 x_1 D_0 y_1 + \alpha_6 y_1 D_0 x_1 + \alpha_7 y_1 D_0 y_1, \end{aligned}$$

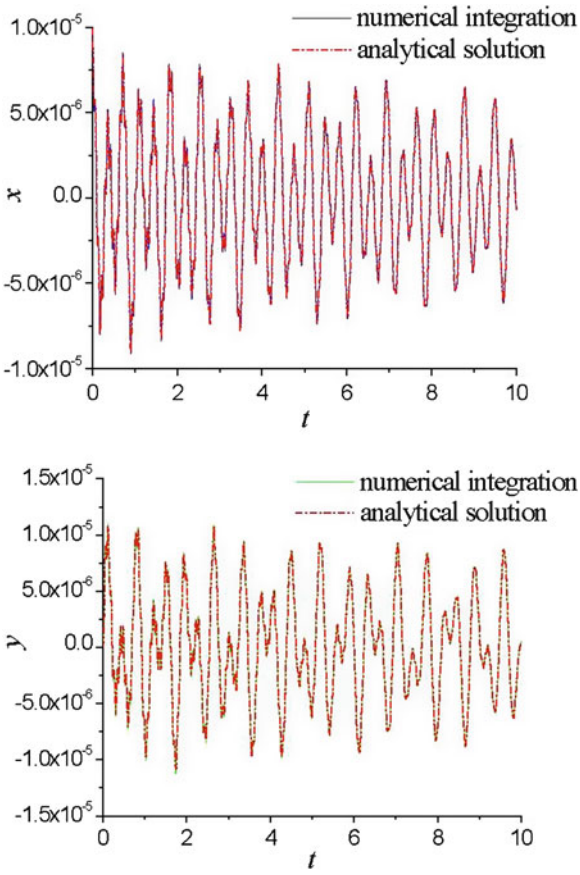

Fig. 1.41 Comparison of numerical integration (1.140) and perturbation solutions (1.158) in the case of non-resonant forced damped vibrations of a rotor

$$\begin{aligned} D_0^2 y_2 + \alpha y_2 + \beta D_0 x_2 = & -2D_0 \left(D_1 y_1 + \mu_2 y_1\right) - \beta D_1 x_1 \\ & + \beta_1 x_1^2 + \beta_2 y_1^2 + \beta_3 x_1 D_0 x_1 + \beta_4 x_1 y_1 \\ & + \beta_5 x_1 D_0 y_1 + \beta_6 y_1 D_0 x_1 + \beta_7 y_1 D_0 y_1 \\ & + f \cos\left(\Omega T_0 + \tau\right). \end{aligned} \tag{1.164}$$

The solution of (1.163) is given in the form

$$\begin{aligned} x_1 &= A_1\left(T_1\right) \exp\left(\mathrm{i}\omega_1 T_0\right) + A_2\left(T_1\right) \exp\left(\mathrm{i}\omega_2 T_0\right) + CC, \\ y_1 &= \Lambda_1 A_1\left(T_1\right) \exp\left(\mathrm{i}\omega_1 T_0\right) + \Lambda_2 A_2\left(T_1\right) \exp\left(\mathrm{i}\omega_2 T_0\right) + CC, \end{aligned} \tag{1.165}$$

where

$$\Lambda_n = \frac{\omega_n^2 - \alpha}{\omega_n \beta} i. \tag{1.166}$$

Substitution of (1.165) into (1.164) yields

$$
\begin{aligned}
D_0^2 x_2 + \alpha x_2 - \beta D_0 y_2 = & \left[-2\mathrm{i}\omega_1 \left(A_1' + \mu_1 A_1\right)\right. \\
& \left. + \beta \Lambda_1 A_1'\right] \exp\left(\mathrm{i}\omega_1 T_0\right) + \left[-2\mathrm{i}\omega_2 \left(A_2' + \mu_1 A_2\right)\right. \\
& \left. + \beta \Lambda_2 A_2'\right] \exp\left(\mathrm{i}\omega_2 T_0\right) + A_1^2[\alpha_1 + \Lambda_1^2 \alpha_2 + \mathrm{i}\omega_1 \alpha_3 + \Lambda_1 \alpha_4 \\
& + \mathrm{i}\omega_1 \Lambda_1 \alpha_5 + \mathrm{i}\omega_1 \Lambda_1 \alpha_6 + \mathrm{i}\omega_1 \Lambda_1^2 \alpha_7] \exp\left(2\mathrm{i}\omega_1 T_0\right) \\
& + A_2^2[\alpha_1 + \Lambda_2^2 \alpha_2 + \mathrm{i}\omega_2 \alpha_3 + \Lambda_2 \alpha_4 + \mathrm{i}\omega_2 \Lambda_2 \alpha_5 + \mathrm{i}\omega_2 \Lambda_2 \alpha_6 \\
& + \mathrm{i}\omega_2 \Lambda_2^2 \alpha_7] \exp\left(2\mathrm{i}\omega_2 T_0\right) + A_1 A_2[2\alpha_1 + 2\Lambda_1 \Lambda_2 \alpha_2 + (\mathrm{i}\omega_1 + \mathrm{i}\omega_2)\, \alpha_3 \\
& + (\Lambda_1 + \Lambda_2)\, \alpha_4 + (\mathrm{i}\omega_2 \Lambda_2 - \mathrm{i}\omega_1 \Lambda_1)\, \alpha_5 + (\mathrm{i}\omega_2 \Lambda_1 + \mathrm{i}\omega_1 \Lambda_2)\, \alpha_6 \\
& + (\mathrm{i}\omega_1 + \mathrm{i}\omega_2)\, \Lambda_1 \Lambda_2 \alpha_7] \exp\left(\mathrm{i}\left(\omega_1 + \omega_2\right) T_0\right) + \bar{A}_1 A_2[2\alpha_1 + 2\bar{\Lambda}_1 \Lambda_2 \alpha_2 \\
& + (\mathrm{i}\omega_2 - \mathrm{i}\omega_1)\, \alpha_3 + \left(\Lambda_2 + \bar{\Lambda}_1\right) \alpha_4 + \left(\mathrm{i}\omega_2 \Lambda_2 - \mathrm{i}\omega_1 \bar{\Lambda}_1\right) \alpha_5 \\
& + \left(\mathrm{i}\omega_2 \bar{\Lambda}_1 - \mathrm{i}\omega_1 \Lambda_2\right) \alpha_6 + (\mathrm{i}\omega_2 - \mathrm{i}\omega_1)\, \bar{\Lambda}_1 \Lambda_2 \alpha_7] \exp\left(\mathrm{i}\left(\omega_2 - \omega_1\right) T_0\right) \\
& + A_1 \bar{A}_1 \left(\alpha_1 + \Lambda_1 \left(\bar{\Lambda}_1 \alpha_2 + \alpha_4 + \mathrm{i}\omega_1 \left(\alpha_5 - \alpha_6\right)\right)\right) \\
& + A_2 \bar{A}_2 \left(\alpha_1 + \Lambda_2 \left(\bar{\Lambda}_2 \alpha_2 + \alpha_4 + \mathrm{i}\omega_2 \left(\alpha_5 - \alpha_6\right)\right)\right) + CC, \qquad (1.167)
\end{aligned}
$$

$$
\begin{aligned}
D_0^2 y_2 + \alpha y_2 + \beta D_0 x_2 = & \left[-2\mathrm{i}\omega_1 \Lambda_1 \left(A_1' + \mu_2 A_1\right) - \beta A_1'\right] \exp\left(\mathrm{i}\omega_1 T_0\right) \\
& + \left[-2\mathrm{i}\omega_2 \Lambda_2 \left(A_2' + \mu_2 A_2\right) - \beta A_2'\right] \exp\left(\mathrm{i}\omega_2 T_0\right) \\
& + A_1^2[\beta_1 + \Lambda_1^2 \beta_2 + \mathrm{i}\omega_1 \beta_3 + \Lambda_1 \beta_4 + \mathrm{i}\omega_1 \Lambda_1 \beta_5 + \mathrm{i}\omega_1 \Lambda_1 \beta_6 \\
& + \mathrm{i}\omega_1 \Lambda_1^2 \beta_7] \exp\left(2\mathrm{i}\omega_1 T_0\right) + A_2^2[\beta_1 + \Lambda_2^2 \beta_2 + \mathrm{i}\omega_2 \beta_3 + \Lambda_2 \beta_4 + \mathrm{i}\omega_2 \Lambda_2 \beta_5 \\
& + \mathrm{i}\omega_2 \Lambda_2 \beta_6 + \mathrm{i}\omega_2 \Lambda_2^2 \beta_7] \exp\left(2\mathrm{i}\omega_2 T_0\right) + A_1 A_2[2\beta_1 + 2\Lambda_1 \Lambda_2 \beta_2 \\
& + (\mathrm{i}\omega_1 + \mathrm{i}\omega_2)\, \beta_3 + (\Lambda_1 + \Lambda_2)\, \beta_4 + (\mathrm{i}\omega_2 \Lambda_2 - \mathrm{i}\omega_1 \Lambda_1)\, \beta_5 \\
& + (\mathrm{i}\omega_2 \Lambda_1 + \mathrm{i}\omega_1 \Lambda_2)\, \beta_6 + (\mathrm{i}\omega_1 + \mathrm{i}\omega_2)\, \Lambda_1 \Lambda_2 \beta_7] \exp\left(\mathrm{i}\left(\omega_1 + \omega_2\right) T_0\right) \\
& + \bar{A}_1 A_2[2\beta_1 + 2\bar{\Lambda}_1 \Lambda_2 \beta_2 + (\mathrm{i}\omega_2 - \mathrm{i}\omega_1)\, \beta_3 \\
& + \left(\Lambda_2 + \bar{\Lambda}_1\right) \beta_4 + \left(\mathrm{i}\omega_2 \Lambda_2 - \mathrm{i}\omega_1 \bar{\Lambda}_1\right) \beta_5 \\
& + \left(\mathrm{i}\omega_2 \bar{\Lambda}_1 - \mathrm{i}\omega_1 \Lambda_2\right) \beta_6 + (\mathrm{i}\omega_2 - \mathrm{i}\omega_1)\, \bar{\Lambda}_1 \Lambda_2 \beta_7] \exp\left(\mathrm{i}\left(\omega_2 - \omega_1\right) T_0\right) \\
& + A_1 \bar{A}_1 \left(\beta_1 + \Lambda_1 \left(\bar{\Lambda}_1 \beta_2 + \beta_4 + \mathrm{i}\omega_1 \left(\beta_5 - \beta_6\right)\right)\right) \\
& + A_2 \bar{A}_2 \left(\beta_1 + \Lambda_2 \left(\bar{\Lambda}_2 \beta_2 + \beta_4 + \mathrm{i}\omega_2 \left(\beta_5 - \beta_6\right)\right)\right) \\
& + \frac{1}{2} f \exp\left(\mathrm{i}\left(\omega_2 T_0 + \sigma_1 T_1 + \tau\right)\right) + CC. \qquad (1.168)
\end{aligned}
$$

Let $\omega_2 > \omega_1$ for definiteness. We need to distinguish between the case of internal resonance $\omega_2 \approx 2\omega_1$ and the case of no internal resonance, i.e., ω_2 is away from $2\omega_1$. The case $\omega_1 > \omega_2$, $\omega_1 \approx 2\omega_2$ is analogous. When ω_2 is away from $2\omega_1$, the solvability conditions (1.155) are written in the form

$$\begin{aligned} q_{\omega_1} + \frac{1}{\Lambda_1} p_{\omega_1} &= 0, \\ q_{\omega_2} + \frac{1}{\Lambda_2} p_{\omega_2} + \frac{1}{2\Lambda_2} f \exp\left(\mathrm{i}\left(\sigma_1 T_1 + \tau\right)\right) &= 0, \end{aligned} \tag{1.169}$$

where

$$\begin{aligned} q_{\omega_1} &= -2\mathrm{i}\omega_1 \left(A_1^{'} + \mu_1 A_1\right) + \beta \Lambda_1 A_1^{'}, \\ q_{\omega_2} &= 2\mathrm{i}\omega_2 \left(A_2^{'} + \mu_1 A_2\right) + \beta \Lambda_2 A_2^{'}, \\ p_{\omega_1} &= -2\mathrm{i}\omega_1 \Lambda_1 \left(A_1^{'} + \mu_2 A_1\right) - \beta A_1^{'}, \\ p_{\omega_2} &= -2\mathrm{i}\omega_2 \Lambda_2 \left(A_2^{'} + \mu_2 A_2\right) - \beta A_2^{'}. \end{aligned} \tag{1.170}$$

Thus, when there is no internal resonance, the first approximation is not influenced by the non-linear terms; it is essentially a solution of the corresponding linear problem.

Actually, the solutions of the differential equations below

$$\begin{aligned} &\left(\beta\Lambda_1 - 2\mathrm{i}\omega_1 + \frac{2\mathrm{i}\omega_1\Lambda_1 + \beta}{\bar{\Lambda}_1}\right) A_1^{'} + \left(\frac{2\mathrm{i}\omega_1\Lambda_1\mu_2}{\bar{\Lambda}_1} - 2\mathrm{i}\omega_1\mu_1\right) A_1 = 0, \\ &\left(\beta\Lambda_2 - 2\mathrm{i}\omega_2 + \frac{2\mathrm{i}\omega_2\Lambda_2 + \beta}{\bar{\Lambda}_2}\right) A_2^{'} + \left(\frac{2\mathrm{i}\omega_2\Lambda_2\mu_2}{\bar{\Lambda}_2} - 2\mathrm{i}\omega_2\mu_1\right) A_2 \\ &\quad = -\frac{1}{2\Lambda_2} f \exp\left[\mathrm{i}\left(\sigma_1 T_1 + \tau\right)\right] \end{aligned} \tag{1.171}$$

are

$$\begin{aligned} A_1\left(T_1\right) &= \frac{1}{2} a_1 \exp\left(-\nu_1 T_1 + \mathrm{i}\Theta_1\right), \\ A_2\left(T_1\right) &= \frac{1}{2} a_2 \exp\left(-\nu_2 T_1 + \mathrm{i}\Theta_2\right) \\ &\quad + \frac{f\left(\nu_2 - \mathrm{i}\sigma_1\right)}{2\mathrm{Im}\Lambda_2 \mathrm{Im}\kappa_2 \left(\nu_2^2 + \sigma_1^2\right)} \exp\left[\mathrm{i}\left(\sigma_1 T_1 + \tau\right)\right], \end{aligned} \tag{1.172}$$

where a_n and Θ_n are the real constants:

$$\nu_n = \frac{2\omega_n(\mu_1+\mu_2)}{4\omega_n - \beta\left(\mathrm{Im}\Lambda_n + \frac{1}{\mathrm{Im}\Lambda_n}\right)},$$
$$\kappa_2 = -4\omega_2 i + \beta\left(\mathrm{Im}\Lambda_2 + \frac{1}{\mathrm{Im}\Lambda_2}\right)i. \tag{1.173}$$

As $t \to \infty$, $T_1 \to \infty$, and

$$A_1 \to 0, \quad A_2 \to \frac{f(\nu_2 - \mathrm{i}\sigma_1)}{2\mathrm{Im}\Lambda_2\mathrm{Im}\kappa_2\left(\nu_2^2+\sigma_1^2\right)}\exp\left[\mathrm{i}\left(\sigma_1 T_1+\tau\right)\right], \tag{1.174}$$

and according to (1.165), we obtain the following steady-state response:

$$x_1 = \frac{f(\nu_2 - \mathrm{i}\sigma_1)}{2\mathrm{Im}\Lambda_2\mathrm{Im}\kappa_2\left(\nu_2^2+\sigma_1^2\right)}\exp\left[\mathrm{i}\left(\omega_2 T_0+\sigma_1 T_1+\tau\right)\right] + CC,$$
$$y_1 = \Lambda_2\frac{f(\nu_2 - \mathrm{i}\sigma_1)}{2\mathrm{Im}\Lambda_2\mathrm{Im}\kappa_2\left(\nu_2^2+\sigma_1^2\right)}\exp\left[\mathrm{i}\left(\omega_2 T_0+\sigma_1 T_1+\tau\right)\right] + CC. \tag{1.175}$$

Therefore, the real solution is

$$x = \frac{F}{\varepsilon}\frac{1}{\mathrm{Im}\Lambda_2\mathrm{Im}\kappa_2\left(\nu_2^2+\sigma_1^2\right)}\left[\nu_2\cos\left(\Omega t+\tau\right)+\sigma_1\sin\left(\Omega t+\tau\right)\right] + O\left(\varepsilon^2\right),$$
$$y = \frac{F}{\varepsilon}\frac{1}{\mathrm{Im}\kappa_2\left(\nu_2^2+\sigma_1^2\right)}\left[\sigma_1\cos\left(\Omega t+\tau\right)-\nu_2\sin\left(\Omega t+\tau\right)\right] + O\left(\varepsilon^2\right), \tag{1.176}$$

or it can be rewritten in the form

$$x = \frac{F}{\varepsilon}\frac{1}{\mathrm{Im}\Lambda_2\mathrm{Im}\kappa_2\left(\nu_2^2+\sigma_1^2\right)^{1/2}}\sin\left(\Omega t+\tau+\tilde{\gamma}_1\right) + O\left(\varepsilon^2\right),$$
$$y = \frac{F}{\varepsilon}\frac{1}{\mathrm{Im}\kappa_2\left(\nu_2^2+\sigma_1^2\right)^{1/2}}\sin\left(\Omega t+\tau+\tilde{\gamma}_2\right) + O\left(\varepsilon^2\right), \tag{1.177}$$

where $\tilde{\gamma}_1 = \arctan(\nu_2/\sigma_1)$, $\tilde{\gamma}_2 = -\arctan(\sigma_1/\nu_2)$.

Another situation occurs when the internal resonance $\omega_2 \approx 2\omega_1$ exists. Let us introduce the detuning parameter σ_2 and set

$$\omega_2 = 2\omega_1 - \varepsilon\sigma_2. \tag{1.178}$$

Taking into account (1.161), the solvability conditions for this case become

$$q_{\omega_1} + \frac{1}{\Lambda_1} p_{\omega_1} + \left(q_{\omega_2-\omega_1} + \frac{1}{\Lambda_1} p_{\omega_2-\omega_1} \right) \bar{A}_1 A_2 \exp\left(-\mathrm{i}\sigma_2 T_1\right) = 0,$$
$$q_{\omega_2} + \frac{1}{\Lambda_2} p_{\omega_2} + \left(q_{2\omega_1+\frac{1}{\Lambda_2} p_{2\omega_1}} \right) A_1^2 \exp\left(\mathrm{i}\sigma_2 T_1\right) + \frac{1}{2\Lambda_2} f \exp\left(\mathrm{i}\left(\sigma_1 T_1 + \tau\right)\right) = 0. \tag{1.179}$$

Here coefficients q_{ω_1}, q_{ω_2}, $q_{\omega_2-\omega_1}$, and $q_{2\omega_1}$ are the expressions in parentheses at the exponents with the corresponding powers (1.167) and p_{ω_1}, p_{ω_2}, $p_{\omega_2-\omega_1}$, and $p_{2\omega_1}$ are the expressions in brackets at the exponents with the corresponding powers (1.168):

$$\begin{aligned}
q_{\omega_1} &= -2\mathrm{i}\omega_1 \left(A_1^{'} + \mu_1 A_1 \right) + \beta \Lambda_1 A_1^{'}, \\
q_{\omega_2} &= 2\mathrm{i}\omega_2 \left(A_2^{'} + \mu_1 A_2 \right) + \beta \Lambda_2 A_2^{'}, \\
q_{2\omega_1} &= \alpha_1 + \Lambda_1^2 \alpha_2 + \mathrm{i}\omega_1 \alpha_3 + \Lambda_1 \alpha_4 + \mathrm{i}\omega_1 \Lambda_1 \alpha_5 + \mathrm{i}\omega_1 \Lambda_1 \alpha_6 + \mathrm{i}\omega_1 \Lambda_1^2 \alpha_7, \\
q_{\omega_2-\omega_1} &= 2\alpha_1 + 2\bar{\Lambda}_1 \Lambda_2 \alpha_2 + \left(\mathrm{i}\omega_2 - \mathrm{i}\omega_1\right) \alpha_3 + \left(\Lambda_2 + \bar{\Lambda}_1\right) \alpha_4 \\
&\quad + \left(\mathrm{i}\omega_2 \Lambda_2 - \mathrm{i}\omega_1 \bar{\Lambda}_1\right) \alpha_5 + \left(\mathrm{i}\omega_2 \bar{\Lambda}_1 - \mathrm{i}\omega_1 \Lambda_2\right) \alpha_6 + \left(\mathrm{i}\omega_2 - \mathrm{i}\omega_1\right) \bar{\Lambda}_1 \Lambda_2 \alpha_7, \\
p_{\omega_1} &= -2\mathrm{i}\omega_1 \Lambda_1 \left(A_1^{'} + \mu_2 A_1 \right) - \beta A_1^{'}, \\
p_{\omega_2} &= -2\mathrm{i}\omega_2 \Lambda_2 \left(A_2^{'} + \mu_2 A_2 \right) - \beta A_2^{'}, \\
p_{2\omega_1} &= \beta_1 + \Lambda_1^2 \beta_2 + \mathrm{i}\omega_1 \beta_3 + \Lambda_1 \beta_4 + \mathrm{i}\omega_1 \Lambda_1 \beta_5 + \mathrm{i}\omega_1 \Lambda_1 \beta_6 + \mathrm{i}\omega_1 \Lambda_1^2 \beta_7, \\
p_{\omega_2-\omega_1} &= 2\beta_1 + 2\bar{\Lambda}_1 \Lambda_2 \beta_2 + \left(\mathrm{i}\omega_2 - \mathrm{i}\omega_1\right) \beta_3 + \left(\Lambda_2 + \bar{\Lambda}_1\right) \beta_4 \\
&\quad + \left(\mathrm{i}\omega_2 \Lambda_2 - \mathrm{i}\omega_1 \bar{\Lambda}_1\right) \beta_5 + \left(\mathrm{i}\omega_2 \bar{\Lambda}_1 - \mathrm{i}\omega_1 \Lambda_2\right) \beta_6 + \left(\mathrm{i}\omega_2 - \mathrm{i}\omega_1\right) \bar{\Lambda}_1 \Lambda_2 \beta_7.
\end{aligned} \tag{1.180}$$

For convenience let us introduce the polar notation

$$A_m = \frac{1}{2} a_m \exp\left(\mathrm{i}\Theta_m\right), \qquad m = 1, 2, \tag{1.181}$$

where a_m and Θ_m are the real functions of T_1. Substitution of (1.181) into (1.179) yields

$$\left(a_1^{'} + \mathrm{i} a_1 \Theta_1^{'} \right) + \nu_1 a_1 + \frac{1}{2\kappa_1} a_1 a_2 \left[\varphi + \mathrm{i}\psi\right] \exp\left(\mathrm{i}\gamma_2\right) = 0,$$
$$\left(a_2^{'} + \mathrm{i} a_2 \Theta_2^{'} \right) + \nu_2 a_2 + \frac{1}{2\kappa_2} a_1^2 \left[\zeta + \mathrm{i}\eta\right] \exp\left(-\mathrm{i}\gamma_2\right) + \frac{f}{\kappa_2 \Lambda_2} \exp\left(\mathrm{i}\gamma_1\right) = 0. \tag{1.182}$$

In the preceding expressions the following notations were introduced:

$$\varphi = \mathrm{Re}\left(q_{\omega_2-\omega_1} + \frac{1}{\Lambda_1} p_{\omega_2-\omega_1}\right), \quad \psi = \mathrm{Im}\left(q_{\omega_2-\omega_1} + \frac{1}{\Lambda_1} p_{\omega_2-\omega_1}\right),$$

$$\zeta = \mathrm{Re}\left(q_{2\omega_1} + \frac{1}{\Lambda_2} p_{2\omega_1}\right),$$

$$\eta = \mathrm{Im}\left(q_{2\omega_1} + \frac{1}{\Lambda_2} p_{2\omega_1}\right),$$

$$\kappa_n = -4\omega_n \mathrm{i} + \beta\left(\mathrm{Im}\Lambda_n + \frac{1}{\mathrm{Im}\Lambda_n}\right)\mathrm{i}, \qquad n = 1, 2,$$

$$\gamma_1 = \sigma_1 T_1 + \tau - \Theta_2, \qquad \gamma_2 = \Theta_2 - 2\Theta_1 - \sigma_2 T_1, \tag{1.183}$$

and ν_1 and ν_2 are defined as in (1.158).

Separating (1.182) into real and imaginary parts and taking into account that according to (1.145) Λ_n $(n = 1, 2)$ is the imaginary value, we obtain

$$\begin{aligned}
a'_1 &= -\nu_1 a_1 - \frac{a_1 a_2}{2\mathrm{Im}\kappa_1}\left(\psi\cos\gamma_2 + \varphi\sin\gamma_2\right), \\
a_1\Theta'_1 &= \frac{a_1 a_2}{2\mathrm{Im}\kappa_1}\left(\varphi\cos\gamma_2 - \psi\sin\gamma_2\right), \\
a'_2 &= -\nu_2 a_2 - \frac{a_1^2}{2\mathrm{Im}\kappa_2}\left(\eta\cos\gamma_2 - \zeta\sin\gamma_2\right) + \frac{f}{\mathrm{Im}\kappa_2 \mathrm{Im}\Lambda_2}\cos\gamma_1, \\
a_2\Theta'_2 &= \frac{a_1^2}{2\mathrm{Im}\kappa_2}\left(\zeta\cos\gamma_2 + \eta\sin\gamma_2\right) + \frac{f}{\mathrm{Im}\kappa_2 \mathrm{Im}\Lambda_2}\sin\gamma_1.
\end{aligned} \tag{1.184}$$

For the steady-state response $a'_n = \gamma'_n = 0$, therefore,

$$\Theta'_1 = \frac{1}{2}\left(\sigma_1 - \sigma_2\right), \qquad \Theta'_2 = \sigma_1. \tag{1.185}$$

Two possibilities follow from (1.184). The first one is given by (1.174). It is the solution of the linear problem. Let us find functions a_1 and a_2 of T_1 according to the second possibility. It follows from the first two equations of (1.184) that

$$\begin{aligned}
\frac{4\omega_1\left(\mu_1 + \mu_2\right)}{a_2} &= -\psi\cos\gamma_2 - \varphi\sin\gamma_2, \\
\frac{\mathrm{Im}\kappa_1}{a_2}\left(\sigma_1 - \sigma_2\right) &= \varphi\cos\gamma_2 - \psi\sin\gamma_2.
\end{aligned} \tag{1.186}$$

So

$$a_2 = \left(\frac{16\omega_1^2\left(\mu_1 + \mu_2\right)^2 + \mathrm{Im}\kappa_1^2\left(\left(\sigma_1 - \sigma_2\right)^2\right)}{\varphi^2 + \psi^2}\right)^{1/2}. \tag{1.187}$$

Let us take $\sin\gamma_2$ and $\cos\gamma_2$ using, for example, the formulas by Cramer:

$$\cos\gamma_2 = \frac{\Delta_1}{\Delta}, \qquad \sin\gamma_2 = \frac{\Delta_2}{\Delta}, \tag{1.188}$$

where

$$\begin{aligned}
\Delta &= \begin{vmatrix} -\psi & -\phi \\ \varphi & -\psi \end{vmatrix} = \varphi^2 + \psi^2, \\
\Delta_1 &= -\frac{1}{a_2}\begin{vmatrix} 2\mathrm{Im}\kappa_1\nu_1 & \varphi \\ \mathrm{Im}\kappa_1(\sigma_1-\sigma_2) & \psi \end{vmatrix} \\
&= \frac{1}{a_2}\left(4\omega_1(\mu_1+\mu_2)\psi + \mathrm{Im}\kappa_1(\sigma_1-\sigma_2)\varphi\right), \\
\Delta_2 &= \frac{1}{a_2}\begin{vmatrix} -\psi & 2\mathrm{Im}\kappa_1\nu_1 \\ \varphi & \mathrm{Im}\kappa_1(\sigma_1-\sigma_2) \end{vmatrix} \\
&= \frac{1}{a_2}\left(-\mathrm{Im}\kappa_1(\sigma_1-\sigma_2)\psi - 4\omega_1(\mu_1+\mu_2)\varphi\right).
\end{aligned} \tag{1.189}$$

Then a biquadratic equation relative to a_1 follows from the last two equations of (1.184):

$$\begin{aligned}
&a_1^4(\zeta^2+\eta^2) + 4a_1^2[-2\omega_2(\mu_1+\mu_2)a_2(\eta\cos\gamma_2 - \zeta\sin\gamma_2) \\
&-\mathrm{Im}\kappa_2\sigma_1 a_2(\zeta\cos\gamma_2 + \eta\sin\gamma_2)] \\
&+4\left[4\omega_2^2(\mu_1+\mu_2)^2 + \mathrm{Im}\kappa_2^2\sigma_1^2\right]a_2^2 - \frac{4f^2}{(\mathrm{Im}\Lambda_2)^2} = 0.
\end{aligned} \tag{1.190}$$

Finally, we obtain the expression for a_1:

$$a_1 = \left[-\frac{p}{2} \pm \left(\left(\frac{p}{2}\right)^2 - q\right)^{\frac{1}{2}}\right]^{\frac{1}{2}}, \tag{1.191}$$

where

$$\begin{aligned}
p &= \frac{4a_2}{\zeta^2+\eta^2}\left[-2\omega_2(\mu_1+\mu_2)(\eta\cos\gamma_2 - \zeta\sin\gamma_2) - \mathrm{Im}\kappa_2\sigma_1(\zeta\cos\gamma_2 + \eta\sin\gamma_2)\right], \\
q &= \frac{1}{\zeta^2+\eta^2}\left\{4a_2^2\left[4\omega_2^2(\mu_1+\mu_2)^2 + \mathrm{Im}\kappa_2^2\sigma_1^2\right] - \frac{4f^2}{(\mathrm{Im}\Lambda_2)^2}\right\}.
\end{aligned} \tag{1.192}$$

Thus, the unknown functions in (1.165) were defined. It follows from (1.141), (1.165), and (1.181) that

$$x = \varepsilon\left[\frac{1}{2}a_1\exp\left[\mathrm{i}\left(\Theta_1+\omega_1 T_0\right)\right]+\frac{1}{2}a_2\exp\left[\mathrm{i}\left(\Theta_2+\omega_2 T_0\right)\right]+CC\right]+O\left(\varepsilon^2\right),$$
$$y = \varepsilon\left[\frac{1}{2}\Lambda_1 a_1\exp\left[\mathrm{i}\left(\Theta_1+\omega_1 T_0\right)\right]+\frac{1}{2}\Lambda_2 a_2\exp\left[\mathrm{i}\left(\Theta_2+\omega_2 T_0\right)\right]+CC\right]+O\left(\varepsilon^2\right). \tag{1.193}$$

Then, the real solution is as follows:

$$x = \varepsilon\left\{a_1\cos\left[\frac{1}{2}\left(\Omega t+\tau-\gamma_1-\gamma_2\right)\right]+a_2\cos\left(\Omega t+\tau-\gamma_1\right)\right\}+O\left(\varepsilon^2\right),$$
$$y = -\varepsilon\left\{a_1\mathrm{Im}\Lambda_1\sin\left[\frac{1}{2}\left(\Omega t+\tau-\gamma_1-\gamma_2\right)\right]a_2\mathrm{Im}\Lambda_2\sin\left(\Omega t+\tau-\gamma_1\right)\right\}+O\left(\varepsilon^2\right). \tag{1.194}$$

Here a_1 and a_2 are defined by (1.187) and (1.191).

Let us consider the expression for a_1 (1.191). When

$$\{[(p/2)>0]\wedge(q>0)\}\vee[(p/2)^2<q], \tag{1.195}$$

there are no real values of a_1 defined by (1.191) and the response must be given by (1.177). When

$$[(p/2)^2>q]\wedge(q<0), \tag{1.196}$$

there is one real solution defined by (1.191). Therefore, the response is one of the two possibilities given by (1.177) and (1.194). When

$$[(p/2)<0]\wedge[(p/2)^2>q]\wedge(q>0), \tag{1.197}$$

there are two real solutions defined by (1.191). Therefore, the response is one of the three possibilities given by (1.177) and (1.194).

Figure 1.42 depicts frequency-response curves. a_1 and a_2 are plotted as functions of σ_1 for $\sigma_2 = 0$. The dashed line with a peak at $\sigma_1 = 0$ corresponds to $a_1 = 0$ and is a solution of the corresponding linear problem. Arrows indicate the jump phenomenon associated with varying the frequency of external excitation Ω. The perturbation solution obtained is the superposition of two submotions with amplitudes a_1 and a_2 and frequencies ω_1 and ω_2, respectively. To compare the perturbation and numerical solutions, we performed an approximate harmonic analysis of solutions $x(t)$ and $y(t)$, obtained numerically. These functions are expanded in Fourier series formed from cosines

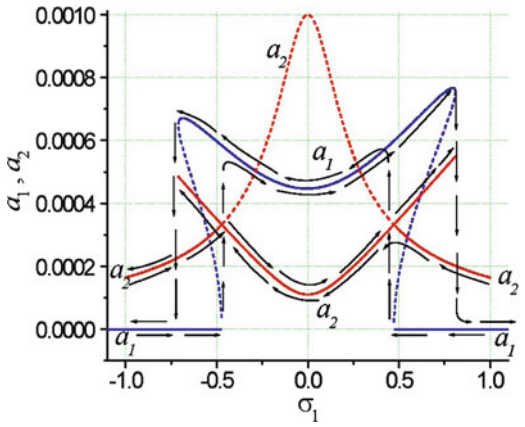

Fig. 1.42 Frequency-response curves; $\sigma_2 = 0$, $\Omega \approx \omega_2$

$$x(t) = \frac{a_0}{2} + \sum_{k=1}^{\infty} a_k \cos \frac{k\pi t}{T},$$

$$a_k = \frac{2}{T} \int_0^T x(t) \cos \frac{k\pi t}{T} \mathrm{d}t, \quad k = 0, 1, 2\ldots, \tag{1.198}$$

where T is the period of integration, $0 \le t \le T$. The coefficients of the Fourier series were calculated approximately. The following parameters of set (1.140) were accepted: $\alpha = 200$, $\beta = 10$, $\alpha_1 = 9.985 \times 10^2$, $\alpha_2 = 2 \times 10^3$, $\alpha_3 = 7.9588 \times 10^3$, $\alpha_4 = 0.002$, $\alpha_5 = -4.0794 \times 10^3$, $\alpha_6 = 4.0002 \times 10^3$, $\alpha_7 = 8.0005 \times 10^3$, $\beta_1 = 29.9975$, $\beta_2 = -0.001$, $\beta_3 = -4.1594 \times 10^3$, $\beta_4 = -1.9997 \times 10^3$, $\beta_5 = -7.9188 \times 10^3$, $\beta_6 = 0.7959$, $\beta_7 = -0.4083$.

Parameters $\alpha = 200$, $\beta = 10$ correspond to natural frequencies $\omega_1 = 10$, $\omega_2 = 20$, i.e., $\omega_2 = 2\omega_1$. The curves in Fig. 1.43 were plotted using points $(\frac{k\pi}{T}, \frac{a_0}{2} + a_k)$. Figure 1.43 demonstrates good agreement of the perturbation and numerical solutions: panel a characterizes $x(t)$ as harmonic motion with amplitude $a_2 \approx 1.5 \times 10^{-4}$ and frequency $\omega_2 = 20$; panel b characterizes $x(t)$ as a superposition of harmonic motions with amplitude $a_1 \approx 4 \times 10^{-4}$, frequency $\omega_1 = 10$, amplitude $a_2 \approx 1.5 \times 10^{-4}$, and frequency $\omega_2 = 20$.

In Figs. 1.45 and 1.46 one can see the saturation phenomenon. As f increases from zero, a_2 also increases until it reaches the value $a_2 = 3.5 \times 10^{-4}$. In Fig. 1.44 it reaches the value $a_2 = 1.125 \times 10^{-4}$, whereas in Fig. 1.46 a_1 is zero. This agrees with the solution of the corresponding linear problem. Then a_2 saves the constant value and a_1 starts to increase. Approximate harmonic analysis of Fig. 1.45 (Fig. 1.47) demonstrates good agreement of the theoretical prediction presented in Fig. 1.44 (Fig. 1.46) and the corresponding numerical solution of (1.140).

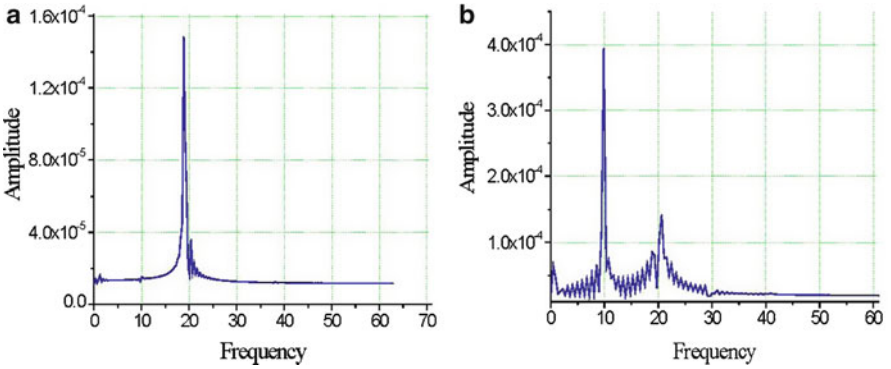

Fig. 1.43 Comparison of analytical results presented on the frequency-response curves (Fig. 1.42) with numerical integration of (2): (**a**) $\Omega = 19$ ($\delta_1 = -1, \delta_2 = 0$), $f = 0.01$; (**b**) $\Omega = 20$ ($\delta_1 = 0, \delta_2 = 0$), $f = 0.01$

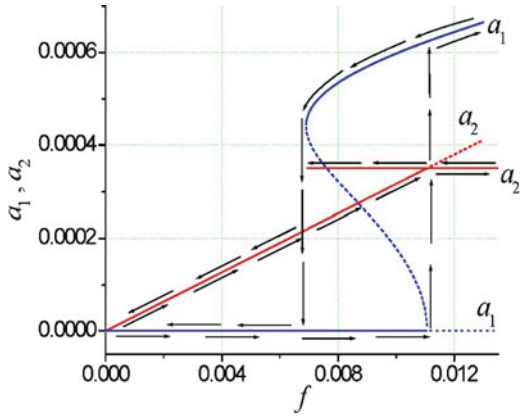

Fig. 1.44 Amplitudes a_1, a_2 versus the amplitude of external excitation f; $\Omega \approx \omega_2, \sigma_1 = -0.5, \sigma_2 = 0$

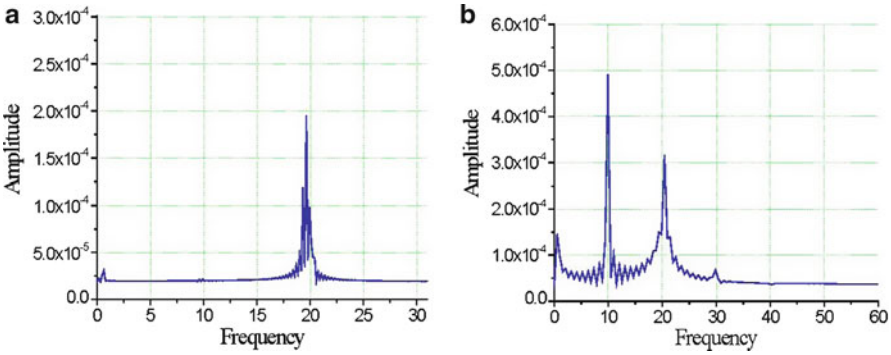

Fig. 1.45 Comparison of analytical results presented in Fig. 1.44 with numerical integration of (1.140): (**a**) $\Omega = 19.5$ ($\sigma_1 = -0.5, \sigma_2 = 0$), $f = 0.0065$; (**b**) $\Omega = 19.5$ ($\sigma_1 = -0.5, \sigma_2 = 0$), $f = 0.01$

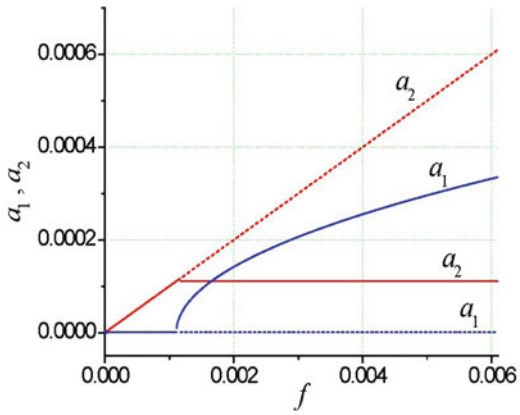

Fig. 1.46 Amplitudes a_1, a_2 versus the amplitude of external excitation f; $\Omega \approx \omega_2, \sigma_1 = \sigma_2 = 0$

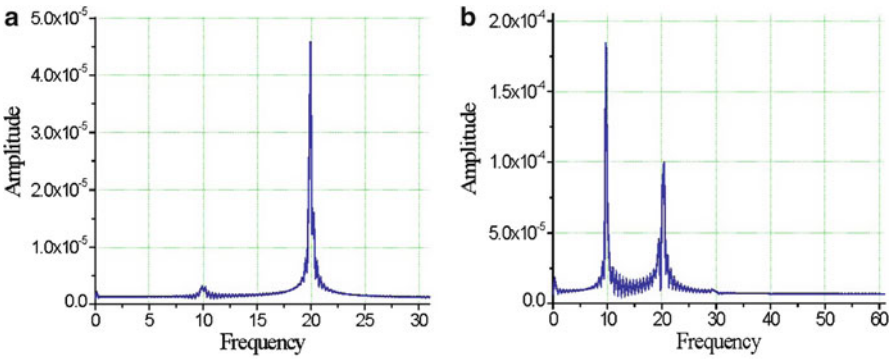

Fig. 1.47 Comparison of analytical results presented in Fig. 1.46 with numerical integration of (1.140): (**a**) $\Omega = 20$ ($\sigma_1 = \sigma_2 = 0$), $f = 0.0006$; (**b**) $\Omega = 20$ ($\sigma_1 = \sigma_2 = 0$), $f = 0.003$

1.5.2.3 Rigid Magnetic Materials: Conditions for Chaotic Vibrations of a Rotor in Various Control Parameter Planes

In the case of rigid magnetic materials, the hysteretic properties of system (1.137) can be considered using the Bouc–Wen hysteretic model. It was shown [35] that this modeling mechanism for energy dissipation was sufficiently accurate to model loops of various shapes in accordance with a real experiment, reflecting the behavior of hysteretic systems from very different fields. The hysteretic model of the rotor-MHDB system is as follows:

$$\ddot{x} = P_r\left(\rho, \dot{\rho}, \dot{\phi}\right)\cos\phi - P_\tau\left(\rho, \dot{\phi}\right)\sin\phi - \gamma_m\dot{x} - \lambda_m\left[\delta\left(x - x_0\right) + (1-\delta)\, z_1\right],$$

$$\begin{aligned}
\ddot{y} &= P_r\left(\rho,\dot{\rho},\dot{\phi}\right)\sin\phi + P_\tau\left(\rho,\dot{\phi}\right)\cos\phi - \gamma_m\dot{y} \\
&\quad -\lambda_m\left[\delta\left(y-y_0\right)+\left(1-\delta\right)z_2\right] + Q_0 + Q\sin\Omega t, \\
\dot{z}_1 &= \left[k_z - \left(\gamma+\beta\,\mathrm{sgn}\left(\dot{x}\right)\ \mathrm{sgn}\left(z_1\right)\right)\ |z_1|^n\right]\dot{x}, \\
\dot{z}_2 &= \left[k_z - \left(\gamma+\beta\,\mathrm{sgn}\left(\dot{y}\right)\ \mathrm{sgn}\left(z_2\right)\right)\ |z_2|^n\right]\dot{y}.
\end{aligned} \tag{1.199}$$

Here z_1 and z_2 are the hysteretic forces. The case $\delta = 0$ corresponds to maximal hysteretic dissipation and $\delta = 1$ to the absence of hysteretic forces in the system; parameters $(k_z, \beta, n) \in R^+$ and $\gamma \in R$ govern the shape of the hysteresis loops.

The conditions for chaotic vibrations of a rotor have been found using the approach based on an analysis of wandering trajectories. The description of the approach, its advantages over standard procedures, and a comparison with other approaches can be found, for example, in [35, 38, 40].

The stability of motion depends on all the parameters of system (1.199), including the initial conditions. We traced the irregular vibrations of a rotor to sufficient accuracy in the parametric planes of amplitude of external excitation versus hysteretic dissipation (δ, Q), the amplitude versus frequency of external excitation (Ω, Q), the amplitude versus dynamic oil-film action characteristics (C, Q), and the amplitude versus the magnetic control parameters (γ_m, Q) and (λ_m, Q).

Chaos is not found in the absence of hysteresis when $\delta = 1$. The chaotic vibrations of a rotor are caused by hysteresis and for all chaotic regions presented $\delta \neq 1$. Thus in system (1.199), chaos was quantified using the following conditions:

$$\begin{array}{c}
\exists t^* \in [t_1, T] : \left\{\left(\left|x\left(t^*\right) - \tilde{x}\left(t^*\right)\right| > \alpha A_x\right) \vee \left(\left|y\left(t^*\right) - \tilde{y}\left(t^*\right)\right| > \alpha A_y\right)\right\} \\
\Downarrow \qquad\qquad\qquad\qquad \Downarrow \\
\begin{array}{cc}
\text{chaotic vibrations} & \text{chaotic vibrations} \\
\text{in the horizontal direction} & \text{in the vertical direction.}
\end{array}
\end{array} \tag{1.200}$$

Here $x(t)$, $\tilde{x}(t)$ and $y(t)$, $\tilde{y}(t)$ are nearby trajectories respectively, A_x and A_y are the characteristic vibration amplitudes of the rotor in the horizontal and vertical direction, respectively:

$$\begin{aligned}
A_x &= \frac{1}{2}\left|\max_{t_1\le t\le T} x\left(t\right) - \min_{t_1\le t\le T} x\left(t\right)\right|, \\
A_y &= \frac{1}{2}\left|\max_{t_1\le t\le T} y\left(t\right) - \min_{t_1\le t\le T} y\left(t\right)\right|.
\end{aligned} \tag{1.201}$$

$[t_1, T] \subset [t_0, T]$ and $[t_0, T]$ is the time interval over which the trajectories are considered. The interval $[t_0, t_1]$ is the time interval over which all transient processes are damped. The introduced parameter α is an auxiliary parameter such that $0 < \alpha < 1$. αA_x and αA_y are referred to as the divergence measures of the observable trajectories in the horizontal and vertical directions and, with the aid of the chosen parameter α, are *inadmissible* for the case of the *regularity* of motion.

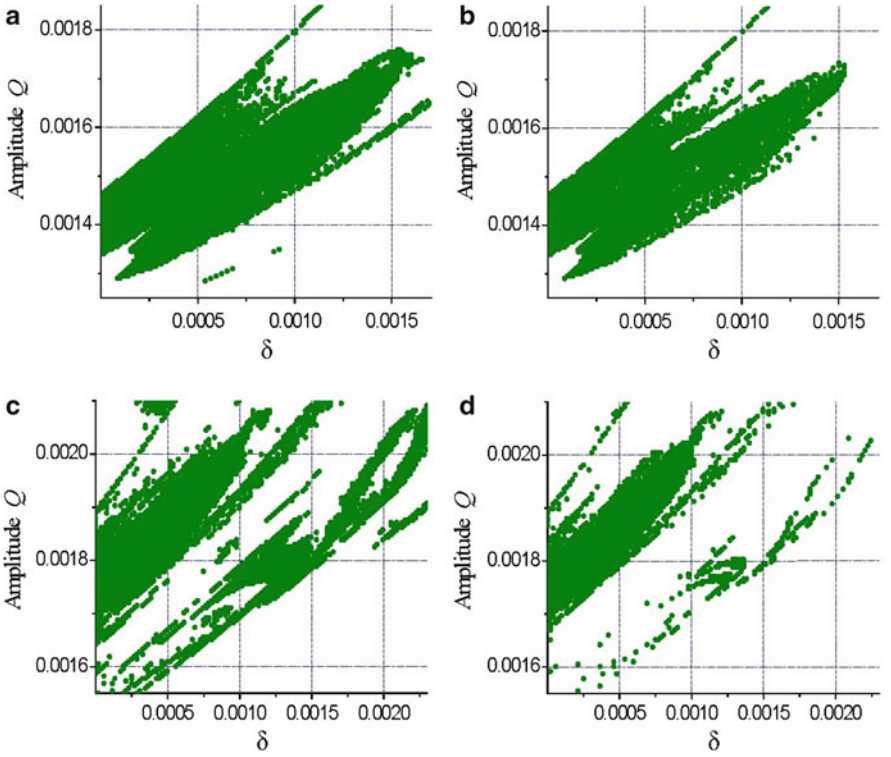

Fig. 1.48 Influence of hysteretic dissipation parameter δ on chaos in horizontal (**a, c**) and vertical (**b, d**) vibrations of rotor (1.199) in the case of rigid magnetic materials. The following parameters are fixed in (**a, b**): $C = 0.03$, $\gamma_m = 0.001$, $\lambda_m = 450$, $k_z = 0.000055$, $\gamma = 15$, $\beta = 0.25$, $n = 1.0$, $\Omega = 0.87$, $Q_0 = 0$, $x_0 = 0$, $y_0 = 0$, $x(0) = y(0) = 10^{-8}$, $\dot{x}(0) = \dot{y}(0) = 0$, $z_1(0) = z_2(0) = 0$; (c, d): $C = 0.2$, $\gamma_m = 0$, $\lambda_m = 500$, $k_z = 0.000055$, $\gamma = 15$, $\beta = 0.25$, $n = 1.0$, $\Omega = 0.87$, $Q_0 = 0$, $x_0 = 0$, $y_0 = 0$, $x(0) = y(0) = 10^{-8}$, $\dot{x}(0) = \dot{y}(0) = 0$, $z_1(0) = z_2(0) = 0$

If inequality (1.200) is satisfied in some nodal point of the sampled control parameter space, then the motion is chaotic (including transient and alternating chaos). The manifold of all such nodal points of the investigated control parameter space defines the domains of chaotic behavior for the considered system.

Figure 1.48 displays the regions of rotor chaotic vibrations in the (δ, Q) plane. Part of this plane $(10^{-7} < \delta \leq 0.0017; 0.00125 < Q \leq 0.00185)$ (panels a and b) and $(10^{-7} < \delta \leq 0.0023; 0.00155 < Q \leq 0.0021)$ (panels c and d) was sampled by means of a uniform rectangular grid. For this purpose two families of straight lines were drawn through dividing points of the axes

$$\begin{aligned} \delta^i &= i\Delta\delta, \quad i = 0, 1, \ldots, 120, \\ Q^j &= j\Delta Q, \quad j = 0, 1, \ldots, 120. \end{aligned} \tag{1.202}$$

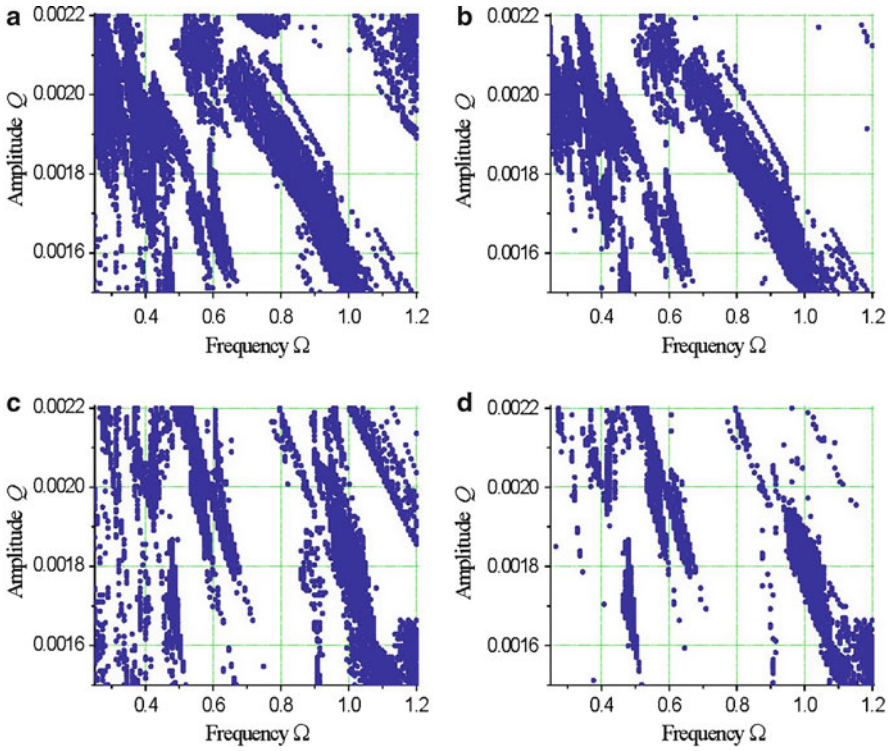

Fig. 1.49 Chaotic regions for horizontal (**a, c**) and vertical (**b, d**) vibrations of rotor (28) in (Ω, Q) parametric plane with decrease of the hysteretic dissipation value (**a, b**) $\delta = 0.0001$; (**c, d**) $\delta = 0.0013$ with other parameters of the system fixed: $C = 0.2$, $\gamma_m = 0$, $\lambda_m = 500$, $k_z = 0.000055$, $\gamma = 15$, $\beta = 0.25$, $n = 1.0$, $Q_0 = 0$, $x_0 = 0$, $y_0 = 0$, $x(0) = y(0) = 10^{-8}$, $\dot{x}(0) = \dot{y}(0) = 0$, $z_1(0) = z_2(0) = 0$

Here $\Delta\delta = 1.4165 \times 10^{-5}$, $\Delta Q = 5 \times 10^{-6}$ (panels a and b), $\Delta\delta = 1.91658 \times 10^{-5}$, $\Delta Q = 4.58333 \times 10^{-6}$ (panels c and d).

The time period for the simulation T is of $\frac{200\pi}{\Omega}$ in non-dimentional time units. During the computations, two-thirds of time period T corresponds to the time interval $[t_0, t_1]$, where transient processes are damped. The integration step size is $0.02\frac{\pi}{\Omega}$. The initial conditions of the nearby trajectories differ by less than 0.5% of characteristic vibration amplitudes, e.g., the starting points of these trajectories are in the rectangle $(|x(t_0) - \tilde{x}(t_0)| < 0.005A_x, |y(t_0) - \tilde{y}(t_0)| < 0.005A_y)$. The parameter α is chosen to be equal to $\frac{1}{3}$.

All domains have a complex structure. There are a number of scattered points, streaks, and islets here. Such a structure is characteristic of domains where chaotic vibrations are possible. For each aggregate of control parameters there is some critical value of the hysteretic dissipation $(1 - \delta_c r)$ that if $(1 - \delta) < (1 - \delta_c r)$, then chaos is not observed in the system under consideration.

In Fig. 1.49 chaotic regions for the horizontal and vertical vibrations of a rotor are depicted in the (Ω, Q) parametric plane $(0.25 < \Omega \leq 1.2; 0.0015 < Q \leq 0.0022)$.

The time period for the simulation T and other numerical integration characteristics are the same as for (δ, Q) parametric plane, $\Delta\Omega = 7.91667 \times 10^{-3}$, $\Delta Q = 5.83333e \times 10^{-6}$. One can observe that for the larger hysteretic dissipation $(1 - \delta)$, $\delta = 0.0001$ the chaotic regions areas are larger.

Figure 1.50 shows the phase portraits, hysteretic loops, and Poincar maps of chaotic motion of a rotor. The parameters of motion correspond to the parameters of the chaotic region depicted in Fig. 1.49a, b. The phase portraits, hysteretic loops, and Poincar maps of the periodic rotor motion that also agree well with the obtained regions of regular/irregular behavior of the rotor depicted in Fig. 1.49a, b are shown in Fig. 1.51.

The influence of the dynamic oil-film action characteristics on chaos occurring in the rotor motion can be observed in Fig. 1.52. One can see the restraining of chaotic regions with decreasing of hysteretic dissipation $(1 - \delta)$. The (C, Q) parametric plane was uniformly sampled by 120×120 nodal points in the rectangles $(0 < C \leq 1.5;\ 0.0015 < Q \leq 0.0021)$, $\Delta C = 0.0125$, $\Delta Q = 5 \times 10^{-6}$ (panels a and b) and $(0 < C \leq 1.5;\ 0.0015 < Q \leq 0.00225)$, $\Delta C = 0.0125$, $\Delta Q = 6.25 \times 10^{-6}$ (panels c and d).

The influence of the magnetic control parameters γ_m, λ_m on chaos occurring in the rotor vibrations can be observed in Figs. 1.53 and 1.54. The (γ_m, Q) and (λ_m, Q) parametric planes were uniformly sampled by 120×120 nodal points in the rectangles $(0 < \gamma_m \leq 0.09;\ 0.00165 < Q \leq 0.0019)$, $\gamma_m = 7.5 \times 10^{-4}$, $\Delta Q = 2.08333 \times 10^{-6}$, Fig. 1.44a, b; $(0 < \gamma_m \leq 0.15;\ 0.00155 < Q \leq 0.0023)$, $\gamma_m = 1.25 \times 10^{-3}$, $\Delta Q = 6.25 \times 10^{-6}$ Fig. 1.44c, d; $(450 < \lambda_m \leq 630;\ 0.00145 < Q \leq 0.0025)$, $\Delta\lambda_m = 1.5$, $\Delta Q = 8.75 \times 10^{-6}$, Fig. 1.54a and b; $(420 < \lambda_m \leq 800;\ 0.0015 < Q \leq 0.0043)$, $\Delta\lambda_m = 3.16667$, $\Delta Q = 2.33333 \times 10^{-5}$, Fig. 1.54c, d. The time period for simulation T and other numerical integration characteristics are the same as for the (δ, Q) parametric plane.

Impact phenomena are possible in the bearings for both chaotic and periodic rotor motion at large amplitudes of the external harmonic excitation. An analysis of the rotor behavior after a collision with the bearings is not considered in this paper because the model described does not have a physical meaning in this case. To see if the rotor chaotic motion is accompanied by an increase in the amplitude of vibration, the amplitude level contours of the horizontal and vertical vibrations of the rotor were obtained. In Fig. 1.55, the amplitude level contours are presented in the (γ_m, Q) parametric plane with the same parameters as in Fig. 1.53a, b. Some "consonance" between the chaotic vibrations regions and the amplitude level contours is observed. At that level the amplitudes of chaotic rotor vibrations are greater in comparison to the periodic vibrations.

In Fig. 1.56 the amplitude level contours are presented in the (C, Q) parametric plane with the same parameters as in Fig. 1.52a, b. Although some "consonance" between the chaotic regions of vibrations and the amplitude level contours is observed, it cannot be concluded that chaos leads to an essential increase in the rotor vibration amplitude [40].

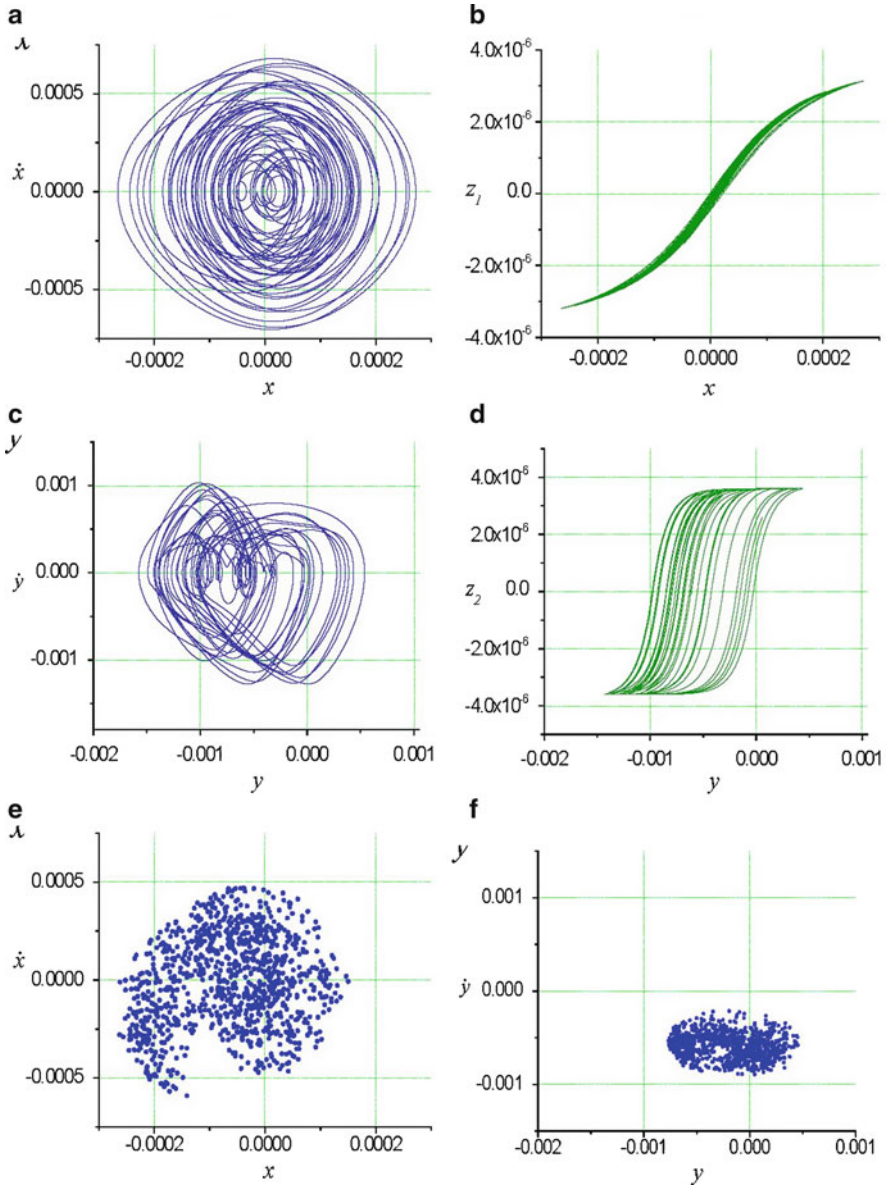

Fig. 1.50 Phase portraits (**a, c**), hysteresis loops (**b, d**), and Poincar maps (**e, f**) of rotor motion that agree with the chaotic regions in Fig. 1.49 (**a, b**). The parameters $\Omega = 0.87$, $Q = 0.00177$, $\delta = 0.0001$, $C = 0.2$, $\gamma_m = 0$, $\lambda_m = 500$, $k_z = 0.000055$, $\gamma = 15$, $\beta = 0.25$, $n = 1.0$, $Q_0 = 0$, $x_0 = 0$, $y_0 = 0$, $x(0) = y(0) = 10^{-8}$, $\dot{x}(0) = \dot{y}(0) = 0$, $z_1(0) = z_2(0) = 0$ are fixed

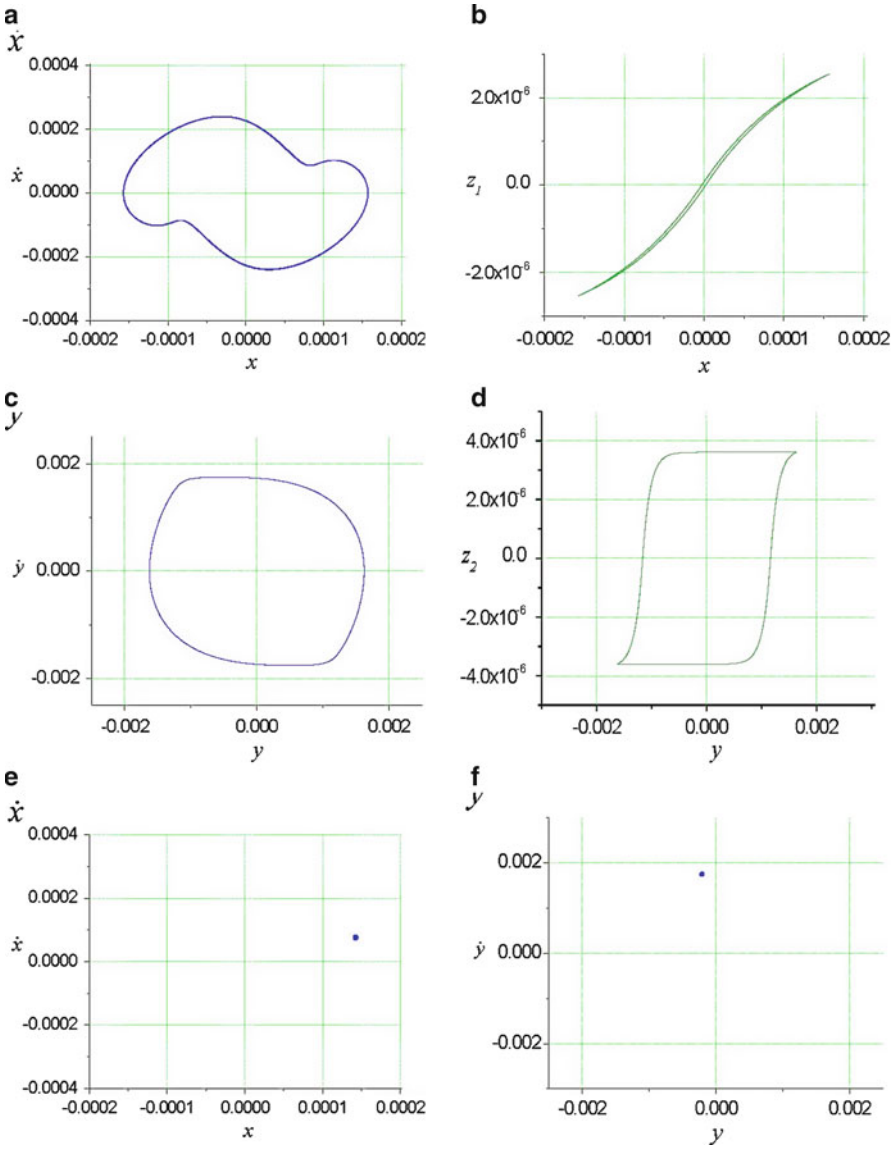

Fig. 1.51 Phase portraits (**a, c**), hysteresis loops (**b, d**), and Poincar maps (**e, f**) of periodic rotor motion that agree with regions of regular motion in Fig. 1.49a–d. The parameters $\Omega = 1.2$, $Q = 0.0017$, $\delta = 0.0001$, $C = 0.2$, $\gamma_m = 0$, $\lambda_m = 500$, $k_z = 0.000055$, $\gamma = 15$, $\beta = 0.25$, $n = 1.0$, $Q_0 = 0$, $x_0 = 0$, $y_0 = 0$, $x(0) = y(0) = 10^{-8}$, $\dot{x}(0) = \dot{y}(0) = 0$, $z_1(0) = z_2(0) = 0$ are fixed

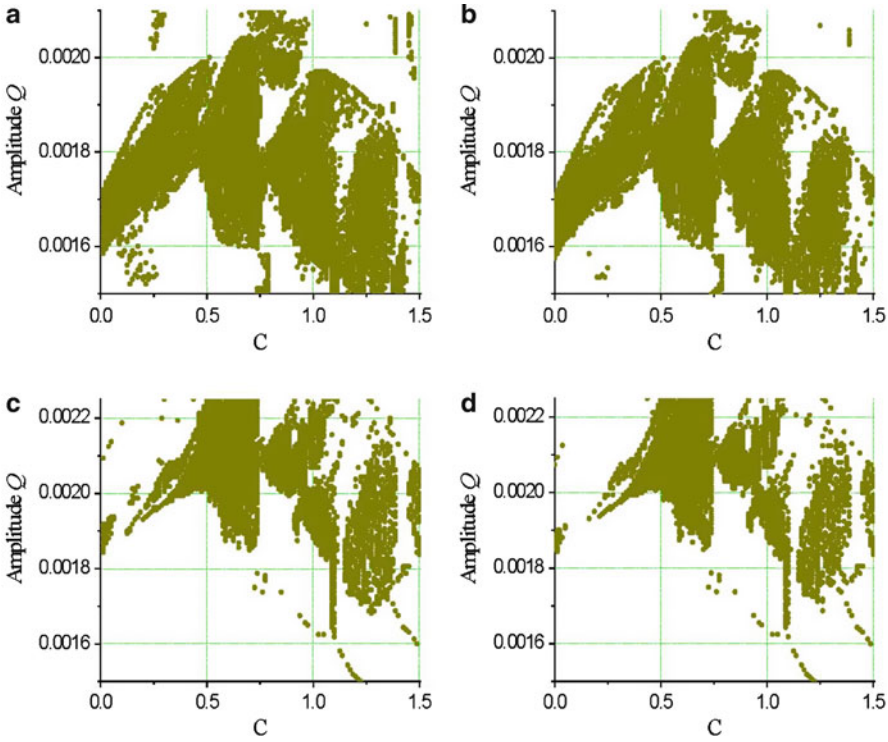

Fig. 1.52 Influence of dynamic oil-film action characteristics on chaos occurring in horizontal (**a, c**) and vertical (**b, d**) vibrations of rotor (1.199) in the case of rigid magnetic materials. The parametric planes (C,Q) are depicted at (**a**), (**b**) $\delta = 0.000001$, $\gamma_m = 0$ and (**c**), (**d**) $\delta = 0.001$, $\gamma_m = 0.03$ with other parameters of the system fixed: $\lambda_m = 500$, $k_z = 0.000055$, $\gamma = 15$, $\beta = 0.25$, $n = 1.0$, $Q_0 = 0$, $x_0 = 0$, $y_0 = 0$, $x(0) = y(0) = 10^{-8}$, $\dot{x}(0) = \dot{y}(0) = 0$, $z_1(0) = z_2(0) = 0$

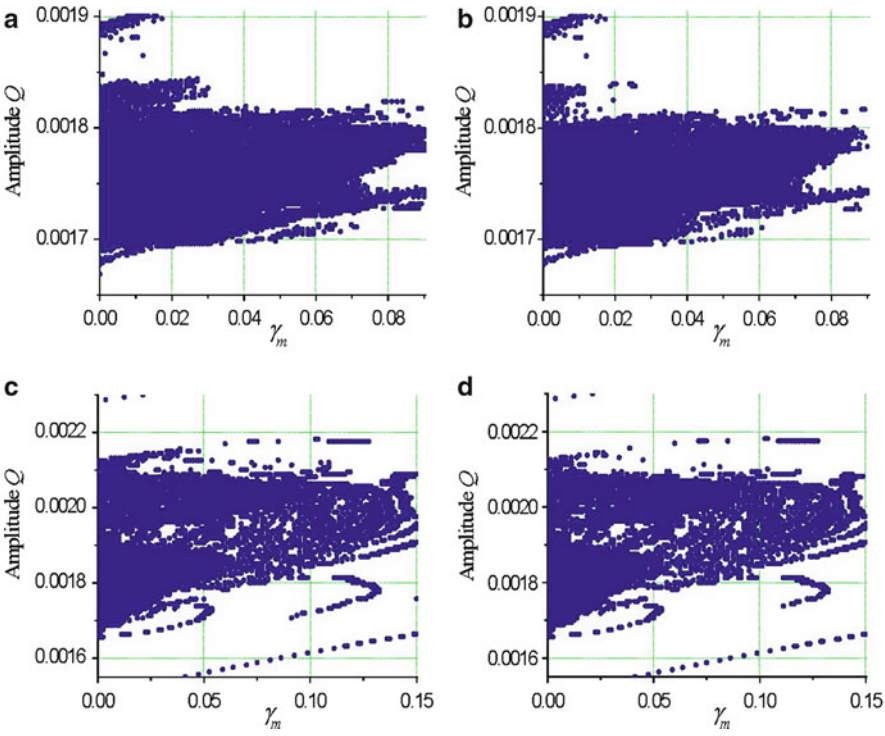

Fig. 1.53 Influence of magnetic control parameter γ_m on chaos occurring in horizontal (**a, c**) and vertical (**b, d**) vibrations of rotor (1.199) in the case of rigid magnetic materials. The parametric planes (γ_m, Q) are depicted at (**a, b**) $\delta = 0.000001$, $C = 0.2$ and (**c, d**) $\delta = 0.0005$, $C = 1$ with other parameters of the system fixed: $\lambda_m = 500$, $k_z = 0.000055$, $\gamma = 15$, $\beta = 0.25$, $n = 1.0$, $\Omega = 0.87$, $Q_0 = 0$, $x_0 = 0$, $y_0 = 0$, $x(0) = y(0) = 10^{-8}$, $\dot{x}(0) = \dot{y}(0) = 0$, $z_1(0) = z_2(0) = 0$

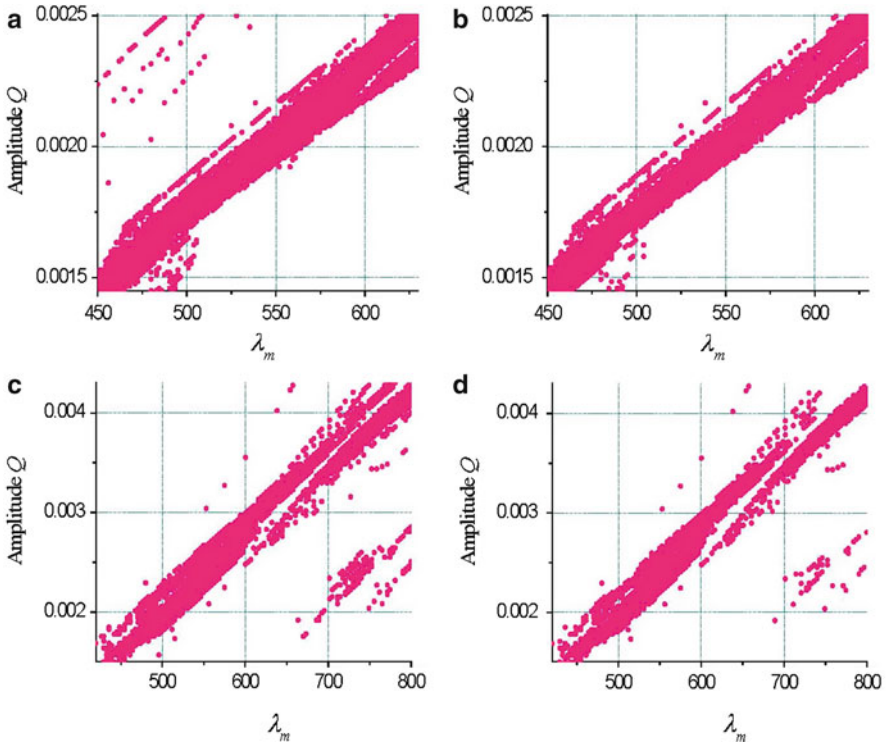

Fig. 1.54 Influence of magnetic control parameter γ_m on chaos occurring in horizontal (**a, c**) and vertical (**b, d**) vibrations of rotor (1.199) in the case of rigid magnetic materials. The parametric planes (γ_m, Q) are depicted at (**a, b**) $\delta = 0.000001$, $C = 0.2$, $\gamma_m = 0$ and (**c, d**) $\delta = 0.001$, $C = 1$, $\gamma_m = 0.005$ with other parameters of the system fixed: $k_z = 0.000055$, $\gamma = 15$, $\beta = 0.25$, $n = 1.0$, $\Omega = 0.87$, $Q_0 = 0$, $x_0 = 0$, $y_0 = 0$, $x(0) = y(0) = 10^{-8}$, $\dot{x}(0) = \dot{y}(0) = 0$, $z_1(0) = z_2(0) = 0$

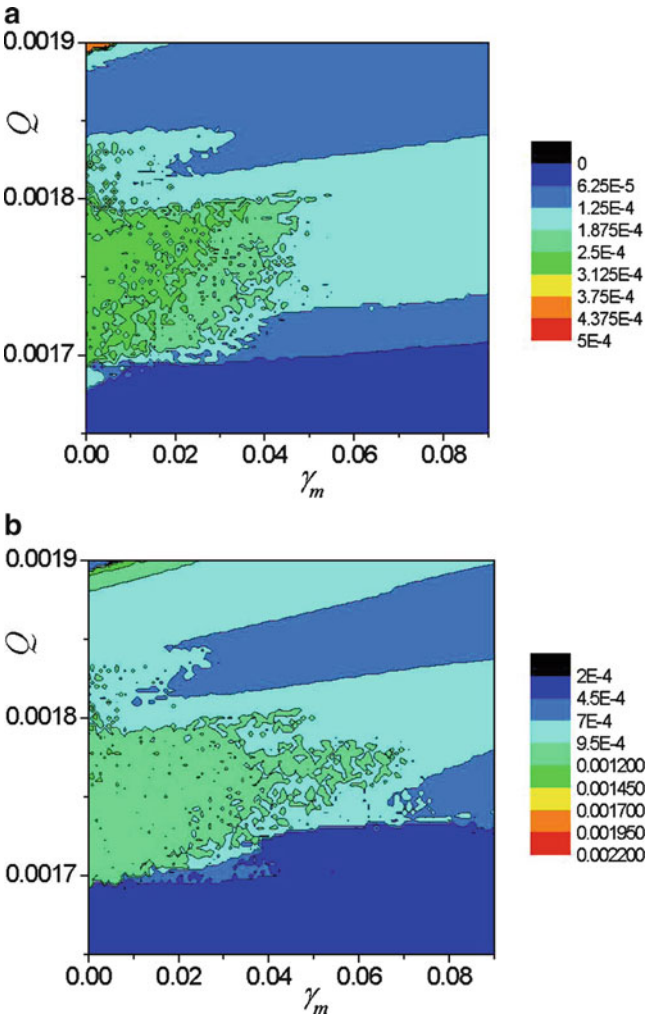

Fig. 1.55 Amplitude level contours (corresponding to Fig. 1.53a, b) of horizontal (**a**) and vertical (**b**) vibrations of rotor (1.199) in parametric plane (γ_m, Q) at $\delta = 0.000001$, $C = 0.2$, $\lambda_m = 500$, $k_z = 0.000055$, $\gamma = 15$, $\beta = 0.25$, $n = 1.0$, $\Omega = 0.87$, $Q_0 = 0$, $x_0 = 0$, $y_0 = 0$, $x(0) = y(0) = 10^{-8}$, $\dot{x}(0) = \dot{y}(0) = 0$, $z_1(0) = z_2(0) = 0$

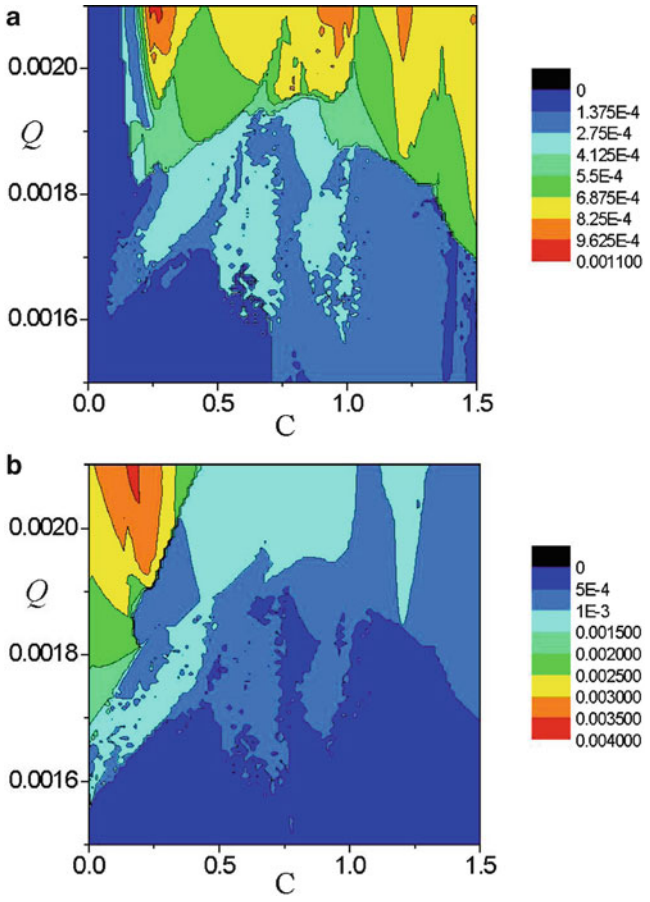

Fig. 1.56 Amplitude level contours (corresponding to Fig. 1.52a, b) of horizontal (**a**) and vertical (**b**) vibrations of rotor (1.199) in parametric plane (C, Q) at $\delta = 0.000001$, $\gamma_m = 0$, $\lambda_m = 500$, $k_z = 0.000055$, $\gamma = 15$, $\beta = 0.25$, $n = 1.0$, $\Omega = 0.87$, $Q_0 = 0$, $x_0 = 0$, $y_0 = 0$, $x(0) = y(0) = 10^{-8}$, $\dot{x}(0) = \dot{y}(0) = 0$, $z_1(0) = z_2(0) = 0$

References

1. S.H. Crandall, D.C. Karnogg, E.F. Kurtz, D.C. Pridmore-Brown, *Dynamics of Mechanical and Electromechanical Systems* (McGraw-Hill, New York, 1968)
2. A. Preumont, *Mechatronics: Dynamics of Electromechanical and Piezoelectric Systems* (Springer, Berlin, 2006)
3. J. Awrejcewicz, *Classical Mechanics: Dynamics* (Springer, Berlin, 2012)
4. A. Nicolaide, *Magnetism and Magnetic Materials: Theory, Properties, Modeling* (Transylvania University Press, Transylvania, 2001)
5. A. Green, K.C. Craig, Robust, design, nonlinear control of magnetic-levitation systems. J. Dyn. Meas. Contr. **120**(4), 488–495 (1998)
6. A. Piat, *Active Magnetic Suspension and Bearing. Modeling and Simulation* (InTech Education and Publishing, Vienna, 2008), pp. 453–470
7. M. Aliasghary, et al., *Sliding mode control of magnetic levitation system using radial basis function neural network.* IEE XPlore, RAM (2008), pp. 467–470
8. P. Olejnik, J. Awrejcewicz, in *Magnetic Levitation of a Light Cylindrical-Shape Mass with Control of Damping of the Transition-State Vibrations. Proceedings of the XXIV Symposium "Vibrations in Physical Systems,"* Pozna-Bedlewo, 12–15 May 2010
9. A.H. Nayfeh, D.T. Mook, *Nonlinear Oscillations* (Wiley Interscience, New York, 1979)
10. V.I. Arnold, *Geometrical Methods in Theory of Ordinary Differential Equations* (Springer, Berlin, 1983)
11. J. Guckenheimer, P. Holmes, *Nonlinear Oscillations: Dynamical Systems and Bifurcations of Vector Fields* (Springer, Berlin, 1983)
12. W.P. Rubanik, *Oscillations in Complex Quasilinear Systems with Dealy* (University Press, Minsk, 1985), in Russian
13. J. Awrejcewicz, Nonlinear oscillations of a string caused by the electromagnetic field. J. Tech. Phys. **35**, 1–2, 5–12 (1994)
14. J. Awrejcewicz, Strange nonlinear behaviour governed by a set of four averaged amplitude equations. Meccanica **31**, 347–361 (1996)
15. J. Awrejcewicz, V.A. Krysko, *Introduction to Asymptotic Methods* (Taylor and Francis Group, Boca Raton, FL, 2006)
16. J. Awrejcewicz, *Bifurcation and Chaos in Simple Dynamical Systems* (World Scientific, Singapore, 1989)
17. J. Awrejcewicz, *Bifurcation and Chaos in Coupled Oscillators* (World Scientific, Singapore, 1999)
18. A. Tondl, *Some Problems of Rotor Dynamics* (Chapman & Hall, London, 1965)
19. T. Someya, *Journal-Bearing Databook* (Springer, Berlin, 1998)
20. J.S. Rao, *Rotor Dynamics* (Wiley, New York, 1991)
21. R. Gasch, R. Nordmann, H. Pfützner, *Rotordynamik* (Springer, Berlin, 2002)
22. A. Muszyska, *Rotordynamics* (CRC Press, Boca Raton, FL, 2005)
23. W. Kurnik, Active magnetic antiwhirl control of a rigid rotor supported on hydrodynamic bearings. Mach. Dyn. Prob. **10**, 21–36 (1995)
24. K. Dziedzic, W. Kurnik, Stability of a rotor with hybrid magneto-hydrodynamic support. Mach. Dyn. Prob. **26**(4), 33–43 (2002)
25. P. Flores, J. Ambrosio, J.C. Claro, H.M. Lancarani, C.S. Koshy, Lubricated revolute joints in rigid multibody systems. Non-linear Dynm. **56**, 277–295 (2009)
26. C.W. Chang-Jian, C.K. Chen, Non-linear analysis of a rub-impact rotor supported by turbulent couple stress fluid film journal bearings under quadratic damping. Non-linear Dynam. **56**, 297–314 (2009)
27. W. Zhang, X.P. Zhan, Periodic and chaotic motions of a rotor-active magnetic bearing with quadratic and cubic terms and time-varying stiffness. Non-linear Dynam. **41**, 331–359 (2005)
28. A. Boyaci, H. Hetzler, W. Seeman, C. Proppe, J. Wauer, Analytical bifurcation analysis of a rotor supported by floating ring bearings. Non-linear Dynam. **57**, 497–507 (2009)

29. B. Schweizer, Oil whirl, oil whip and whirl/whip synchronization occurring in rotor systems with full-floating ring bearings. Non-linear Dynam. **57**, 509–532 (2009)
30. G.F. Zhang, W.N. Xu, B. Xu, W. Zhang, Analytical study of non-linear synchronous full annular rub motion of flexible rotor-stator system and its dynamic stability. Non-linear Dynam. **57**, 579–592 (2009)
31. Y. Ishida, M. Inagaki, R. Ejima, A. Hayashi, Non-linear resonances and self-excited oscillations of a rotor caused by radial clearance and collision. Non-linear Dynam. **57**, 593–605 (2009)
32. D.D. Quinn, Resonant dynamics in a rotordynamics system with non-linear inertial coupling and shaft anisotropy. Non-linear Dynam. **57**, 623–633 (2009)
33. R. Bouc, Modele mathmatique d'hystrsis (A mathematical model for hysteresis). Acustica **21**, 16–25 (1971)
34. Y.K. Wen, Method for random vibration of hysteretic system. J. Eng. Mech. Div. **102**(EMI), 246–263 (1976)
35. J. Awrejcewicz, L. Dzyubak, Hysteresis modelling and chaos prediction in one- and 2-DOF hysteretic models. Arch. Appl. Mech. **77**, 261–279 (2007)
36. F. Ikhouave, J. Rodellar, *Systems with Hysteresis* (Wiley, Chichester, 2007)
37. J.W. Mack, P. Nistri, P. Zecca, Mathematical models for hysteresis. SIAM Rev. **35**(1), 94–123 (1993)
38. J. Awrejcewicz, L. Dzyubak, C. Grebogi, Estimation of chaotic and regular (stick-slip and slip-slip) oscillations exhibited by coupled oscillators with dry friction. Non-linear Dynam. **42**(2), 383–394 (2005)
39. Z. Osinski (ed.), *Damping of Vibrations* (A.A. Balkema, Rotterdam, Brookfield, 1998)
40. J. Awrejcewicz, L. Dzyubak, Chaos caused by hysteresis and saturation phenomenon in 2-DOF vibrations of the rotor supported by the magneto-hydrodynamic bearing. Int. J. Bifurcation Chaos **21**(10), 2801–2823 (2011)